

A STUDY OF TWO- AND THREE-DIMENSIONAL
TURBULENT BOUNDARY LAYER DATA SETS USING
MOMENTUM INTEGRAL TECHNIQUES

by

David O. Fitts

Thesis submitted to the Faculty of the
Virginia Polytechnic Institute and State University
in partial fulfillment of the requirements for the degree of
MASTER OF SCIENCE
in
Mechanical Engineering

APPROVED:

F. J. Pierce, Chairman

H. L. Moses

S. B. Thomason

March, 1982

Blacksburg, Virginia

ACKNOWLEDGMENTS

The author wishes to extend special thanks to his major professor, Dr. F. J. Pierce, whose advise and encouragement made it possible to complete this work. Thanks are also extended to Dr. H. L. Moses and Dr. S. B. Thomason for serving on the author's graduate committee.

The author would like to acknowledge Mr. John Menna and Mr. Martin Harsh for their help in the completion of this study. Special thanks go to all the Mechanical Engineering graduate students who made this effort an enjoyable experience.

NASA is gratefully acknowledged for their financial support, as is Dr. J. B. Jones for providing a Presidential Fellowship for the author's graduate work.

Finally, a special thanks is extended to the author's parents and family for their support and encouragement through his higher education.

TABLE OF CONTENTS

	<u>Page</u>
Acknowledgments	ii
Table of Contents	iii
List of Figures	v
List of Tables	vii
Nomenclature	ix
1. Introduction	1
1.1 Classification of Boundary Layers	1
1.2 Motivation for the Study	2
1.3 Scope of Investigation	3
2. Two- and Three-Dimensional Momentum Integral Equations	4
2.1 Two-Dimensional Momentum Integral Equations	5
2.2 Three-Dimensional Momentum Integral Equations	11
2.2.1 Description of the Three-Dimensional Boundary Layer	11
2.2.2 The General Three-Dimensional Momentum Integral Equations for Cartesian Coordinates	14
2.2.3 Infinite Swept-Wing Momentum Integral Equations	16
2.2.4 Plane of Symmetry Momentum Integral Equations	17
2.2.5 Axisymmetric Momentum Integral Equations with and without Body Rotation	18
2.2.6 Examination of Three-Dimensional Data Sets	20
3. Review of Turbulent Boundary Layer Experiments	23
3.1 Two-Dimensional Experiments	23

TABLE OF CONTENTS
(Continued)

	<u>Page</u>
3.2 Three-Dimensional Experiments	24
4. Method of Analysis	30
5. Results and Discussion	37
5.1 Two-Dimensional Data Sets	38
5.1.1 Kong - Axisymmetric Flows	38
5.1.2 Strickland and Simpson - Zero Pressure Gradient and Separating Flows	40
5.1.3 Menna - Two-Dimensional Flow	54
5.2 Nominally Two-Dimensional Flow with Slight Three- Dimensionality	61
5.2.1 Menna - Assumed Plane of Symmetry in Collateral Flow	65
5.2.2 Menna - Assumed Plane of Symmetry in Skewed Flow	67
5.3 Three-Dimensional Data Sets	74
5.3.1 Horne - Upstream Initial and Edge Conditions .	74
5.3.2 Elsenaar and Boelsma, van den Berg and Elsenaar - Infinite Swept-Wing Flow	85
5.3.3 Pierce and McAllister - Flow About a Strut-Flat Plate Junction	94
6. Conclusions	107
References	109
Vita	114
Abstract	

LIST OF FIGURES

<u>Figure</u>	<u>Page</u>
1. Coordinate System for Axisymmetric Flow	10
2. Unilaterally Skewed Three-Dimensional Boundary Layer . .	12
3. Bilaterally Skewed Three-Dimensional Boundary Layer . . .	13
4. Measurement Locations for Kong's Axisymmetric Flows . . .	39
5. Kong, 12.7 cm H ₂ O Dynamic Pressure Flow	42
6. Kong, 17.8 cm H ₂ O Dynamic Pressure Flow	43
7. Measurement Locations for Strickland and Simpson's Separating Flow	47
8. Strickland and Simpson, 30 ft/sec Zero Pressure Gradient Flow	51
9. Strickland and Simpson, 60 ft/sec Zero Pressure Gradient Flow	52
10. Strickland and Simpson, Separating Flow	53
11. Menna, Two-Dimensional Flow	58
12. Coordinate Systems for Plane of Symmetry in a Collateral Spreading Flow	62
13. Freestream Streamline Map for Skewed Spreading Flow on a Plane of Symmetry	63
14. Freestream Streamline Map for Skewed Converging Flow on a Plane of Symmetry	64
15. Menna, Assumed 1/12 deg/in. Collateral Freestream Convergence at a Plane of Symmetry	69
16. Menna, Skewed Plane of Symmetry, Case No. 1	75
17. Menna, Skewed Plane of Symmetry, Case No. 2	76
18. Menna, Skewed Plane of Symmetry, Case No. 3	77
19. Menna, Skewed Plane of Symmetry, Case No. 4	78

LIST OF FIGURES
(Continued)

<u>Figure</u>	<u>Page</u>
20. Menna, Skewed Plane of Symmetry, Case No. 5	79
21. Menna, Skewed Plane of Symmetry, Case No. 6	80
22. Menna, Skewed Plane of Symmetry, Case No. 7	81
23. Measurement Locations for Menna and Horne	84
24. Horne, Assumed Two-Dimensional Flow	86
25. Measurement Locations for Elsenaar and Boelsma, and van den Berg and Elsenaar	90
26. Elsenaar and Boelsma, Infinite Swept-Wing, X-Equation . .	91
27. Elsenaar and Boelsma, Infinite Swept-Wing, Z-Equation . .	92
28. van den Berg and Elsenaar, Infinite Swept-Wing, X- Equation	95
29. van den Berg and Elsenaar, Infinite Swept-Wing, Z- Equation	96
30. Data Stations for Pierce and McAllister's Teardrop Flow .	98
31. Pierce and McAllister Teardrop Column G, X-Equation . . .	100
32. Pierce and McAllister Teardrop Column G, Z-Equation . . .	101
33. Pierce and McAllister Teardrop Row +5, X-Equation	102
34. Pierce and McAllister Teardrop Row +5, Z-Equation	103

LIST OF TABLES

<u>Table</u>	<u>Page</u>
1. C_f Differences in Kong's Axisymmetric Data Sets	41
2. PL and PR for Kong's 12.7 cm H ₂ O Dynamic Pressure Flow .	44
3. PL and PR for Kong's 17.8 cm H ₂ O Dynamic Pressure Flow .	45
4. PL and PR for Strickland and Simpson's 30 ft/sec Zero Pressure Gradient Flow	48
5. PL and PR for Strickland and Simpson's 60 ft/sec Zero Pressure Gradient Flow	49
6. PL and PR for Strickland and Simpson's Separating Flow .	50
7. Menna, Friction Velocity Comparison	56
8. Menna, Boundary Layer Parameter Comparison	57
9. PL and PR for Menna' Two-Dimensional Flow. A Comparison using Different Boundary Layer Parameter Integration Techniques	59
10. PL and PR for Menna's Two Dimensional Flow. A Comparison using Friction Velocities Inferred from Different Law of the Wall Constants	60
11. Average Collateral Convergence/Divergence of Menna's Assumed Plane of Symmetry Flow	68
12. PL and PR for Mennas Assumed Collateral Plane of Symmetry Flow. Assumes Freestream Convergence = 1/12 deg/in. . .	70
13. Freestream Spreading and Skewing Rates of Menna's Assumed Plane of Symmetry Flow	73
14. PL and PR for Menna's Assumed Skewed Plane of Symmetry Flow, Cases 1-7	82
15. Freestream Spreading and Velocity Profile Skewing Contributions to PL for Cases 3 and 4	83
16. PL and PR for Horne's Upstream Condition Flow. Assumes Two-Dimensional Flow	87

LIST OF TABLES
(Continued)

<u>Table</u>	<u>Page</u>
17. Average Collateral Convergence/Divergence of Horne's Assumed Plane of Symmetry Flow	88
18. PL and PR for Elsenaar and Boelsma's Infinite Swept-Wing Flow	93
19. PL and PR for van den Berg and Elsenaar's Infinite Swept-Wing Flow	97
20. PL and PR for Pierce and McAllister's Strut-Flat Plate Flow on Column G	104
21. PL and PR for Pierce and McAllister's Strut-Flat Plate Flow on Row +7	105

Nomenclature

c	Law of the Wall constant
c_f	Skin friction coefficient, $\tau_0 / \rho Q^2/2$
G	Typical time-averaged component of flow variable
G'	Typical fluctuating component of flow variable
\tilde{G}	Typical instantaneous flow variable
h_3	Metric in the orthogonal curvilinear coordinate set
P	Time-averaged component of pressure
PL	Integrated left-hand side of momentum integral equation
PR	Integrated right-hand side of momentum integral equation
Q	Freestream velocity
Re/L	Unit Reynolds number
r_0	Local radius of body of revolution
T	Period over which time-averaging is performed
t	Time
U	Cartesian freestream velocity component in x-direction
u	Cartesian boundary layer velocity component in x-direction
u_s	Curvilinear boundary layer velocity component in ξ -direction
u^*	Friction or shear velocity
u^+	Nondimensionalized velocity component
v	Cartesian boundary layer velocity component in y-direction
W	Cartesian freestream velocity component in z-direction
w	Cartesian boundary layer velocity component in z-direction
W_0	Surface transverse velocity of rotating body

w_s Curvilinear boundary layer velocity component in ζ -direction

x, y, z Cartesian coordinate set

y^+ Nondimensionalized wall distance

α Boundary layer skew angle

α_0 Boundary layer skew angle at the wall

β Angle between freestream direction and x-direction

δ Boundary layer thickness

$$\delta_{\xi}^* = \frac{1}{Q} \int_0^{\infty} \{ Q - u_s \} d\eta$$

$$\delta_1^* = \frac{1}{Q} \int_0^{\infty} \{ U - u \} dy$$

$$\delta_3^* = \frac{1}{Q} \int_0^{\infty} \{ W - w \} dy$$

ξ, η, ζ Curvilinear coordinate set

$$\theta_{xz} = \int_0^{\infty} \left\{ \frac{u}{U} \frac{w}{W_0} \right\} dy$$

$$\theta_z = \int_0^{\infty} \left\{ \frac{w}{W_0} \right\} dy$$

$$\theta_{\xi} = \frac{1}{Q^2} \int_0^{\infty} u_s (Q - u_s) d\eta$$

$$\theta_{\xi\zeta} = \frac{1}{Q^2} \int_0^{\infty} w_s (Q - u_s) d\eta$$

$$\theta_{11} \quad \frac{1}{Q^2} \int_0^{\infty} u \{U - u\} dy$$

$$\theta_{13} \quad \frac{1}{Q^2} \int_0^{\infty} w \{U - u\} dy$$

$$\theta_{31} \quad \frac{1}{Q^2} \int_0^{\infty} u \{W - w\} dy$$

$$\theta_{33} \quad \frac{1}{Q^2} \int_0^{\infty} w \{W - w\} dy$$

κ Law of the Wall constant

μ Dynamic viscosity

ν Kinematic viscosity

ρ Density

τ Total shear stress

τ_0 Total wall shear stress

τ_x Shear stress component in x-direction

τ_z Shear stress component in z-direction

Ω Angular velocity of rotating body

1. Introduction

1.1 Classification of Boundary Layers

Boundary layer flows are generally classified as laminar or turbulent flows. Laminar boundary layers exhibit only slight mixing between fluid layers and shearing stresses through the boundary layer are due to viscous effects only. Turbulent boundary layers are characterized by random fluctuations and strong mixing of the flow, with shear stresses resulting from viscous and turbulent mixing effects. Laminar boundary layer flows are easier to predict than turbulent boundary layer flows due to the lack of randomness of the flow. However, turbulent flows are much more likely to occur in real world circumstances, such as with external flows over wings, aircraft fuselages, missiles, and ship hulls, or internal flows through pipes, ducts, nozzles, diffusers, and turbomachinery passages.

Boundary layer flows may also be classified as two- or three-dimensional. As the flow takes on additional degrees of freedom, accurate prediction of the flow field becomes more difficult. Much work has been performed in the area of two-dimensional turbulent boundary layer (2DTBL) flows in the past, and for the most part, these flows are well understood. During the past decade, emphasis has been placed on the analysis of the more complex three-dimensional turbulent boundary layers (3DTBL) since 3DTBLs are more often found in engineering practice than 2DTBLs.

1.2 Motivation for the Study

A common means of checking the accuracy of numerical prediction methods is to compare the computed flow field to an experimentally measured flow field. Differences between the computed and measured flow fields may be attributed to several factors, among which are poor turbulence models, poor prediction codes, erroneous data, and/or a measured flow field which is not described by the assumed flow field. For two-dimensional flows, accurate prediction methods exist and carefully controlled experiments provide good data. However, the construction of a truly two-dimensional flow is not a simple matter. Several studies (1), (2), (3) of nominally two-dimensional experimental flows have shown that small amounts of three-dimensionality can exist in even the most carefully controlled experiments. de Brederode and Bradshaw (1) identify several causes of small spanwise flow as (i) non-uniformity of the incoming boundary layer at the tunnel contraction exit, (ii) non-straight transition line, and (iii) displacement effects caused by the side-wall boundary layer growth and by the secondary corner flows. Such three dimensionality could be important when comparing computed results modeling a two-dimensional flow to the experimentally measured nominally two-dimensional flow containing some small three-dimensionality.

Before comparing predicted results to measured quantities, it is desirable to somehow verify how closely the actual measured flow field represents the assumed nominal flow field. One means of checking the actual flow field is to substitute the measured data into the differ-

ential equations of motion for the nominal flow field. Agreement between the opposite sides of the equations would generally indicate that the actual flow field is as assumed. The difficulty with this method is that various derivatives of measured quantities are required, thus introducing errors from differentiation of experimental data with scatter. In order to minimize the difficulties in differentiating experimental data, integral techniques may be utilized. It should be noted that integral methods are less detailed in that the equations of motion are not solved for the entire flow field, but rather for an average across the entire boundary layer.

1.3 Scope of Investigation

This study examined selected two- and three-dimensional turbulent boundary layer data sets using momentum integral techniques. This study also examined the effect of small amounts of three-dimensionality which may be present in nominally two-dimensional flows. It should be stressed that the measured flow fields were not compared to the results of integral prediction methods. Rather, the appropriate momentum integral equation was numerically integrated using parameters obtained from experimentally measured data. Using this technique, a determination as to whether the measured data sets were consistent with the assumed nominal flow fields could be made. To determine which experimental flows could readily be examined using momentum integral equations in Cartesian coordinates, and in order to avoid a duplication of effort, a brief review of 2D- and 3DTBL experiments is presented.

2. Two- and Three-Dimensional Momentum Integral Equations

Turbulent flows are generally examined using a mean-flow analysis for engineering purposes. With the mean-flow analysis, the gross properties of a turbulent flow, such as mean velocity and temperature profiles, boundary layer thickness parameters, and skin friction coefficients can be predicted. Following the original ideas of Reynolds, the fluid is assumed to exist in a random, unsteady turbulent state, requiring time-averaging for the mean equations of motion. Any variable \tilde{G} is resolved into a mean value, G , plus a fluctuating value G' , such that the following relations hold true:

$$\tilde{G} = G + G' \quad 2.1$$

$$G = \frac{1}{T} \int_{t_0}^{t_0 + T} \tilde{G} \, dt \quad 2.2$$

$$0 = \frac{1}{T} \int_{t_0}^{t_0 + T} G' \, dt \quad 2.3$$

The period T over which the integration is performed is chosen such that it is significantly larger than the typical period of the fluctuating term, G' , and the integration takes a time-average of the variable in question.

2.1 Two-Dimensional Momentum Integral Equations

The equations of motion in the Cartesian coordinate system for a steady, two-dimensional, incompressible turbulent boundary layer flow are:

$$\frac{\partial u}{\partial x} + \frac{\partial v}{\partial y} = 0 \quad 2.4$$

$$u \frac{\partial u}{\partial x} + v \frac{\partial u}{\partial y} = - \frac{1}{\rho} \frac{\partial P}{\partial y} + \frac{1}{\rho} \frac{\partial \tau}{\partial y} \quad 2.5$$

$$0 = - \frac{1}{\rho} \frac{\partial P}{\partial y} \quad 2.6$$

A derivation of these equations from the full Navier-Stokes equations may be found in Currie (4) or White (5). The total shear, τ , of Eq. 2.5 is a combination of viscous and turbulent shear terms, such that:

$$\tau = \mu \frac{\partial u}{\partial y} + \rho \overline{u'v'} \quad 2.7$$

viscous turbulent
shear shear

The turbulent shear term, $\rho \overline{u'v'}$, is often referred to as the Reynolds stress, the overbar designating a time-average of the fluctuating velocity product. The Reynolds normal stresses are often included in the motion equations as boundary layer separation is approached, since the assumption that these terms remain small has been questioned near separation.

The two-dimensional momentum integration equation is obtained by integrating the equations of motion across the boundary layer thickness and applying the following boundary conditions:

$$u(x,0) = v(x,0) = 0 \quad 2.8$$

$$u(x,\infty) = U(x) \quad 2.9$$

$$\tau(x,0) = \tau_0(x) \quad 2.10$$

$$\tau(x,\infty) = 0 \quad 2.11$$

Performing the integration as outlined by Currie results in the von Karman integral relation:

$$\frac{d\theta_{11}}{dx} + (2\theta_{11} + \delta_1^*) \frac{1}{U} \frac{dU}{dx} = \frac{C_f}{2} \quad 2.12$$

Usually, Eq. 2.12 is used with other ancillary equations to predict two-dimensional flow fields. In this study, the momentum integral equation is used to see whether the measured data sets are consistent with the assumed nominal flow field. The advantage of the momentum integral equation over the differential equations of motion, in this application, is that there are no y -dependences or y -derivatives in the equation. The necessary parameters are readily obtained from experimental data sets and may be substituted into the

momentum integral equation for comparison of the two sides. However, this method of examination still requires the differentiation of parameters obtained from experimental data. In order to avoid differentiation of parameters, Coles (6) suggests that the momentum integral equation can be numerically integrated.

For experimental flows, velocity measurements can be obtained using impact or hot-wire/film probes, from which δ_1^* , θ_{11} , and U are determined. Skin friction may be measured indirectly, for example, using surface fences, Preston tubes, or razor blades, or directly using floating element devices.

For two-dimensional data sets without skin friction data, near-wall similarity may be used to infer this parameter. It has been shown that nearly all 2DTBL's exhibit similarity in 10-20% of the boundary layer thickness near the wall. This near-wall region can be divided into three sub-regions,

- 1) The laminar or viscous sublayer, where viscous shear is dominant,
- 2) An overlap or buffer sub-region where both viscous shear and turbulent shear are of the same order of magnitude, and
- 3) The Law of the Wall subregion, where turbulent shear dominates,

The near-wall regions, (1) and (3), have been modeled by the two equations:

$$u^+ = y^+ \quad , \quad 0 \leq y^+ \leq y_i^+ \quad 2.13$$

$$u^+ = \frac{1}{\kappa} \ln y^+ + c, \quad y^+ \geq y_i^+ \quad 2.14$$

where,

$$u^+ = \frac{u}{u^*} \quad 2.15$$

$$y^+ = \frac{yu^*}{\nu} \quad 2.16$$

$$u^* = \sqrt{\frac{\tau_0}{\rho}} \quad 2.17$$

The constants κ and c are experimentally determined coefficients and y_i^+ is the value of y^+ at which Eqs. 2.13 and 2.14 intersect. The most popular pairs of constants are those of Coles and Hirst (7) and Patel (8), and to a lesser extent, those of the N.P.L. (9). These groups of constants show reasonably close agreement when plotted in similarity coordinates. Spalding (10) models the entire near-wall region with the single third-order equation:

$$y^+ = u^+ + e^{-\kappa c} \left[e^{\kappa u^+} - 1 - \kappa u^+ - \frac{\{\kappa u^+\}^2}{2} - \frac{\{\kappa u^+\}^3}{6} \right] \quad 2.18$$

Noting that $u^+ y^+$ equals uy/ν , each point in a velocity profile may be evaluated for u^* . A more complete discussion of two-dimensional near-wall similarity can be found in White (5) or Coles (6).

A special case of the 2DTBL is the steady, axisymmetric flow past a body of revolution. With the assumption that the local surface

radius, $r_0(x)$, is much greater than the boundary layer thickness, White (5) gives the boundary layer continuity and momentum equations for the coordinates of Fig. 1 as:

$$\frac{\partial(r_0 u)}{\partial x} + r_0 \frac{\partial v}{\partial y} = 0 \quad 2.19$$

$$u \frac{\partial u}{\partial x} + v \frac{\partial u}{\partial y} = -\frac{1}{\rho} \frac{\partial P}{\partial x} + \frac{1}{\rho} \frac{\partial \tau}{\partial y} \quad 2.20$$

$$0 = -\frac{1}{\rho} \frac{\partial P}{\partial y} \quad 2.21$$

The momentum integral equation is determined in the same manner as Eq. 2.12, resulting in

$$\frac{d\theta_{11}}{dx} + \left(2\theta_{11} + \delta_1^*\right) \frac{1}{U} \frac{dU}{dx} + \frac{\theta_{11}}{r_0} \frac{dr_0}{dx} = \frac{c_f}{2} \quad 2.22$$

For an axisymmetric flow past a cylinder of constant radius, Eq. 2.22 reduces to Eq. 2.12.

If a cylindrical body is long enough, the assumption that $\delta \ll r_0$ may fail and the boundary layer thickness can become of the order of the body diameter or greater. The main effect of a thick axisymmetric boundary layer is that the cylindrical geometry must be taken into account along with the resulting transverse-curvature effects. Since this study will not deal with thick axisymmetric flows, further discussion of this topic is omitted.

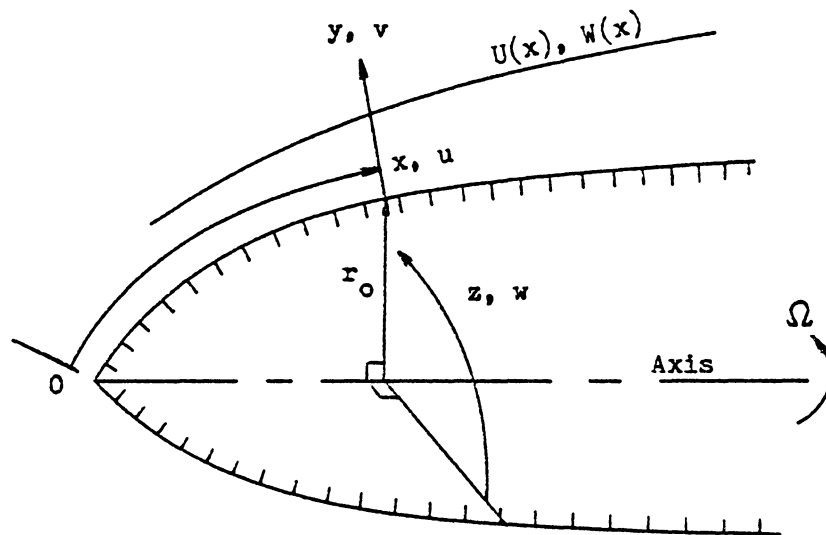


Fig. 1 Coordinate System for Axisymmetric Flow

2.2 Three-Dimensional Momentum Integral Equations

2.2.1 Description of the Three-Dimensional Boundary Layer

The aspect of the 3DTBL which distinguishes it from the 2DTBL is the skewing or turning of the flow within the boundary layer. Figure 2 shows a typical 3DTBL with unilateral skewing, that is, the skew direction is to one side of the freestream streamline direction. Three-dimensional boundary layers may also exhibit bilateral skewing as shown in Fig. 3.

Figures 2 and 3 show the coordinate systems commonly used when studying 3DTBL's. The orthogonal curvilinear or freestream streamline coordinate set is oriented so that the ξ -direction follows freestream streamlines. The Cartesian coordinate set may be oriented in any direction, though the orientation is usually dependent upon the flow geometry.

Three-dimensional flows can also be classified as being pressure-driven or shear-driven. Pressure-driven 3DTBLs are produced as a result of a transverse freestream pressure gradient acting through the boundary layer. The curvature of high-momentum fluid in the freestream is balanced by the pressure gradient normal to the freestream direction. The freestream pressure gradient acts throughout the boundary layer, causing the lower momentum fluid near the wall to curve more than the freestream in order to balance the transverse pressure gradient. Pressure-driven 3DTBLs are found in curved channels, on the surface of swept wings, and ahead of swept-steps or other obstructions in the flow field. Shear-driven flows occur when the shearing action

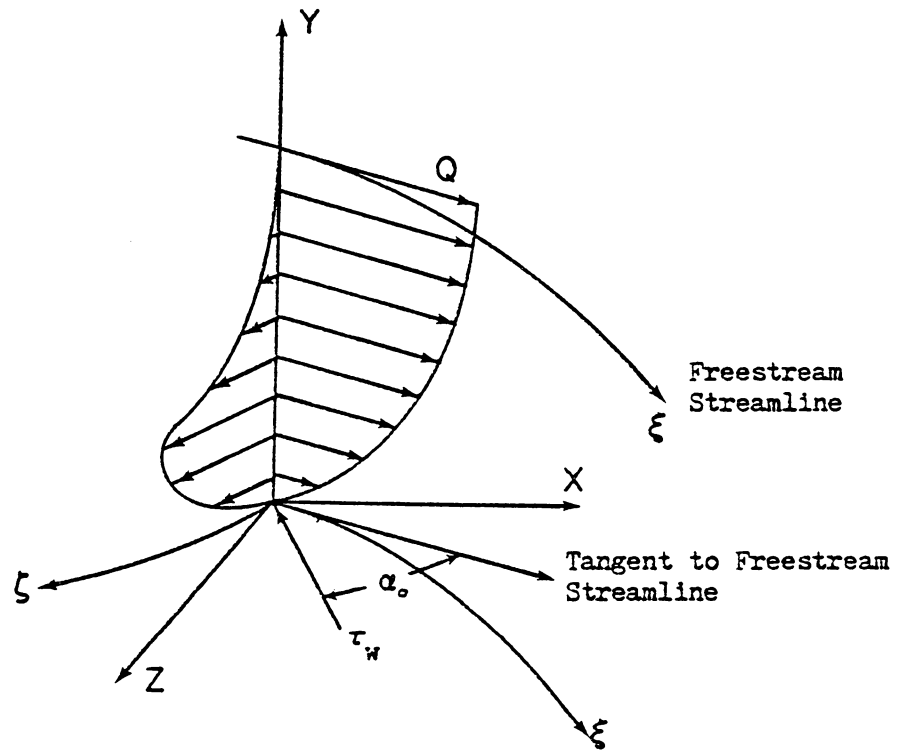


Fig. 2 Unilaterally Skewed Three-Dimensional Boundary Layer

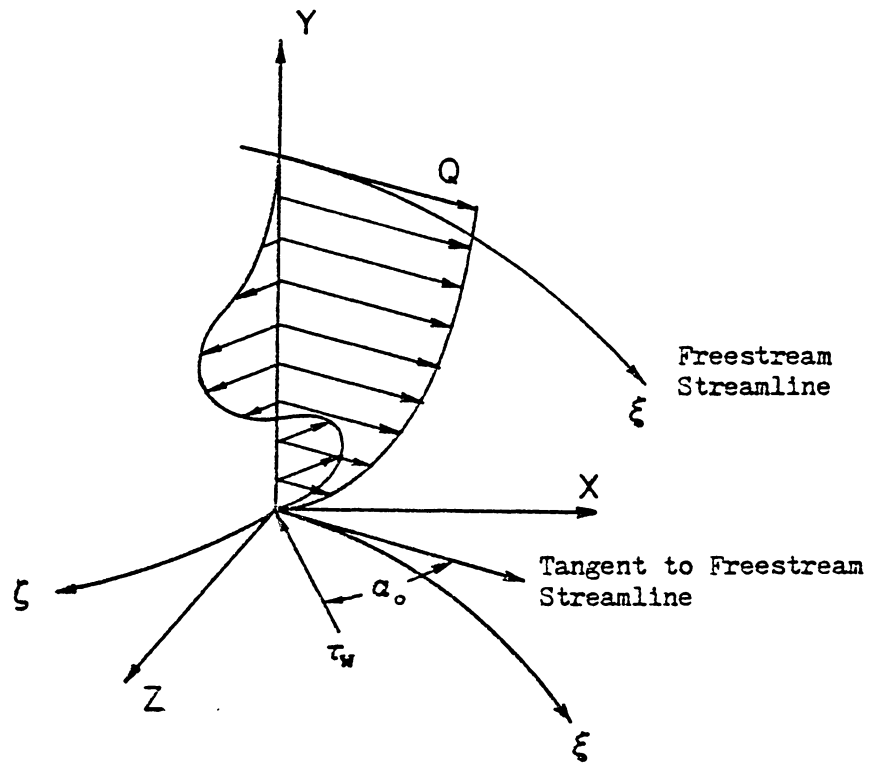


Fig. 3 Bilaterally Skewed Three-Dimensional Boundary Layer

between adjacent fluid layers is the primary cause of the secondary flow. Such flows are the relaxing flows downstream of swept-steps or flows parallel to rotating bodies of revolution.

2.2.2 The General Three-Dimensional Momentum Integral Equations for Cartesian Coordinates

The equations of motion for the steady, incompressible three-dimensional turbulent boundary layer flow in a Cartesian coordinate system are:

$$\frac{\partial u}{\partial x} + \frac{\partial v}{\partial y} + \frac{\partial w}{\partial z} = 0 \quad 2.23$$

$$u \frac{\partial u}{\partial x} + v \frac{\partial u}{\partial y} + w \frac{\partial u}{\partial z} = -\frac{1}{\rho} \frac{\partial P}{\partial x} + \frac{1}{\rho} \frac{\partial \tau_x}{\partial y} \quad 2.24$$

$$0 = -\frac{1}{\rho} \frac{\partial P}{\partial y} \quad 2.25$$

$$u \frac{\partial w}{\partial x} + v \frac{\partial w}{\partial y} + w \frac{\partial w}{\partial z} = -\frac{1}{\rho} \frac{\partial P}{\partial z} + \frac{1}{\rho} \frac{\partial \tau_z}{\partial y} \quad 2.26$$

where,

$$\tau_x = \mu \frac{\partial u}{\partial y} - \overline{\rho u'v'} \quad 2.27$$

$$\tau_z = \mu \frac{\partial w}{\partial y} - \overline{\rho v'w'} \quad 2.28$$

As in the two-dimensional equations of motion, Reynolds normal stress terms may be included in the motion equations as boundary layer separation is approached.

The three-dimensional momentum integral equations in Cartesian coordinates are derived in the same manner as the two-dimensional equation with the boundary conditions:

$$u(x, 0, z) = v(x, 0, z) = w(x, 0, z) = 0 \quad 2.29$$

$$u(x, \infty, z) = U(x, z) \quad 2.30$$

$$w(x, \infty, z) = W(x, z) \quad 2.31$$

$$\tau_x(x, 0, z) = \tau_{0_x}(x, z) \quad 2.32$$

$$\tau_x(x, 0, z) = \tau_{0_z}(x, z) \quad 2.33$$

$$\tau_x(x, \infty, z) = \tau_z(x, \infty, z) = 0 \quad 2.34$$

Integrating the continuity and momentum equations through the boundary layer thickness gives for the x-direction:

$$\frac{\delta_1^*}{Q} \frac{\partial U}{\partial x} + \frac{2\theta_{11}}{Q} \frac{\partial Q}{\partial x} + \frac{\partial \theta_{11}}{\partial x} + \frac{\delta_3^*}{Q} \frac{\partial U}{\partial z} + \frac{2\theta_{13}}{Q} + \frac{\partial Q}{\partial z} + \frac{\partial \theta_{13}}{\partial z} = \frac{\tau_{0_x}}{\rho Q^2} \quad 2.35$$

and for the z-direction:

$$\frac{\delta_1^*}{Q} \frac{\partial W}{\partial x} + \frac{2\theta_{31}}{Q} \frac{\partial Q}{\partial x} + \frac{\partial \theta_{31}}{\partial x} + \frac{\delta_3^*}{Q} \frac{\partial W}{\partial z} + \frac{2\theta_{33}}{Q} \frac{\partial Q}{\partial z} + \frac{\partial \theta_{33}}{\partial z} = \frac{\tau_{0_z}}{\rho Q^2} \quad 2.36$$

Note that for two dimensional flow in either the x- or z-direction, Eqs. 2.35 and 2.36 reduce to the two-dimensional momentum integral equation.

The three-dimensional momentum integral equations can also be derived for an orthogonal curvilinear set. However, since the locations of freestream streamlines in three-dimensional flows are difficult to determine accurately in experiments, this study will use the momentum integral equations in Cartesian coordinates only.

Certain 3DTBL flows are less complex than others. These simpler flows include the flow over an infinite-length swept-wing or plate, the plane of symmetry in a collateral spreading or skewed spreading flow, and the flow parallel to a rotating body of revolution.

2.2.3 Infinite Swept-Wing Momentum Integral Equations

The coordinate system for the flow over a nearly flat infinite swept-wing or plate utilizes an axis in the chordwise-direction (x-direction), an axis in the spanwise-direction (z-direction) and an axis normal to the surface (y-direction). This type of flow field is quasi-two-dimensional in that there are no spanwise variations in the flow. The momentum integral equations (Eqs. 2.35 and 2.36) thus reduce to:

$$\frac{\delta_1^*}{Q} \frac{dU}{dx} + \frac{2\theta_{11}}{Q} \frac{dQ}{dx} + \frac{d\theta_{11}}{dx} = \frac{\tau_{0x}}{\rho Q^2} \quad 2.37$$

$$\frac{\delta_1^*}{Q} \frac{dW}{dx} + \frac{2\theta_{31}}{Q} \frac{dQ}{dx} + \frac{d\theta_{31}}{dx} = \frac{\tau_{0z}}{\rho Q^2} \quad 2.38$$

2.2.4 Plane of Symmetry Momentum Integral Equation

Plane of symmetry flows are simplified because the flow on the plane of symmetry is collateral and most transverse derivatives are zero. For the plane of symmetry flow in the x-direction, Eqs. 2.35 and 2.36 reduce to:

$$\frac{\partial \theta_{11}}{\partial x} + \frac{(2\theta_{11} + \delta_1^*)}{U} \frac{\partial U}{\partial x} + \frac{\partial \theta_{13}}{\partial z} = \frac{\tau_{0x}}{\rho Q^2} \quad 2.39$$

The flow on the plane of symmetry of a spreading flow is two-dimensional in the sense that the boundary layer profile is collateral.

However, the flow field actually spreads from the plane of symmetry and this spreading effect is represented by the term $\frac{\partial \theta_{13}}{\partial z}$ in Eq. 2.39.

In the Cartesian coordinate set, this term does not indicate whether the flow field is spreading and collateral, or whether it is spreading and skewed. Pierce (11) has given the momentum integral equation for plane of symmetry flows in curvilinear coordinates as:

$$\frac{\partial \theta_\xi}{\partial \xi} + \frac{(2\theta_\xi + \delta_\xi^*)}{Q} \frac{\partial Q}{\partial \xi} + \frac{1}{h_3} \frac{\partial \theta_{\xi\zeta}}{\partial \zeta} + \frac{\theta_\xi}{h_3} \frac{\partial \beta}{\partial \zeta} = \frac{\tau_{0x}}{\rho Q^2} \quad 2.40$$

where the boundary layer parameters θ_ξ , δ_ξ^* , and $\theta_{\xi\zeta}$ and the metric h_3 are defined for the curvilinear set. On the plane of symmetry, the flow field is such that $\delta_\xi^* = \delta_1^*$, $\theta_\xi = \theta_{11}$ and $\frac{\partial}{\partial \xi} = \frac{\partial}{\partial x}$. Thus comparing Eqs. 2.39 and 2.40, it is apparent that the term $\frac{\partial \theta_{13}}{\partial z}$ of the

Cartesian set is the equivalent of the two terms $\frac{1}{h_3} \frac{\partial \theta_{\xi\zeta}}{\partial \zeta}$ and $\frac{\theta_{\zeta}}{h_3} \frac{\partial \beta}{\partial \zeta}$ of the curvilinear set.

Following the suggestions of Johnston (12), the third and fourth terms of Eq. 2.40 may be given simple physical interpretations. Referring to Fig. 2, the term $\frac{1}{h_3} \frac{\partial \theta_{\xi\zeta}}{\partial \zeta}$ represents the rate of change of the transport of freestream direction momentum in the ζ -direction with respect to the ζ -direction. The term $\frac{\theta_{\xi}}{h_3} \frac{\partial \beta}{\partial \zeta}$ accounts for the freestream direction momentum which, while being transported downstream, is also being distributed laterally, not by a lateral velocity, but by the spreading of the flow. Note that lateral velocities are in the ζ -direction, which is normal to the freestream streamline direction, but not necessarily normal to the plane of symmetry. If the flow near a plane of symmetry has no transverse velocity in the freestream streamline coordinate set, $\theta_{\xi\zeta}$ is zero by definition, and the term $\frac{\partial \theta_{13}}{\partial z}$ is due to collateral spreading of the straight freestream streamlines only. If lateral velocities do exist near the plane of symmetry, when viewed in the curvilinear coordinate set, the term $\frac{\partial \theta_{13}}{\partial z}$ is due to both the effects of skewing in the boundary layer and the spreading of the curved freestream streamlines.

2.2.5 Axisymmetric Momentum Integral Equations With and Without Body Rotation

The flow past a rotating or stationary body of revolution is quasi-two-dimensional in that the flow field does not change in the

circumferential direction. Skewing in the boundary layer is a result of the transverse shearing action between the body surface and the axially-flowing fluid.

Using the coordinate system of Fig. 1, the boundary layer equations of motion for the flow past a rotating body of revolution are:

$$\frac{\partial(r_0 u)}{\partial x} + \frac{\partial v}{\partial y} = 0 \quad 2.41$$

$$u \frac{\partial u}{\partial x} + v \frac{\partial u}{\partial y} - \frac{w^2}{r_0} \frac{dr_0}{dx} = - \frac{1}{\rho} \frac{dP}{dx} + \frac{1}{\rho} \frac{\partial \tau_x}{\partial y} \quad 2.42$$

$$0 = - \frac{1}{\rho} \frac{\partial P}{\partial y} \quad 2.43$$

$$u \frac{\partial w}{\partial x} + v \frac{\partial w}{\partial y} + \frac{uw}{r_0} \frac{dr_0}{dx} = \frac{1}{\rho} \frac{\partial \tau_z}{\partial y} \quad 2.44$$

These equations were derived with the assumption that $\delta \ll r_0$ in order that transverse-curvature effects can be ignored. The momentum integral equations are derived in the same manner as Eq. 2.22 with the exception of the boundary conditions:

$$w(x, 0, z) = W_0(x) = r_0(x) \Omega \quad 2.45$$

$$\tau_z(x, 0, z) = \tau_{0z}(x) \quad 2.46$$

$$\tau_z(x, \infty, z) = 0 \quad 2.47$$

where Ω is the angular velocity of the rotating body. The resulting momentum integral equations as presented by Schlichting (13) are:

$$\frac{d\theta_{11}}{dx} + \frac{(2\theta_{11} + \delta_1^*)}{U} \frac{dU}{dx} + \frac{(\theta_{11} + \frac{W_0^2}{U} \theta_z)}{r_0} \frac{dr_0}{dx} = \frac{\tau_{0x}}{\rho U^2} \quad 2.48$$

$$\frac{\Omega}{U^2 r_0^2} \frac{d}{dx} (U r_0^2 \theta_{xz}) = - \frac{\tau_{0z}}{\rho Q^2} \quad 2.49$$

Equations 2.48 and 2.49 also apply to the 3DTBL on a stationary body, although the boundary layer parameters θ_z and θ_{xz} would be redefined to avoid dividing by $W_0 = 0$. For two-dimensional axisymmetric flow, Eqs. 2.48 and 2.49 reduce to Eq. 2.22.

2.2.6 Examination of Three-Dimensional Data Sets

When comparing experimentally measured 3DTBL data sets to the equations of motion for a nominal three-dimensional flow field, the three-dimensional momentum integral equations have the same advantages over the differential equations of motion that the two-dimensional

momentum integral has over the two-dimensional differential equations of motion when examining 2DTBL data sets. The three-dimensional differential equations are functions of x , y , and z and contain x -, y -, and z -derivatives. The momentum integral equations are dependent upon x and z only, and y -derivatives are removed, although x - and z -derivatives remain. The three-dimensional momentum integral equations may be integrated numerically in the x - and z - directions to avoid differentiating the experimentally determined parameters, although unlike the two-dimensional case some differentiation is unavoidable, except for the special case of quasi-two-dimensional flows.

Data sets for three-dimensional flows are obtained much the same way as two-dimensional data sets, except that skin friction values are not as readily determined in three-dimensional flows. Mean velocity fields may be measured using impact or hot-wire probes. Shear fields are more difficult to measure accurately since indirect methods of measuring wall shear stress (Preston tubes, surface fences, razor blades) are developed for use in two-dimensional boundary layers. These devices are calibrated in two dimensional flows, but because of skewing in the boundary layer near the wall, magnitude and direction errors may be introduced. Direct measurements of skin friction may be made using direct force floating element devices which measure both magnitude and direction of wall shear stress. Three-dimensional near-wall similarity may be used to infer wall shear stress from velocity profile measurements after the methods of Pierce and Zimmermann (14). Pierce and McAllister (15) have shown that this

concept provides a useful means of determining wall shear stress for profiles with monotone increasing skew and with skew angles up to about 15-20°, for profiles with an increasing and decreasing skew angle of 10° or less, and for plane of symmetry flow away from separation.

3. Review of Turbulent Boundary Layer Experiments

3.1 Two-Dimensional Experiments

Two-dimensional turbulent boundary layer flows have been extensively examined over the years and are fairly well understood. For the 1968 Stanford Conference, Coles and Hirst (7) examined thirty-three 2DTBL data sets obtained from flows subjected to a wide range of longitudinal pressure gradients. Although additional 2DTBL investigations have been performed since 1968, it was felt that a sufficient number of such flows were presented by Coles and Hirst and a more thorough search for 2DTBL experiments was not pursued. The post-1968 flows which are described here are those which are somewhat different from those presented by Coles and Hirst, or that are of particular interest to this study.

The boundary layer on a large diameter, axisymmetric body was examined by Kong (16). The surface of the body was changed for different flow conditions which included solid and porous smooth surfaces and solid and porous rough surfaces. Measurements of mean velocity and Reynolds stress profiles and direct wall shear measurements were obtained. Strickland and Simpson (17) examined the boundary layers in a separating flow. Mean velocity and turbulence intensity profiles were obtained using hot-film and laser anemometry while mean and fluctuating wall shear distributions were obtained using flush-mounted hot-film sensors. Menna (18), as part of his documentation of the two-dimensionality of the VPI&SU Internal Flow Lab wind tunnel, measured mean velocity profiles across and along the tunnel centerline.

de Brederode and Bradshaw (1) examined the nominally two-dimensional flow in a square duct. Measurements were made in the boundary layer along the tunnel center-plane to determine the minimum tunnel aspect ratio (ratio of tunnel width to boundary layer thickness) below which secondary flow (streamwise vorticity originating near the corners) became significant. Deviations from two-dimensional flow on the tunnel center-plane were assumed to be caused by collateral convergence/divergence of the flow.

3.2 Three-Dimensional Experiments.

In general, 3DTBL experiments may be classified into five categories according to the flow geometry of the experiment as suggested by Vermeulen (19). These are:

- 1) Flow over a swept-wing or plate,
- 2) Stagnation flow on a flat plate (wing-body or strut-body junction),
- 3) Flow in a vortex diffuser (combined source-vortex flow),
- 4) Flow in a curved duct, and
- 5) Flow on rotating bodies.

In addition to these five categories, other flow geometries have been examined, such as wall jets, plane of symmetry flows, and relaxing flows.

Many of the early investigations were conducted to obtain some basic understanding of 3DTBL's. As a result, many of the early investigations lack adequate data sets to be used as test cases

for prediction methods. Wheeler and Johnston (20) examined many of these early investigations and summarized their results, noting the shortcomings of each investigation. This discussion will focus mainly on investigations completed since Wheeler and Johnston's review, although selected studies completed prior to it will be discussed.

Measurements of the flow over infinite swept-wings were made by Etheridge (21), van den Berg and Elsenaar (22), and Elsenaar and Boelsma (23). Etheridge investigated the flow past a 45° swept plate under different adverse pressure gradients. van den Berg and Elsenaar measured mean velocity profiles on a 35° swept flat plate in an adverse pressure gradient. Later, Elsenaar and Boelsma used the same model to obtain measurements of the six components of the Reynolds stress tensor. In both investigations, departure from spanwise two-dimensionality and three-dimensional separation occurred near the trailing edge of the plate. Flows past non-infinite swept-wings/plates were investigated by Zimmermann and Abbott (24) and Bertelrud (25,26). Measurements of the mean velocity and Reynolds stress profiles were made by Zimmermann and Abbott on a yawed flat plate with zero longitudinal pressure gradient. Bertelrud measured Reynolds stress components near the leading edge of an aircraft wing with varying angles of attack behind the separation bubble, and mean velocity profiles further downstream on the main body of the wing.

Stagnation point flows on flat surfaces have been examined by East and Hoxey (27), Luzhanskii and Solntsev (28), Ezekwe (29), Dechow and Felsch (30), Tennant (31), Pierce and McAllister (15), and Menna (18).

East and Hoxey investigated the flow impinging upon a blunt teardrop body protruding from a flat surface. Mean velocity profiles were obtained in the 3DTBL on the flat plate upstream and beside the teardrop. Luzhanskii and Solntsev examined the separation zones of 3DTBL's formed in front of cylindrical and rectangular bodies protruding from flat surfaces. Ezekwe investigated the flow over a flat surface impinging upon a flat wall. Measurements of the mean velocity field and Reynolds stress tensors were obtained on and near the plane of symmetry of the flow. Dechow and Felsch obtained measurements of the mean velocity and Reynolds stress tensor in the 3DTBL growing in front of a cylinder with a streamlined trailing edge standing on a flat wall. Measurements were obtained along a freestream streamline beginning in the quasi-two-dimensional region ahead of the body to the region behind the three-dimensional separation region. Tennant, and Pierce and McAllister investigated the 3DTBL growing ahead of and beside a blunt teardrop body protruding from a flat surface. Measurements included mean velocity profiles and direct measurement of the wall shear stress using an omnidirectional wall shear meter. Menna measured the mean velocity profiles and Reynolds stress components in the 3DTBL around the same model used by Pierce and McAllister.

Curved channel flows were first investigated by Gruschwitz (32). Francis and Pierce (33) measured mean velocity and turbulence intensity profiles on the centerline of the two curved channels. Klinksiek (34), and Duerson (35) investigated the flow in a rectangular recurving channel. Mean velocity measurements along the centerline of the

channel end-wall were obtained by Francis and Pierce and Klinksiek, and mean velocity and Reynolds stress profiles were obtained by Duerson. Vermeulen (19) obtained mean velocity profiles on the end-wall of a rectangular 60° curved duct for zero longitudinal pressure gradient flow and for adverse pressure gradient conditions severe enough to cause separation.

Flows on rotating bodies may be classified into two categories, flows on rotating disks and flows past rotating bodies of revolution or cylinders. An early study of the instability and transition of the boundary layer on rotating disks was performed by Gregory, et. al. (36). Cham and Head (37) investigated the boundary layer on a rotating disk at three different rotational speeds.

Flows past rotating cylinders have been investigated by Parr (38), who measured mean velocity profiles, and Bissonette and Mellor (39) and Lohmann (40) who each measured mean velocity and turbulent stress profiles. These experiments were obtained in an apparatus in which an axial boundary layer was permitted to develop on the surface of a stationary cylindrical body. A rotating cylinder of the same diameter immediately downstream of the stationary body induced the transverse velocity in the boundary layer. Furuya and Nakamura (41) investigated the boundary layer growth on rotating bodies of revolution with hemispherical, streamlined, and conical nose sections. Velocity profiles were measured on the cylindrical portions of the bodies behind the nose sections of the hemispherical and streamlined models, and on the conical nose section.

The five categories of 3DTBL flow experiments are not the only types of flow fields investigated. Shear-driven relaxing flows have been investigated by Nelson (42), Pierce and McAllister (15), Higuchi and Rubesin (43), Hebbar and Melnik (44), and Winkelmann and Melnik (45). Nelson obtained mean velocity profiles and pressure field data in the 3DTBL downstream of 30° and 45° swept-steps. Pierce and McAllister used the same apparatus as Nelson to obtain mean velocity profiles and direct wall shear measurements downstream of the steps. Higuchi and Rubesin investigated the relaxation of the flow from a spinning cylinder onto a stationary cylinder. Measurements obtained included mean velocity profiles and indirect wall shear values. Hebbar and Melnik obtained measurements of the mean velocity and static pressure fields and indirect wall shear measurements in the relaxing 3DTBL downstream of a 30° swept transverse hump faired into the tunnel sidewall. Reynolds stress measurements were incomplete due to traverse limitations of the hot wire probe. Winkelmann and Melnik used basically the same apparatus as Hebbar and Melnik to investigate transverse non-uniformities in the relaxing boundary layer downstream of the hump. To study the non-uniformities, transverse variations of the flow velocity, yaw, pitch, and turbulence intensity were measured in the boundary layer at set distances above the wall.

Other experiments not falling into the five categories have been performed by East and Sawyer (46), Catalano, et. al. (47), and Horne (48). East and Sawyer measured mean velocity profiles and Reynolds stress tensors in the 3DTBL ahead of a 45° swept step. Data were

obtained at stations beginning in the quasi-two-dimensional region ahead of the body up to the region just ahead of three-dimensional separation. Catalano, et. al., obtained pressure and mean velocity field measurements in a three-dimensional wall jet. The experiment was designed to simulate the flowfield created by jet engine exhaust gases directed along the upper surface of a wing. Horne measured the free stream edge and initial conditions of the 3DTBL flow upstream of the blunt teardrop used by Pierce and McAllister. Velocity profiles from both pressure probe and hot-film instrumentation indicated the flow to be essentially two-dimensional.

4. Method of Analysis

The procedure followed when examining the experimental data sets is outlined below.

(1) Each experiment was examined to see whether a momentum integral examination of the data had already been performed, and if not, whether a momentum integral examination could be performed. In order for the examination to be performed, the data measurement grid needed to be oriented in a Cartesian sense and a sufficient number of measurement stations needed to exist when transverse derivatives of flow parameters were required. These requirements usually eliminated flows in curved channels, since, in most cases, data measurements were made along the channel center-line only. Vermeulen (19) took measurements on and off the center-line of a curved channel, and through interpolation, was able to show that his data satisfied the momentum integral equations in a freestream streamline direction.

(2) The freestream velocity, Q , was adjusted to correct for variations in measurement conditions. This was accomplished by utilizing similitude and assuming a constant unit Reynolds number at each measurement station for a particular flow field, i.e.:

$$\text{Re}/L = \frac{Q}{\nu} \Big|_{\text{measured}} = \frac{Q}{\nu} \Big|_{\text{reference}} \quad 4.1$$

A representative value of kinematic viscosity was chosen for each data set with which the reference freestream velocities were

determined. The reference velocities were then plotted and smoothed to reduce the experimental scatter.

(3) Values of the integrated boundary layer parameters were determined by numerically integrating the mean velocity profiles using a trapezoidal integration routine.

(4) In cases where skin friction data was not provided with the data sets, friction velocities were determined using near-wall similarity. The friction velocities for two-dimensional boundary layers and boundary layers on the plane of symmetry were determined using two-dimensional near-wall similarity. Pierce (49) suggested that the scalar form of the Law of the Wall could be used for a plane of symmetry flow since lateral flow does not exist on this plane. The velocity profiles were fitted to Spalding's third order equation between $50 < y^+ < 300$ as suggested by Coles and Hirst (7) for near-zero pressure gradient flows. Wall shear values were corrected to reference conditions using similarity:

$$\frac{c_f}{2} = \frac{\tau_o}{\rho Q^2} \Bigg|_{\text{measured}} = \frac{\tau_o}{\rho Q^2} \Bigg|_{\text{reference}} \quad 4.2$$

The reference freestream velocities used in Eq. 4.2 were obtained from smoothed curves.

Three-dimensional near-wall similarity was not utilized because skin friction data were provided for all skewed velocity profiles. van den Berg and Elsenaar (22) presented skin friction

data obtained indirectly using Stanton tubes which were calibrated in a fully-developed pipe flow. The direction of the wall shear stress was determined with rotatable wall pitots. Elsenaar and Boelsma (23), in the continued investigation of this work, derived skin friction data from interpolation of the smoothed data of van den Berg and Elsenaar. Pierce and McAllister (15) measured the wall shear stress using an omnidirectional, direct force floating element device.

(5) When the momentum integral equations required transverse derivatives of parameters, the parameters were plotted and a curve was smoothed through the data. Derivatives were obtained using a mirror technique. The normal to the curve was determined by placing the mirror normal to the surface of the graph. The mirror was then positioned so that there was no discontinuity in the curve where the actual curve met its mirror image. A straight line was then drawn normal to the first normal (parallel to the curve tangent) and the slope was measured graphically.

(6) The momentum integral examination of each data set, two-dimensional, axisymmetric, and three-dimensional, was accomplished by integrating the three-dimensional momentum integral equations numerically. The equations used:

$$\frac{\partial(Q^2\theta_{11})}{\partial x} + Q\delta_1^* \frac{\partial U}{\partial x} + \frac{\partial(Q^2\theta_{13})}{\partial z} + Q\delta_3^* \frac{\partial U}{\partial z} = \frac{\tau_{0x}}{\rho} \quad 4.3$$

$$\frac{\partial(Q^2\theta_{31})}{\partial x} + Q\delta_1^* \frac{\partial W}{\partial x} + \frac{\partial(Q^2\theta_{33})}{\partial x} + Q\delta_3^* \frac{\partial W}{\partial z} = \frac{\tau_{0z}}{\rho} \quad 4.4$$

are the equivalent of Eqs. 2.35 and 2.36 respectively. The form of the momentum integrals in Eqs. 4.3 and 4.4 was chosen to eliminate two derivative terms on the left side of each equation. These equations could be simplified for the special cases of two-dimensional, axisymmetric (thin boundary layer, constant wall radius assumption), plane of symmetry, or infinite swept-wing flows by introducing assumptions appropriate to each flow field.

When integrating Eqs. 4.3 and 4.4 in the x-direction, the equations were normalized by $(Q^2\theta_{11})_{x_0}$ and $(Q^2\theta_{31})_{x_0}$ respectively, resulting in the relations:

$$\begin{aligned} \frac{(Q^2\theta_{11})_x}{(Q^2\theta_{11})_{x_0}} - 1 + \int_{\frac{u}{Q_{x_0}}|_{x_0}}^{\frac{u}{Q_{x_0}}|_x} \frac{Q\delta_1^*}{(Q\theta_{11})_{x_0}} d\left[\frac{u}{Q_{x_0}}\right] + \int_{\frac{x_0}{\theta_{11x_0}}}^{\frac{x}{\theta_{11x_0}}} \frac{1}{Q^2_{x_0}} \frac{\partial(Q^2\theta_{13})}{\partial z} d\left[\frac{x}{\theta_{11x_0}}\right] \\ + \int_{\frac{x_0}{\theta_{11x_0}}}^{\frac{x}{\theta_{11x_0}}} \frac{Q\delta_3^*}{Q^2_{x_0}} \frac{\partial u}{\partial z} d\left[\frac{x}{\theta_{11x_0}}\right] = \int_{\frac{x_0}{\theta_{11x_0}}}^{\frac{x}{\theta_{11x_0}}} \frac{\tau_{0x}}{\rho Q^2_{x_0}} d\left[\frac{x}{\theta_{11x_0}}\right] \quad 4.5 \end{aligned}$$

$$\begin{aligned}
& \frac{(Q^2\theta_{31})_x}{(Q^2\theta_{31})_{x_0}} - 1 + \int \frac{W}{Q_{x_0}} \Big|_x \frac{Q\delta_1^*}{(Q\theta_{31})_{x_0}} d\left[\frac{W}{Q_{x_0}}\right] + \int \frac{x}{\theta_{31}x_0} \frac{1}{Q^2_{x_0}} \frac{\partial(Q^2\theta_{33})}{\partial z} d\left[\frac{x}{\theta_{31}x_0}\right] \\
& + \int \frac{x}{\theta_{31}x_0} \frac{Q\delta_3^*}{Q^2_{x_0}} \frac{\partial W}{\partial z} d\left[\frac{x}{\theta_{31}x_0}\right] = \int \frac{x}{\theta_{31}x_0} \frac{\tau_{0z}}{\rho Q^2_{x_0}} d\left[\frac{x}{\theta_{31}x_0}\right] \quad 4.6
\end{aligned}$$

Equations 4.3 and 4.4 were integrated in the z-direction in the same manner as above by normalizing by $(Q^2\theta_{13})_{z_0}$ and $(Q^2\theta_{33})_{z_0}$, respectively to give:

$$\begin{aligned}
& \int \frac{z}{\theta_{13}z_0} \frac{1}{Q^2_{z_0}} \frac{\partial(Q^2\theta_{11})}{\partial x} d\left[\frac{z}{\theta_{13}z_0}\right] + \int \frac{z}{\theta_{13}z_0} \frac{Q\delta_1^*}{Q^2_{z_0}} \frac{\partial U}{\partial z} d\left[\frac{z}{\theta_{13}z_0}\right] + \frac{(Q^2\theta_{13})z}{(Q^2\theta_{13})_{z_0}} \\
& - 1 + \int \frac{U}{Q_{z_0}} \Big|_z \frac{Q\delta_3^*}{(Q\theta_{13})_{z_0}} d\left[\frac{U}{Q_{z_0}}\right] = \int \frac{z}{\theta_{13}z_0} \frac{\tau_{0x}}{\rho Q^2_{z_0}} d\left[\frac{z}{\theta_{13}z_0}\right] \quad 4.7
\end{aligned}$$

$$\int_{\frac{z_0}{\theta_{33} z_0}}^{\frac{z}{\theta_{33} z_0}} \frac{1}{Q^2 z_0} \frac{\partial(Q^2 \theta_{31})}{\partial x} d \left[\frac{z}{\theta_{33} z_0} \right] + \int_{\frac{z_0}{\theta_{33} z_0}}^{\frac{z}{\theta_{33} z_0}} \frac{Q \delta_1^*}{Q^2 z_0} \frac{\partial W}{\partial x} d \left[\frac{z}{\theta_{33} z_0} \right] + \frac{(Q^2 \theta_{33}) z}{(Q^2 \theta_{33}) z_0}$$

$$- 1 + \int_{\frac{W}{Q z_0} \Big|_{z_0}}^{\frac{W}{Q z_0} \Big|_z} \frac{Q \delta_3^*}{(Q \theta_{33}) z_0} d \left[\frac{W}{Q z_0} \right] = \int_{\frac{z_0}{\theta_{33} z_0}}^{\frac{z}{\theta_{33} z_0}} \frac{\tau_{0z}}{\rho Q^2 z_0} d \left[\frac{z}{\theta_{33} z_0} \right] \quad 4.8$$

The second integral in Eqs. 4.5 and 4.6 and the third integral in Eqs. 4.7 and 4.8 were obtained by converting from the Riemann integral to the Stieltjes integral. Following Apostol (50), the Riemann-Stieltjes integrals involve two functions $f(x)$ and $\alpha(x)$ denoted by $\int_{\alpha(a)}^{\alpha(b)} f(x) d(\alpha(x))$. This becomes the Riemann integral for the special case of $\alpha(x) = x$. When $\alpha(x)$ has a continuous derivative, the definition is such that the symbol $d(\alpha(x))$ can be interpreted as the differential $\alpha'(x) dx$ and the Stieltjes integral $\int_{\alpha(a)}^{\alpha(b)} f(x) d(\alpha(x))$ becomes the Riemann integral $\int_a^b f(x) \alpha'(x) dx$.

Equations 4.5 through 4.8 were integrated numerically using a trapezoidal integration routine. The trapezoid rule was chosen for simplicity and also because of varied step sizes in

the integration. By integrating the x- and z-momentum integral equations along the same direction, a measure of redundancy in the examination was introduced. Following the terminology of Coles and Hirst (7), the integrated left-hand side of the momentum integral was denoted as PL, the right-hand side as PR. Agreement between the data set and the equations of motion for the nominal flow field was shown when the change in PL over an integration interval equaled the change in PR over the same interval.

5. Results and Discussion

The object of this study was to examine two-dimensional and three-dimensional turbulent boundary layer data sets using momentum integral techniques. A review of 2DTBL and 3DTBL experiments was performed to determine whether a momentum integral examination of the data sets had already been performed and, if not, whether the data sets could be examined using this technique.

After reviewing the available experimental data sets, the following were selected for examination in this study:

Two-Dimensional Data Sets

Kong (16) - two axisymmetric flows

Strickland and Simpson (7) - two zero pressure gradient flows,
one adverse pressure gradient flow

Menna (18) - one favorable pressure gradient flow

Three-Dimensional Data Sets

Horne (48) - one flow upstream of a blunt teardrop body protruding
from a flat surface

Elsenaar and Boelsma (23) - one infinite swept-wing flow

van den Berg and Elsenaar (22) - one infinite swept-wing flow

Pierce and McAllister (15) - the flow in front of and alongside a
blunt teardrop body protruding from a flat surface

The data set of Menna was also examined to determine the effect of slight three-dimensionality in a nominally two-dimensional flow. The data set was examined assuming a plane of symmetry existed in a collateral, spreading/converging flow, and assuming a plane of symmetry existed in a skewed spreading/converging flow.

5.1 Two-Dimensional Data Sets

5.1.1 Kong - Axisymmetric Flows

The two data sets examined here were obtained in the turbulent boundary layer on a smooth, solid cylinder with freestream velocities corresponding to dynamic pressures of 12.7 and 17.8 cm of water. The data sets obtained for the porous and solid dynapore body surface were not examined due to the lack of measured wall shear data. The test body consisted of a cylindrical main body with a streamlined nose section, 4.04 m long and 40.1 cm in diameter. Figure 4 shows the measurement station numbers and locations for both data sets. The large outside diameter of the body was chosen so that possible transverse curvature effects would be minimized by maintaining the ratio of the boundary layer thickness to the body radius at less than 0.1. Actual values ranged from about 0.075 to 0.1175. The boundary layer thicknesses were nominally 1.8 cm in the flow corresponding to a dynamic pressure of 12.7 cm of water and 2.3 cm in the flow corresponding to a dynamic pressure of 17.8 cm of water.

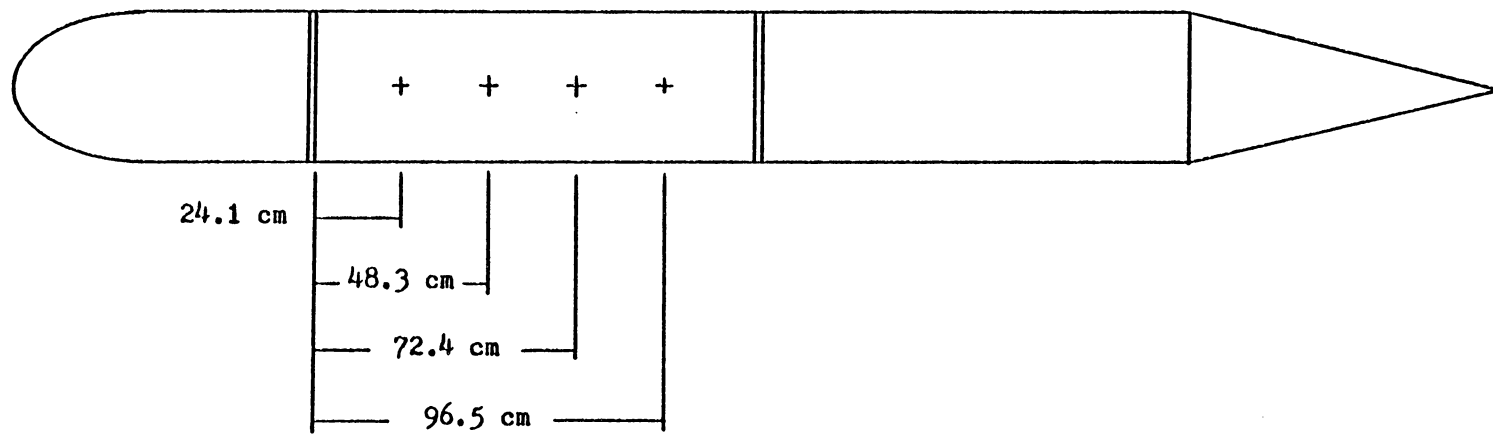


Fig. 4 Measurement Locations for Kong's Axisymmetric Flows

Tabulated data sets obtained from Kong in a private communication included freestream velocity, friction velocity, temperature and pressure, and mean velocity profile values. During the examination of the data, it was noticed that skin friction values tabulated in Kong's dissertation differed slightly from those obtained from the tabulated freestream and friction velocities provided by Kong privately. These differences are shown in Table 1. A slight adverse pressure gradient was also noted when freestream velocities were plotted and smoothed. The largest decreases in freestream velocity occurred between the last measurement stations in both flow fields, amounting to 5% of the initial freestream velocity in the flow corresponding to 12.7 cm of water, and 3% in the flow corresponding to 17.8 cm of water.

The examination the Kong's two flows was performed using both the skin friction data obtained from the dissertation and that from the tabulated friction velocities obtained from Kong privately. The results of the examination are found in Figs. 5 and 6 and in Tables 2 and 3. The 1-8% differences in c_f values appear as 2-7% differences in the PR values of Figs. 5 and 6. In all cases, the data sets appeared to describe flow fields which deviated somewhat from the assumed axisymmetric field.

5.1.2 Strickland and Simpson - Zero Pressure Gradient and Separating Flows

Strickland and Simpson (17) measured their separating flow field using a variety of instruments (pitot tube, slant and horizontal hot-

Table 1. C_f Differences in Kong's Axisymmetric Data Sets

12.7 cm H₂O

x, cm	C_{f_1}	C_{f_2}
24.1	0.00327	0.00304
48.3	0.00299	0.00280
72.4	0.00297	0.00280
96.5	0.00257	0.00266

17.8 cm H₂O

x, cm	C_{f_1}	C_{f_2}
24.1	0.00274	0.00260
48.3	0.00264	0.00253
72.4	0.00257	0.00246
96.5	0.00254	0.00257

C_{f_1} from Dissertation

C_{f_2} from Data Supplied by Kong

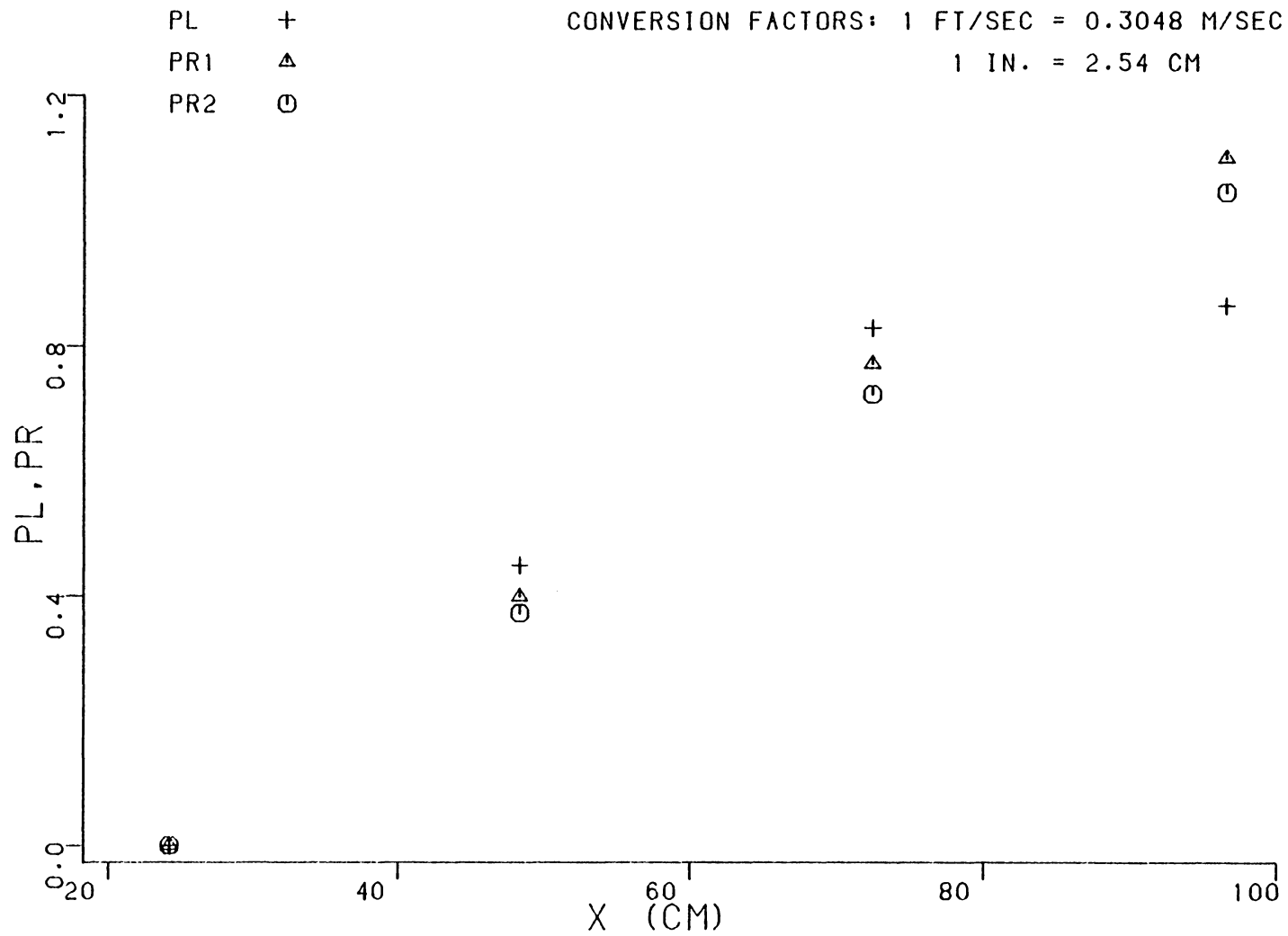


FIG. 5 KONG, 12.7 CM H2O DYNAMIC PRESSURE FLOW

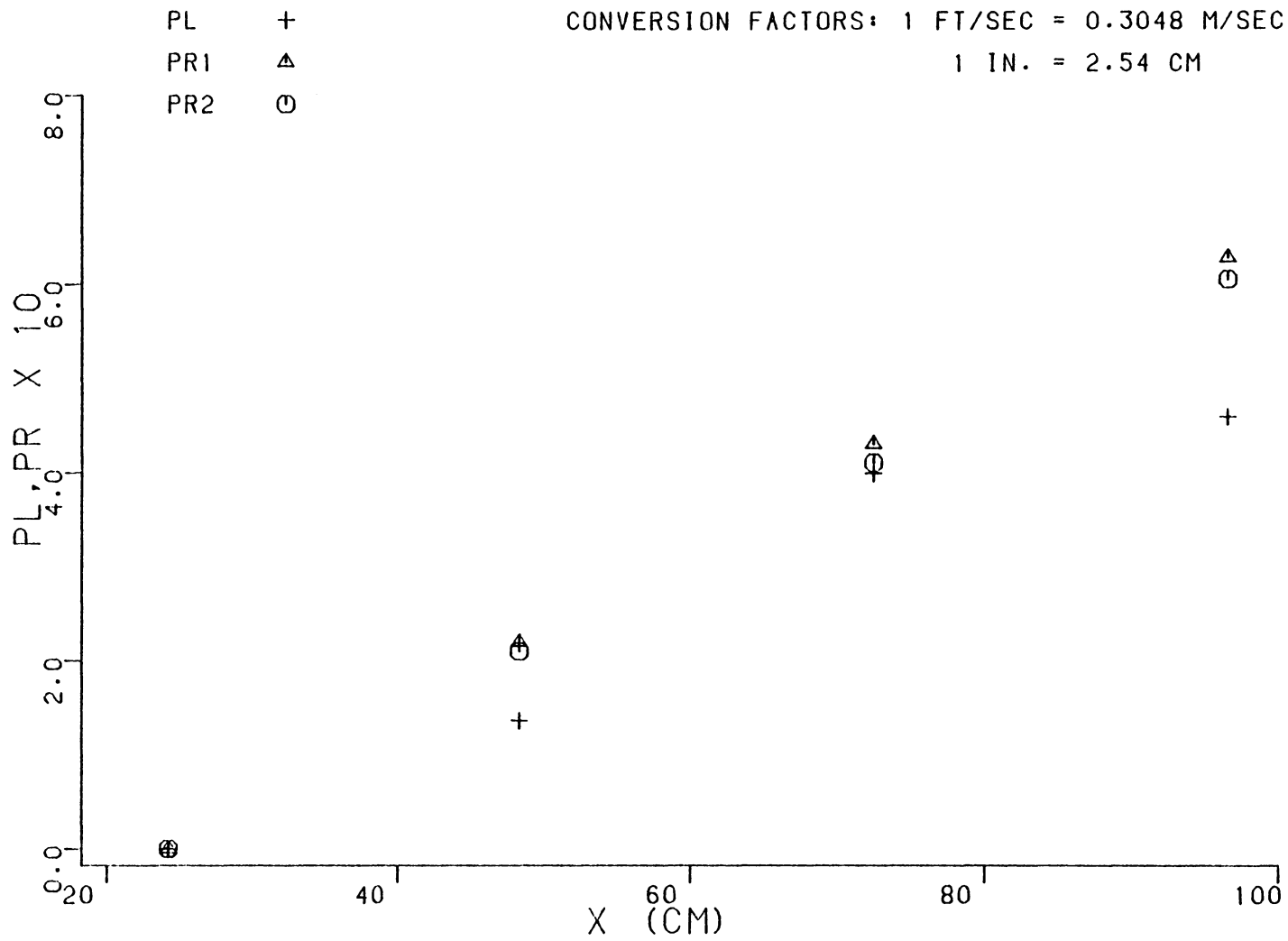


FIG. 6 KONG, 17.8 CM H2O DYNAMIC PRESSURE FLOW

Table 2. PL and PR for Kong's 12.7 cm H₂O Dynamic Pressure Flow

x, cm	PL	PR ₁	PR ₂	Δ PL	Δ PR ₁	Δ PR ₂
24.1	0.0	0.0	0.0			
48.3	0.449	0.399	0.372	0.449	0.399	0.372
72.4	0.829	0.772	0.723	0.380	0.373	0.351
96.5	0.865	1.10	1.05	0.036	0.327	0.322

PR₁ - c_f from Dissertation

PR₂ - c_f from Data Supplied by Kong

Table 3. PL and PR for Kong's 17.8 cm H₂O Dynamic Pressure Flow

x, cm	PL	PR ₁	PR ₂	Δ PL	Δ PR ₁	Δ PR ₂
24.1	0.0	0.0	0.0			
48.3	0.137	0.220	0.210	0.137	0.220	0.210
72.4	0.400	0.431	0.411	0.263	0.211	0.201
96.5	0.460	0.629	0.606	0.061	0.199	0.195

PR₁ - c_f from Dissertation

PR₂ - c_f from Data Supplied by Kong

films, and laser anemometer). Skin friction was measured by Preston tubes and flush mounted hot-films, and determined empirically using both near-wall similarity plots and the Ludwig-Tillmann equation. The data sets obtained using hot-films and the laser anemometer were not examined here because wall shear data locations did not coincide with the velocity profile locations. Boundary layer parameters used in the examination of these flows were calculated by Strickland and Simpson. A comparison of displacement and momentum thicknesses calculated by Strickland and Simpson was made with those determined using a trapezoidal integration of the tabulated profile data, and the differences were found to be less than one percent.

The data sets examined here described two zero pressure gradient flows (different freestream velocities) and one adverse pressure gradient flow. Figure 7 shows the data measurement locations and tunnel geometry for the separating flow. Skin friction data used to examine the separating flow data sets and provided in reference (17) were obtained by Preston tube, near-wall similarity plots, and Ludwig-Tillmann equation. Skin friction data used to examine the zero pressure gradient data sets were obtained by near-wall similarity only. Tabular values of PL and PR for each flow are found in Tables 4 through 6 and are plotted in Figs. 8 through 10. Figure 10 is shown as representative of the results for the separating flow since PR values for the three skin friction data sets differed little.

The zero pressure gradient data sets were obtained primarily to check equipment performance. The data set obtained at $U = 18.3$ m/sec

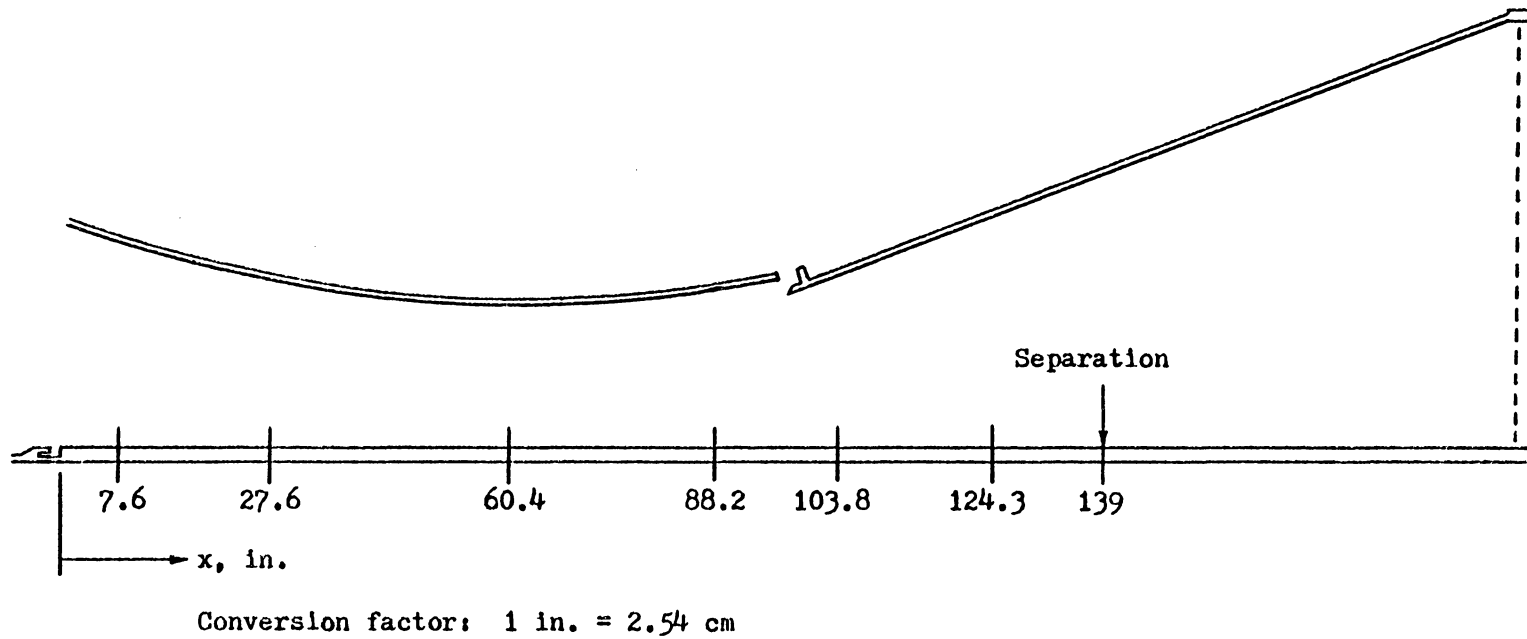


Fig. 7 Measurement Locations for Strickland and Simpson's Separating Flow

Table 4. PL and PR for Strickland and Simpson's 30 ft/sec Zero Pressure Gradient Flow

x, in.	PL	PR
27.7	0.0	0.0
60.4	0.513	0.502
88.4	0.916	0.883
124.7	1.39	1.36
138.7	1.46	1.55
157.1	1.70	1.78
184.0	2.19	2.12

Conversion factors

1 ft/sec = 0.3048 m/sec

1 in. = 2.54 cm

Table 5. PL and PR for Strickland and Simpson's 60 ft/sec
Zero Pressure Gradient Flow

x, in.	PL	PR
27.7	0.0	0.0
60.4	0.388	0.404
88.4	0.700	0.711
124.7	1.06	1.09
157.1	1.37	1.42
184.0	1.65	1.68

Conversion factors

1 ft/sec = 0.3048 m/sec

1 in. = 2.54 cm

Table 6. PL and PR for Strickland and Simpson's
Separating Flow

x, in.	PL	PR ₁	PR ₂	PR ₃	ΔPL	ΔPR ₁	ΔPR ₂	ΔPR ₃
7.6	0.0	0.0	0.0	0.0				
27.6	0.924	0.880	0.890	0.912	0.924	0.880	0.890	0.912
60.4	2.77	2.76	2.73	2.80	1.85	1.88	1.84	1.89
88.2	4.12	4.18	4.11	4.22	1.35	1.42	1.38	1.42
103.8	4.50	4.69	4.58	4.70	0.38	0.51	0.47	0.48
124.3	5.98	4.98	4.82	4.95	1.48	0.29	0.24	0.25

- 1 - c_f from Ludwig-Tillmann Eq.
- 2 - c_f from Near-Wall Similarity
- 3 - c_f from Preston Tube

Conversion factors

1 in. = 2.54 cm

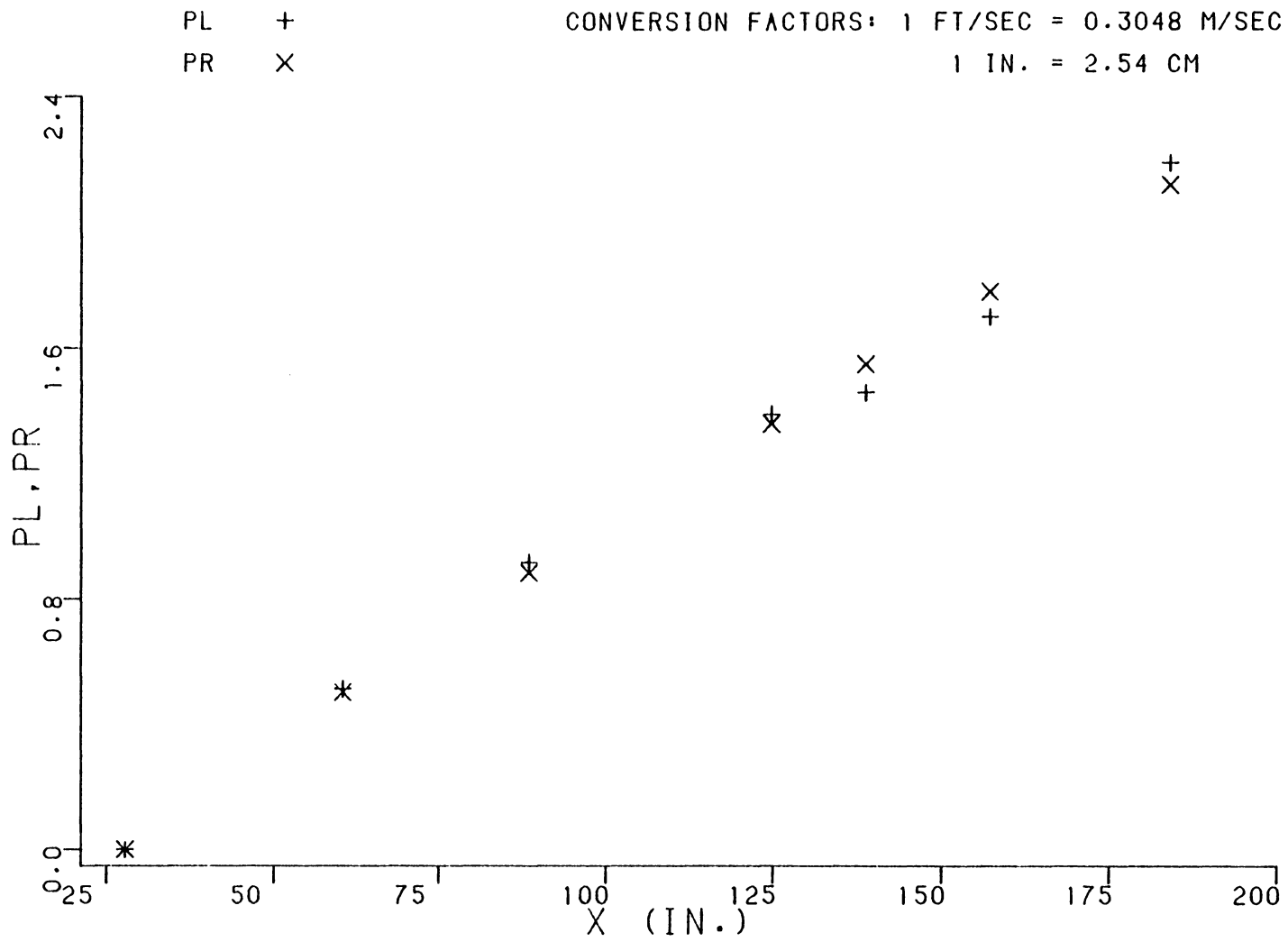


FIG. 8. STRICKLAND AND SIMPSON 30 FPS ZERO PRESSURE GRADIENT FLOW

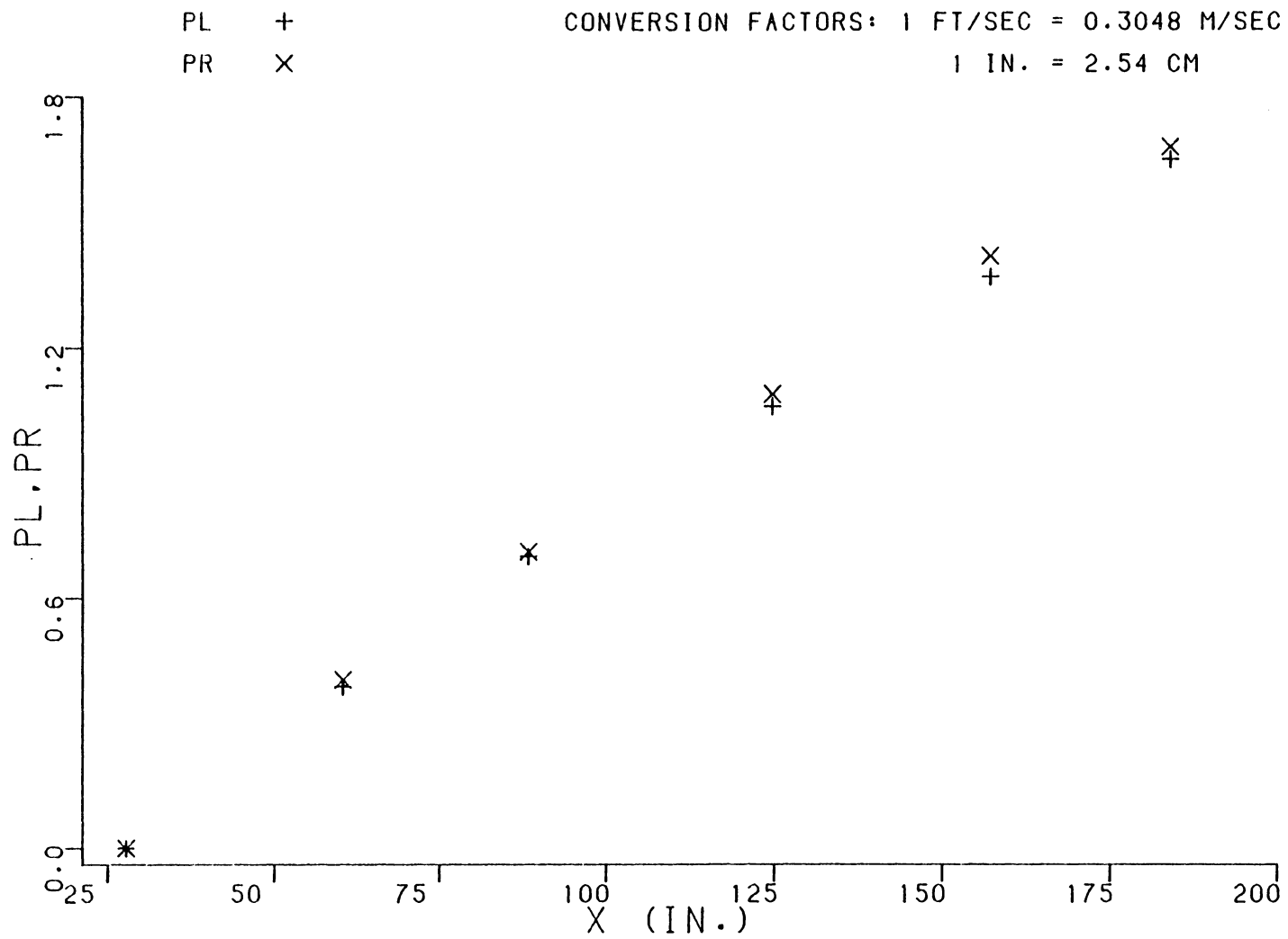


FIG. 9. STRICKLAND AND SIMPSON 60 FPS ZERO PRESSURE GRADIENT FLOW

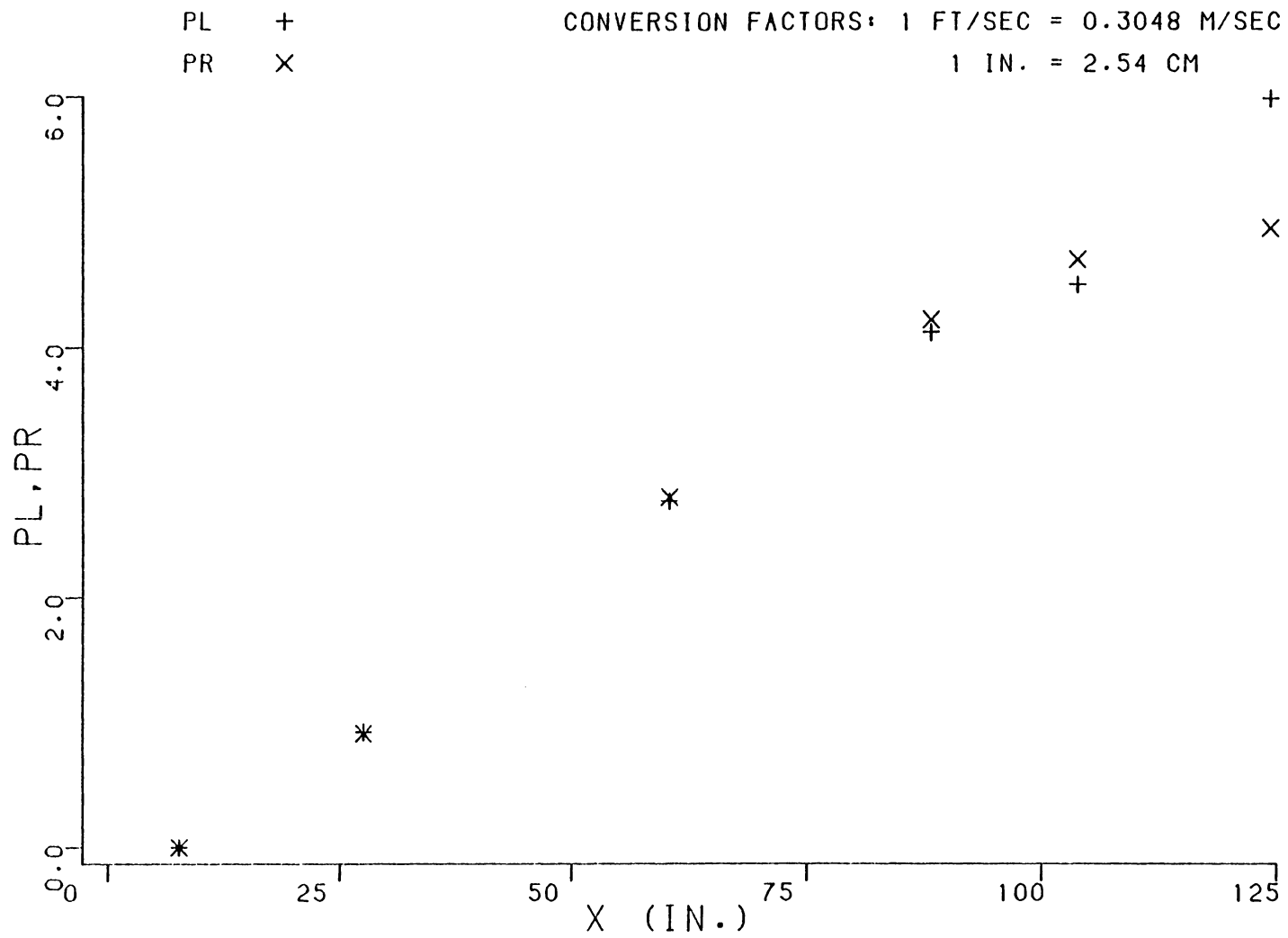


FIG. 10. STRICKLAND AND SIMPSON SEPARATING FLOW

(60 ft/sec)¹ appeared to define a two-dimensional flow field with only minor differences in PL and PR. However, the data set obtained at $U = 9.1$ m/sec (30 ft/sec) appeared to describe a flow field which deviated from two-dimensional flow between $x = 3.17$ m and $x = 3.52$ m ($x = 124.7$ in. and $x = 138.7$ in.) and again between $x = 3.99$ m and 4.67 m ($x = 157.1$ in. and $x = 184.0$ in.).

The separating flow data sets appeared to define a two-dimensional flow field up to $x = 2.24$ m ($x = 88.2$ in.). At x values greater than 2.24 m, as the separation region was approached, PL and PR deviated significantly. This may have been due to the increased influence of Reynolds normal stresses which were not included in this examination.

5.1.3 Menna - Two-Dimensional Flow

Menna (18) measured the flow field in a nominally two-dimensional tunnel in an effort to determine the quality of this flow. Mean velocity profile measurements in the nominally 10 cm (4 in.) thick boundary layer were obtained on the centerline of the 0.61 m x 0.91 m (2 ft. x 3 ft.) tunnel using a three-hole claw probe. After the velocity profiles had been obtained, the claw probe was found to have a slight geometric misalignment not detected when calibrated in a uniform flow. This flaw showed a small skew angle for a very thin layer of the flow near the wall where velocity gradients were largest. This ap-

¹Measurements in parentheses are in the dimensions of the original investigators.

parent skewing of the boundary layer, which typically remained less than two degrees at the wall and went to zero in a very short distance, was judged to be insignificant in the velocity magnitude measurements.

This data set was examined using wall shear values inferred using Coles' (7), NPL (9), and Patel's (8) Law of the Wall constants. A comparison of the friction velocities inferred using each pair of constants is given in Table 7. The data set was also examined using boundary layer parameters determined by a modified Simpson's rule integration and compared with the results obtained using boundary layer parameters determined by trapezoid rule integration. The modified Simpson's rule integration consisted of fitting a parabola through successive sets of three adjacent points in the measured velocity profile, beginning at the wall. The integrals from the first to the second and from the second to the third points were computed using the algebraic equation for the parabola. The triplet of points was then moved one step outward and the process repeated. The two values for each interval (except for the end intervals) were averaged, thus providing some smoothing of the integrals. Table 8 provides a comparison of boundary layer parameters calculated using both trapezoid and the modified Simpson's integration.

The results of the examinations of this data set are shown in Fig. 11 with tabular values of PL and PR found in Tables 9 and 10. As seen in Table 9, values of PL and PR obtained using boundary layer parameters determined by modified Simpson's rule integration did not differ significantly from the values obtained with trapezoid-rule-integrated

Table 7. Menna, Friction Velocity Comparison

x, in.	u_{COLES}^*	u_{PATEL}^*	u_{NPL}^*
0	2.859	2.838	2.955
12	2.804	2.784	2.899
24	2.834	2.813	2.930
36	2.837	2.816	2.932
48	2.816	2.795	2.910
60	2.808	2.787	2.902
72	2.815	2.794	2.909
84	2.758	2.737	2.850
96	2.821	2.799	2.915

Note: Dimensions for u^* are ft/sec

Conversion factors

1 ft/sec = 0.3048 m/sec

1 in. = 2.54 cm

Table 8. Menna, Boundary Layer Parameter Comparison

x, in.	$\delta_1^{* a}$	$\delta_1^{* b}$	θ_{11}^a	θ_{11}^b
0	0.288	0.292	0.211	0.214
12	0.317	0.321	0.233	0.235
24	0.339	0.344	0.250	0.252
36	0.366	0.371	0.270	0.272
48	0.383	0.388	0.283	0.285
60	0.408	0.413	0.302	0.305
72	0.432	0.438	0.321	0.324
84	0.469	0.476	0.348	0.352
96	0.465	0.472	0.349	0.353

a - Modified Simpson's Rule Integration

b - Trapezoid Rule Integration

Note: Dimensions for δ_1^* and θ_{11} are inches.

Conversion factor

1 in. = 2.54 cm

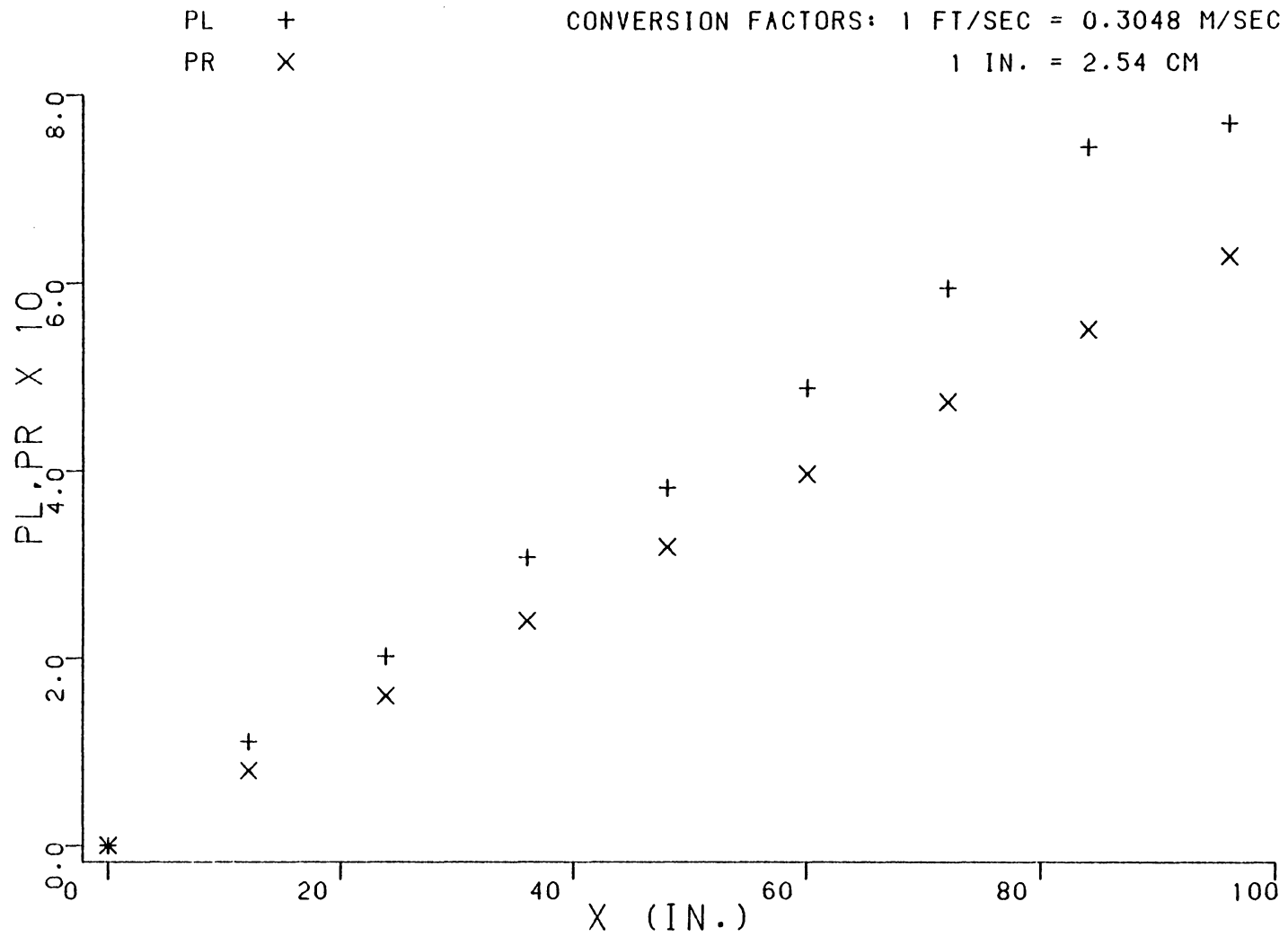


FIG. 11. MENNA TWO-DIMENSIONAL FLOW

Table 9. PL and PR for Menna's Two-Dimensional Flow. A Comparison Using Different Boundary Layer Parameter Integration Techniques.

x, in.	PL ₁	PL ₂	PR ₁	PR ₂	ΔPL ₁	ΔPL ₂	ΔPR ₁	ΔPR ₂
0	0.0	0.0	0.0	0.0				
12	0.111	0.114	0.074	0.076	0.111	0.114	0.074	0.076
24	0.202	0.208	0.148	0.152	0.091	0.094	0.074	0.076
36	0.308	0.315	0.221	0.228	0.106	0.107	0.073	0.075
48	0.382	0.389	0.294	0.302	0.074	0.074	0.073	0.075
60	0.489	0.495	0.366	0.376	0.106	0.107	0.072	0.074
72	0.595	0.600	0.438	0.450	0.107	0.105	0.071	0.073
84	0.745	0.749	0.509	0.523	0.150	0.148	0.071	0.073
96	0.770	0.772	0.580	0.597	0.025	0.024	0.072	0.074

1 - Parameters from Trapezoidal Integration

Conversion factor

2 - Parameters from Modified Simpson's Integration

1 in. = 2.54 cm

Table 10. PL and PR for Menna's Two-Dimensional Flow. A Comparison Using Friction Velocities Inferred from Different Law of the Wall Constants

x, in.	PL	PR ₁	PR ₂	PR ₃	ΔPL	ΔPR ₁	ΔPR ₂	ΔPR ₃
0	0.0	0.0	0.0	0.0				
12	0.111	0.080	0.075	0.074	0.111	0.080	0.075	0.074
24	0.202	0.160	0.150	0.148	0.091	0.080	0.075	0.074
36	0.308	0.240	0.225	0.221	0.106	0.080	0.074	0.073
48	0.382	0.319	0.298	0.294	0.074	0.079	0.074	0.073
60	0.489	0.397	0.372	0.366	0.106	0.078	0.073	0.072
72	0.595	0.474	0.444	0.438	0.107	0.077	0.072	0.071
84	0.745	0.551	0.516	0.508	0.150	0.077	0.072	0.071
96	0.770	0.629	0.589	0.580	0.025	0.078	0.073	0.072

- 1 - NPL Staff (9) Constants
- 2 - Coles (7) Constants
- 3 - Patel (8) Constants

Conversion factor
1 in. = 2.54 cm

parameters. The wall shear stress values inferred from the different Law of the Wall constants produced somewhat larger changes in PR , although still not significant. Figure 11 shows PL and PR_3 values from Table 10 as representative of these results. The velocity profiles tended to follow the third order Spalding curve best when NPL staff constants were used, which may explain why the $PL - PR$ results utilizing these constants agreed best when compared to the $PL - PR$ comparisons using the Coles or Patel constants. Irrespective of the small differences among the various sets of PL and PR values in Tables 9 and 10, these results are consistent in that they all indicate that this flow deviates somewhat from a true two-dimensional flow.

5.2 Nominally Two-Dimensional Flow With Slight Three-Dimensionality

As noted earlier, the construction of a truly two-dimensional experimental flow is a difficult task. Several investigations (1), (2), (3) have shown that small amounts of three-dimensionality may exist in even the most carefully controlled two-dimensional flows. Since the momentum integral examination of the two-dimensional data set of Menna (18) indicated the presence of some three-dimensionality, it was desired to quantify the amount of secondary flow that might be present in this particular flow field. Assuming a plane of symmetry on the tunnel centerline, the flow was examined as if it were in a collateral, diverging/converging flow (see Fig. 12) and in a skewed diverging/converging flow (see Figs. 13 and 14).

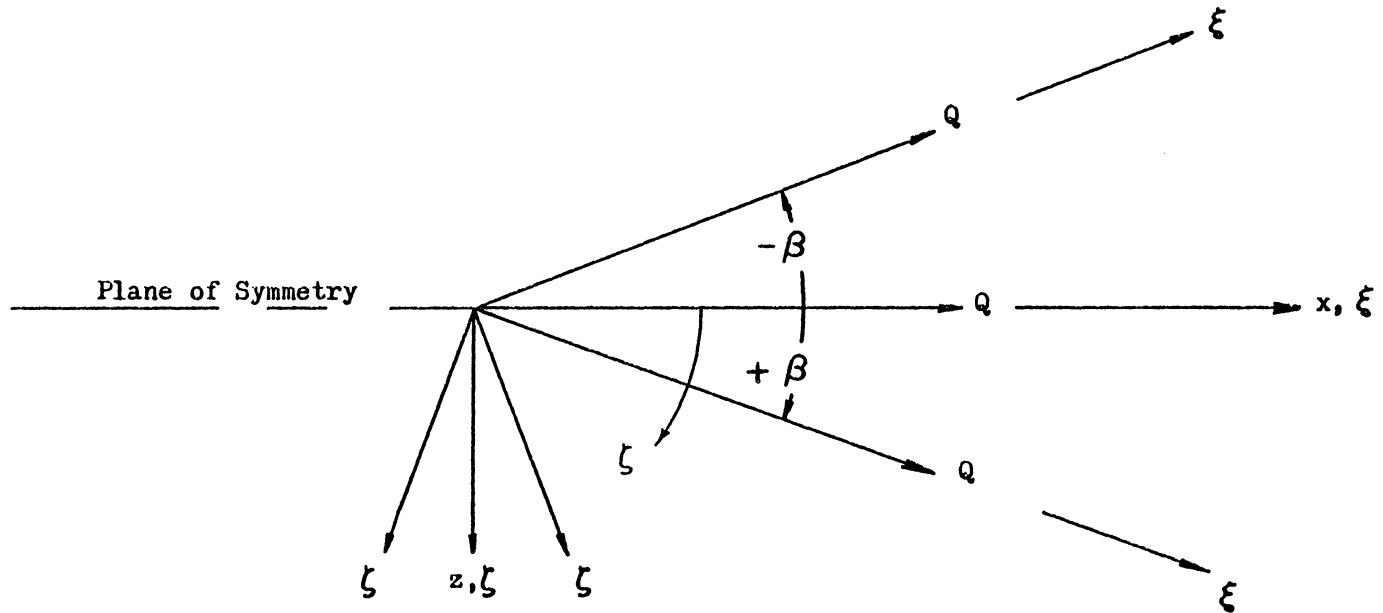


Fig. 12 Coordinate Systems for Plane of Symmetry in a Collateral Spreading Flow

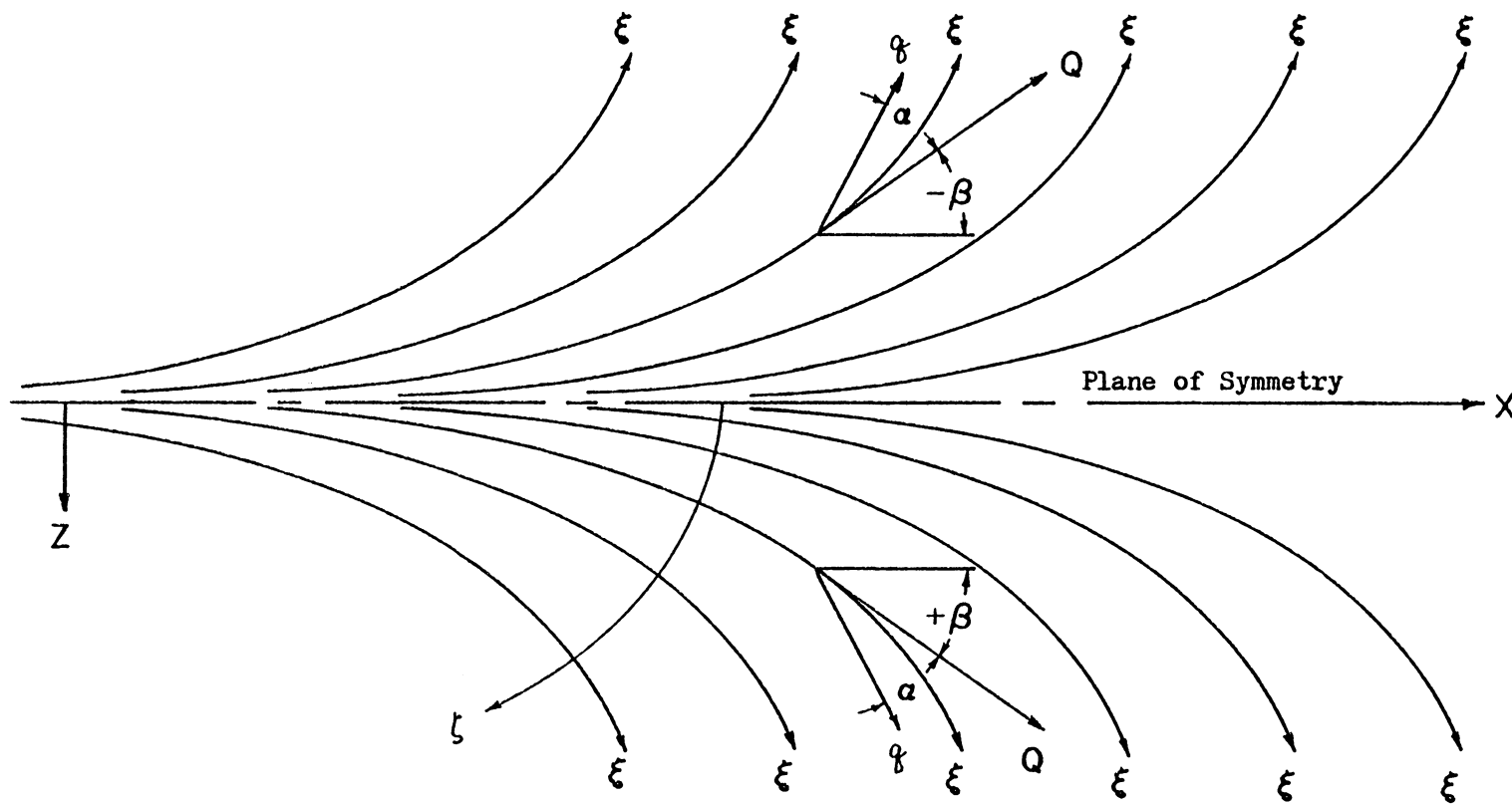


Fig. 13 Freestream Streamline Map for Skewed Spreading Flow on a Plane of Symmetry

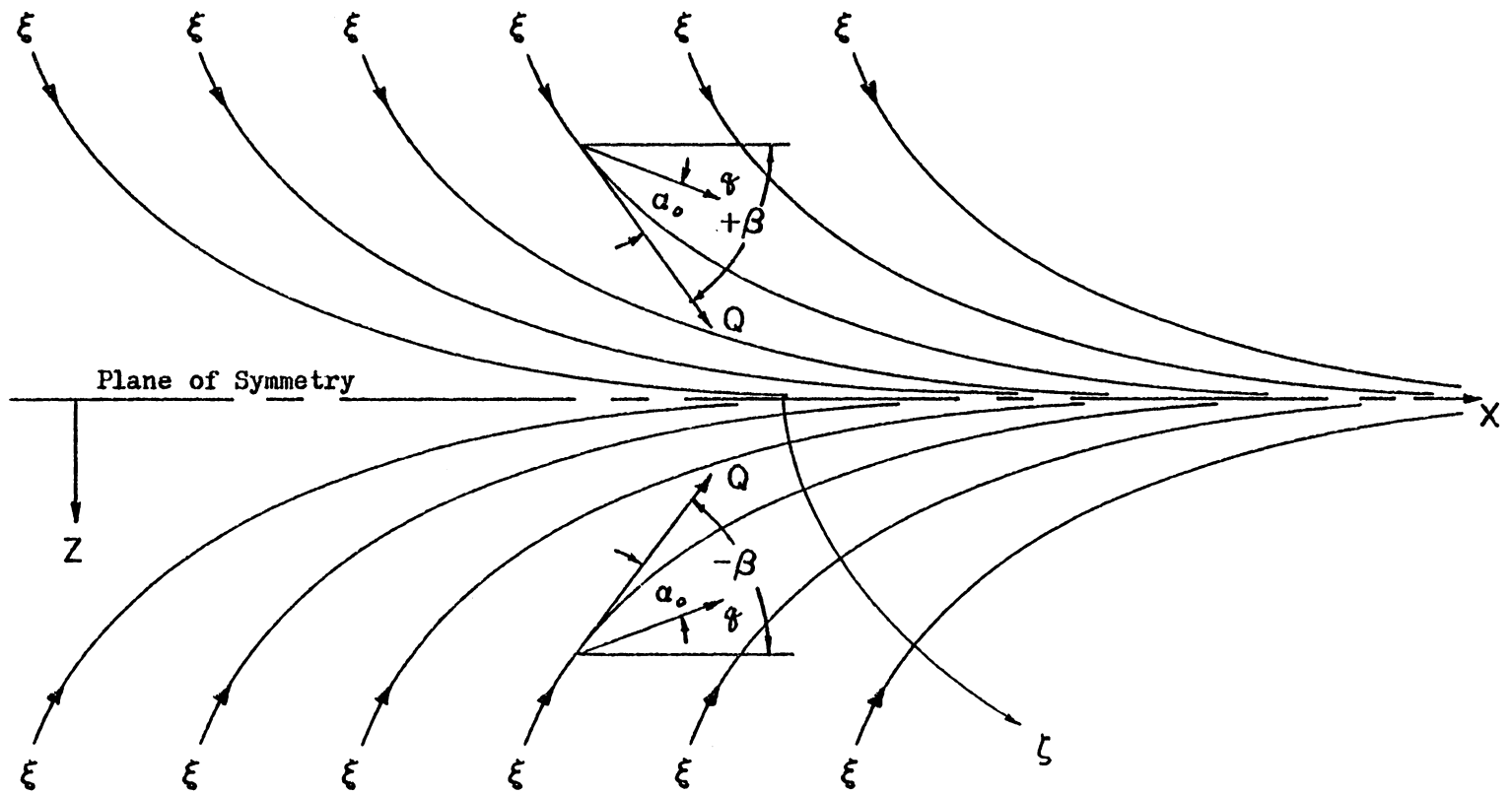


Fig. 14 Freestream Streamline Map for Skewed Converging Flow on a Plane of Symmetry

5.2.1 Menna - Assumed Plane of Symmetry in Collateral Flow

The plane of symmetry assumption required an approximation of $\frac{\partial(Q^2\theta_{13})}{\partial z}$ in Eq. 4.3. Assuming the freestream velocity to be constant across the tunnel, the derivative could be expressed as $Q^2 \frac{\partial\theta_{13}}{\partial z}$. As discussed previously, the $\frac{\partial\theta_{13}}{\partial z}$ term of the Cartesian system is the equivalent of the two terms $\frac{1}{h_3} \frac{\partial\theta_{\xi\zeta}}{\partial\zeta}$ and $\frac{\theta_{\xi}}{h_3} \frac{\partial\beta}{\partial\zeta}$ of the curvilinear set. For the collateral flow assumption, $\theta_{\xi\zeta}$ is zero by definition, leaving only one new term in the momentum integral equation. Since $\theta_{\xi} = \theta_{11}$ on the plane of symmetry by definition, an approximation of $\frac{1}{h_3} \frac{\partial\beta}{\partial\zeta}$ was needed. Derivatives in the z- and ζ -directions are not equal, even on the plane of symmetry. However, assuming small amounts of convergence or divergence of the freestream streamlines, $\frac{1}{h_3} \frac{\partial\beta}{\partial\zeta}$ could be approximated by the term $\frac{\partial\beta}{\partial z}$ near the plane of symmetry. The term $\frac{\partial(Q^2\theta_{13})}{\partial z}$ in Eq. 4.3 could then be replaced by the term $Q^2\theta_{11} \frac{\partial\beta}{\partial z}$, for the above assumptions.

The desired result of this effort, assuming the data set was obtained on the plane of symmetry in a collateral spreading flow, was to determine the divergence (convergence) of the freestream streamlines away from (towards) the plane of symmetry. This was done by approximating $\frac{\partial\beta}{\partial z}$, the rate of divergence (convergence) of the flow field from the plane of symmetry. Rearranging Eq. 4.3 gives:

$$Q^2\theta_{11} \frac{\partial\beta}{\partial z} = \frac{\tau_0}{\rho} - \left[\frac{\partial(Q^2\theta_{11})}{\partial x} + U \delta_1^* \frac{\partial U}{\partial x} \right] \quad 5.1$$

Integrating Eq. 5.1 along the tunnel centerline and normalizing by $(Q^2 \theta_{11})_{x_0}$ gives:

$$\int_{x_0}^x \frac{\theta_{11}}{\theta_{11x_0}} \cdot \frac{Q^2 \theta_{11} \frac{\partial \beta}{\partial z}}{Q^2_{x_0}} d \left[\frac{x}{\theta_{11x_0}} \right] = PR - PL \quad 5.2$$

where PL and PR were obtained from the two-dimensional examination of the data set. By performing the integration numerically using the trapezoid rule and assuming a constant rate of divergence over each x-interval, $\frac{\partial \beta}{\partial z}$ could be determined. Using the sign convention of Fig. 12, divergence of the flow resulted in $\frac{\partial \beta}{\partial z} > 0$, while $\frac{\partial \beta}{\partial z} < 0$ indicated convergence of the flow.

This approach was in agreement with de Brederode and Bradshaw's (1) investigation of slight secondary flow in nominally two-dimensional flows. The effects of the growth of side wall boundary layers and secondary corner flows were considered as induced by a collinear convergence or divergence on the duct center-plane. The imbalance of the von Karman momentum integral equation was represented by:

$$\frac{\theta_{11}}{x-x_0} = \frac{c_f}{2} - \left\{ \frac{d\theta_{11}}{dx} + \frac{(2\theta_{11} + \delta_1^*)}{U} \frac{dU}{dx} \right\} \quad 5.3$$

where x_0 was the virtual origin of the flow. Values of x_0 greater than x indicated convergence of the flow, whereas divergence was indicated by values of x_0 less than x .

The approximate divergence rates, $\frac{\partial \beta}{\partial z}$, for each x -interval of Menna's data set are found in Table 11. The examination showed the flow field alternating between convergence and divergence at the center plane, tending more towards convergence. An overall best fit (visual) of PL and PR was found by assuming a constant freestream convergence of 0.21 deg/cm (1/12 deg/in.) at each measurement station. The results obtained using this assumption are found in Fig. 15 and Table 12. These small amounts of convergence would be difficult to measure with the existing traverse mechanism used by Menna.

5.2.2 Menna - Assumed Plane of Symmetry in Skewed Flow

As noted before, the momentum integral equation for plane of symmetry flows requires one term more than the two-dimensional equation. This term, $\frac{\partial \theta_{13}}{\partial z}$ for the Cartesian system, is the equivalent of the two terms $\frac{1}{h_3} \frac{\partial \theta_{\xi\zeta}}{\partial \zeta}$ and $\frac{\theta_{\xi}}{h_3} \frac{\partial \beta}{\partial \zeta}$ of the curvilinear set. The first term, $\frac{1}{h_3} \frac{\partial \theta_{\xi\zeta}}{\partial \zeta}$, is a result of skewing in the boundary layer. The other term, $\frac{\theta_{\xi}}{h_3} \frac{\partial \beta}{\partial \zeta}$, is a result of spreading of the freestream streamlines. Although on the plane of symmetry $\theta_{\xi\zeta}$ is zero by definition, $\frac{1}{h_3} \frac{\partial \theta_{\xi\zeta}}{\partial \zeta}$ is not. Since the velocity profiles off the tunnel centerline were not measured, the profiles were assumed to be described by Mager's (51) power-law profile model of the 3DTBL. This model approximates the boundary layer profile by:

Table 11. Average Collateral Convergence/Divergence of Menna's Assumed Plane of Symmetry Flow

$x_i - x_{i+1}$, in.	$\frac{\partial\beta}{\partial z}$, $\frac{\text{deg.}}{\text{in.}}$
0 - 12	- 1/7.1
12 - 24	- 1/23
24 - 36	- 1/9.8
36 - 48	1/58
48 - 60	- 1/11
60 - 72	- 1/11
72 - 84	- 1/4.7
84 - 96	1/6.8

Conversion factor

1 in. = 2.54 cm

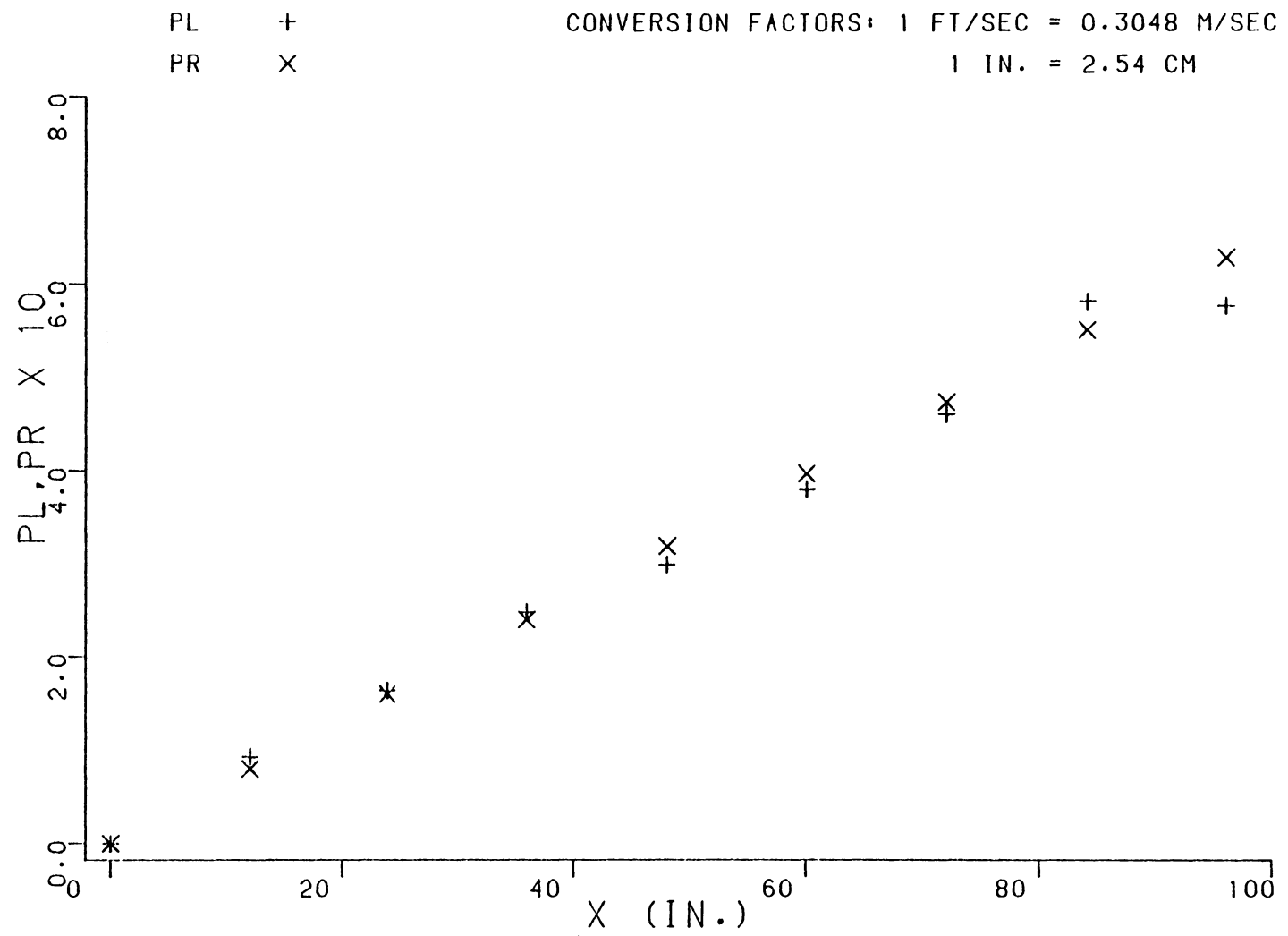


FIG. 15 MENNA, ASSUMED 1/12 DEG/IN. COLLATERAL FREESTREAM CONVERGENCE

Table 12. PL and PR for Menna's Assumed Collateral Plane of Symmetry Flow. Assumes Freestream Convergence = 1/12 deg./in.

x,in	PL	PR
0	0.0	0.0
12	0.093	0.080
24	0.164	0.160
36	0.248	0.240
48	0.299	0.319
60	0.380	0.397
72	0.461	0.474
84	0.582	0.551
96	0.577	0.629

Conversion factor:

1 in. = 2.54 cm

$$\frac{u_s}{Q} = \left\{ \frac{y}{\delta} \right\}^{\frac{1}{n}} \quad 5.4$$

$$\frac{w_s}{Q} = \left\{ \frac{y}{\delta} \right\}^{\frac{1}{n}} \left\{ 1 - \frac{y}{\delta} \right\}^2 \tan \alpha_0 \quad 5.5$$

where,

u_s = velocity in ξ -direction

w_s = velocity in ζ -direction

α_0 = skew angle at the wall (measured with respect to ξ -direction).

The boundary layer thickness, δ , was approximated at each station by the average of eight displacement thicknesses and eleven momentum thicknesses as suggested by White (5). The value of n for each profile was approximated by fitting the measured velocity profile to the power-law streamwise profile and averaging values of n over the interval $0.01 < y/\delta < 0.1$.

The term $\frac{1}{h_3} \frac{\partial \theta_{\xi\zeta}}{\partial \zeta}$ was evaluated by first substituting Eqs. 5.4 and 5.5 into the definition for $\theta_{\xi\zeta}$. Performing the integration for $\theta_{\xi\zeta}$ across the boundary layer yielded:

$$\theta_{\xi\zeta} = \delta \tan \alpha_0 \Phi \quad 5.6$$

where,

$$\Phi = \frac{n}{n+1} - \frac{2n}{2n+1} + \frac{n}{3n+1} - \frac{n}{n+2} + \frac{2n}{2n+2} - \frac{n}{3n+2}$$

Again approximating $\frac{1}{h_3} \frac{\partial}{\partial \zeta}$ by $\frac{\partial}{\partial z}$ near the plane of symmetry for small convergence/divergence of the flow, and assuming that δ and n were functions of x only, then:

$$\frac{1}{h_3} \frac{\partial \theta_{\xi \zeta}}{\partial \zeta} \approx \phi \delta \sec^2 \alpha_0 \frac{\partial \alpha_0}{\partial z} \quad 5.7$$

Assuming that $Q = Q(x)$ only, the term $\frac{\partial(Q^{2\theta_{13}})}{\partial z}$ of Eq. 4.3 was approximated by:

$$\frac{\partial(Q^{2\theta_{13}})}{\partial z} \approx Q^2 \theta_{11} \frac{\partial \beta}{\partial z} + \delta \phi \sec^2 \alpha_0 \frac{\partial \alpha_0}{\partial z} \quad 5.8$$

The procedure for finding the skewing in the boundary layer which would account for the differences in PL and PR in the two-dimensional examination was not as simple as that used when the collateral flow assumption was made. This was due to the presence of two independent terms, $\frac{\partial \beta}{\partial z}$ and $\frac{\partial \alpha_0}{\partial z}$ in the momentum integral equation, rather than one. Instead of back-solving for $\frac{\partial \beta}{\partial z}$ and $\frac{\partial \alpha_0}{\partial z}$ from the known difference between PL and PR, constant values of $\frac{\partial \beta}{\partial z}$ and $\frac{\partial \alpha_0}{\partial z}$ were assumed to exist throughout the flow field. The plane of symmetry momentum integral was then integrated and the results examined to determine where the assumed parameters account for departure from two-dimensional flow.

The combinations of $\frac{\partial \beta}{\partial z}$ and $\frac{\partial \alpha_0}{\partial z}$ which were considered are listed in Table 13. The sign conventions used in each case are as shown in Figs. 13 and 14, with values of $\frac{\partial \beta}{\partial z} > 0$ corresponding to a spreading flow field and values of $\frac{\partial \beta}{\partial z} < 0$ corresponding to a converging flow field. Values of $\frac{\partial \alpha_0}{\partial z}$ must be greater than zero for a flow without

Table 13. Freestream Spreading and Skewing Rates of Menna's Assumed Plane of Symmetry Flow

Case Number	$\frac{\text{deg.}}{\text{in.}}$	$\frac{\text{deg.}}{\text{in.}}$
1	1/16	1/16
2	- 1/16	1/16
3	- 1/8	1/16
4	- 1/8	1/8
5	- 1/4	1/16
6	- 1/4	1/8
7	- 1/4	1/4

Conversion factor

1 in. = 2.54 cm

recurving freestream streamlines since α_0 must turn towards the center of curvature of the freestream streamlines.

The results of the examination of each assumed case are found in Figs. 16 through 22 and in Table 14. The case 3 assumption appeared to best account for the departure from two-dimensionality of the flow field over the entire integration distance, while other cases better accounted for the departure from two-dimensional flow over individual integration intervals. Figures 18 and 19 and Table 15 show the effect of the $\frac{\partial \beta}{\partial z}$ and $\frac{\partial \alpha_0}{\partial z}$ terms on the PL values for cases 3 and 4. The dominant effect is that due to the slight convergence of the freestream streamlines rather than the skewing of the velocity profile. Again, these small amounts of skewing and freestream convergence would prove difficult to measure near the plane of symmetry utilizing existing traverse mechanisms.

5.3 Three-Dimensional Layer Data Sets

5.3.1 Horne - Upstream Initial and Edge Conditions

Horne (48) measured the freestream initial and edge conditions and boundary layer velocity profiles upstream of the teardrop body used by Pierce and McAllister (15). Measurements were obtained on the centerline of the 0.61 m high by 0.91 m wide (2 ft. x 3 ft.) tunnel in the quasi-two-dimensional flow field ahead of the body. The locations of data measurement stations are shown in Fig. 23. The data set was examined assuming the flow field to be nominally two-dimensional. The amounts of collateral divergence or convergence of the freestream which

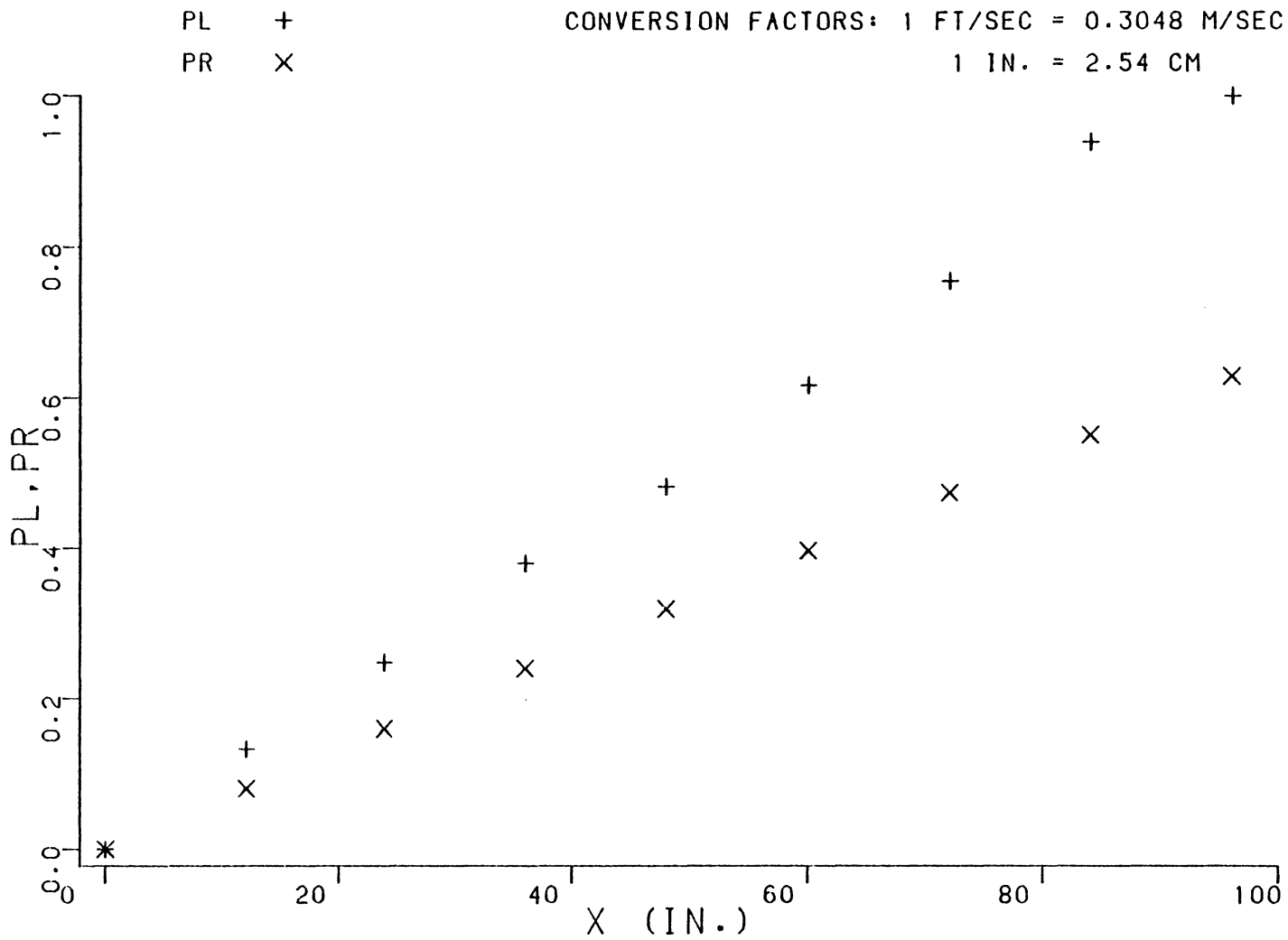


FIG. 16. MENNA SKEWED PLANE OF SYMMETRY, CASE NO. 1

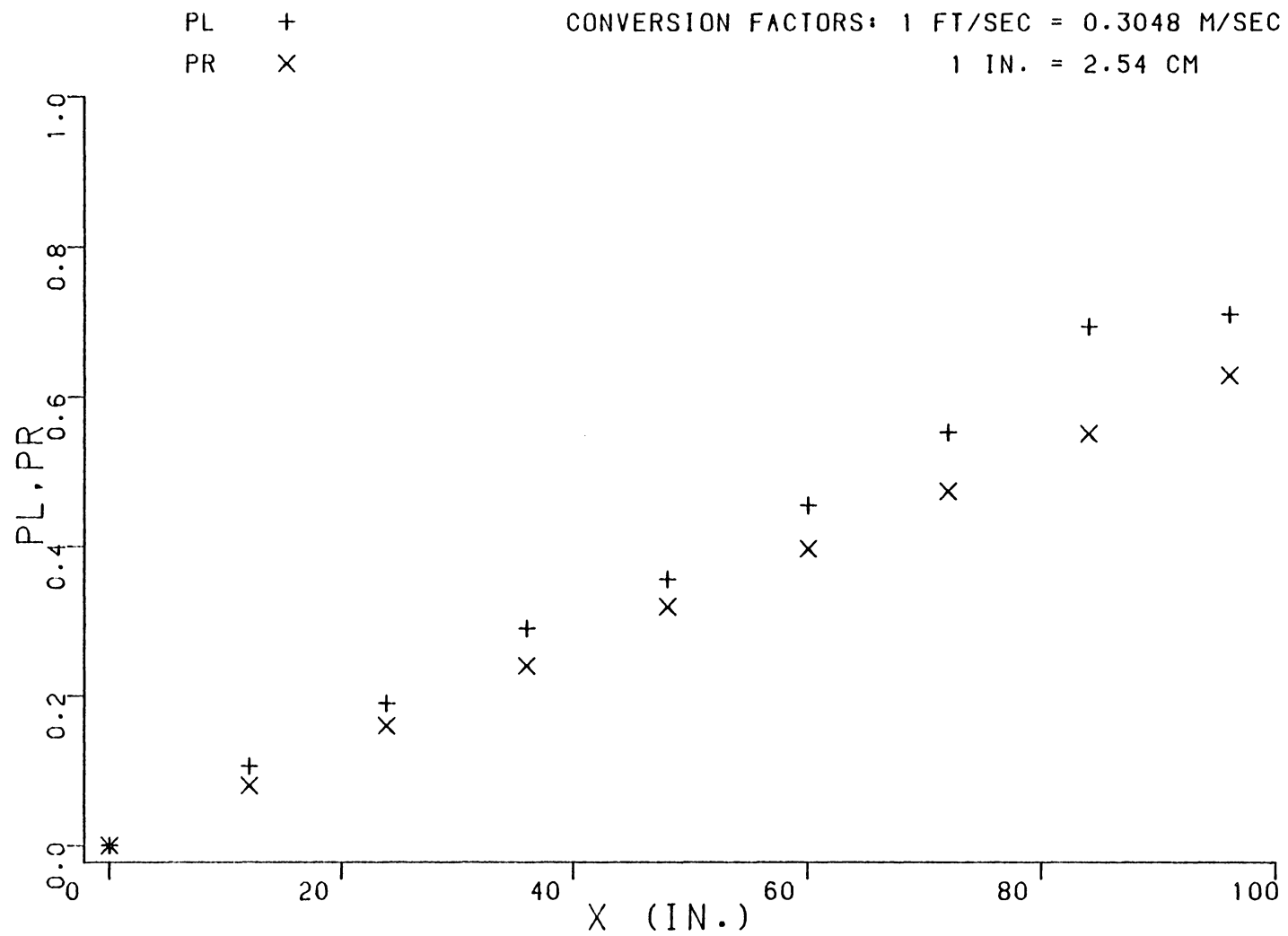


FIG. 17. MENNA SKEWED PLANE OF SYMMETRY, CASE NO. 2

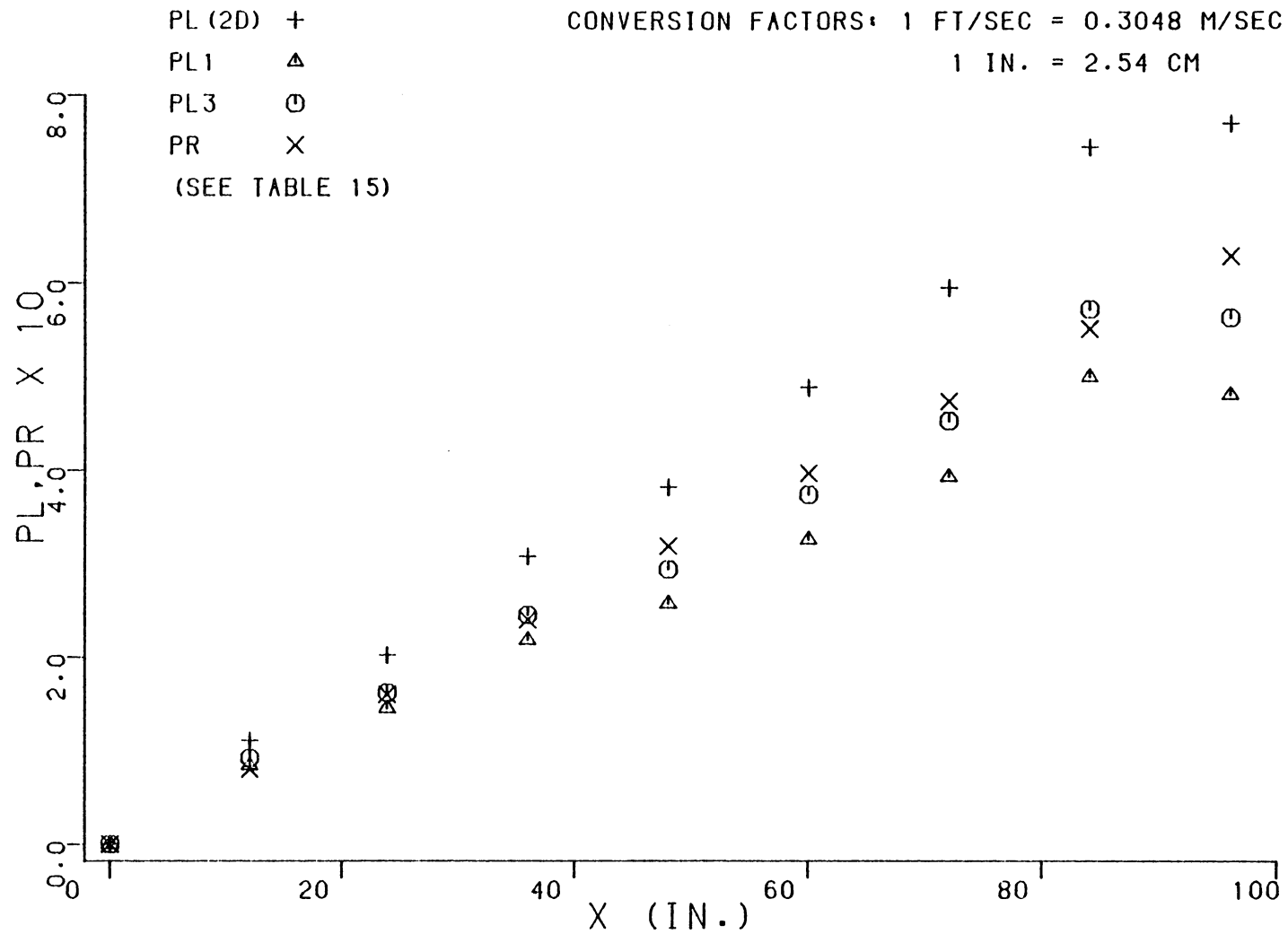


FIG. 18 MENNA, SKEWED PLANE OF SYMMETRY, CASE NO. 3

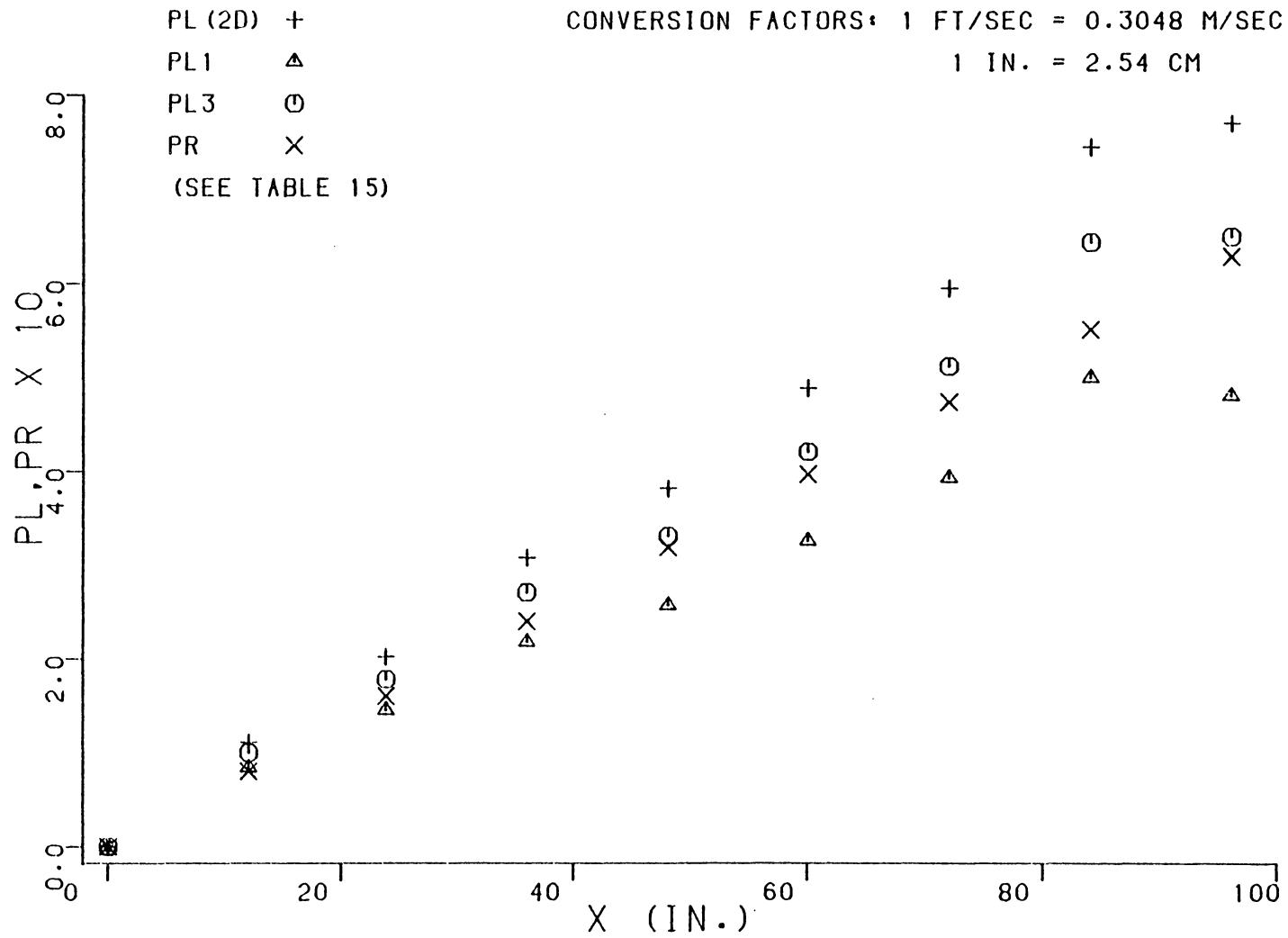


FIG. 19 MENNA, SKEWED PLANE OF SYMMETRY, CASE NO. 4

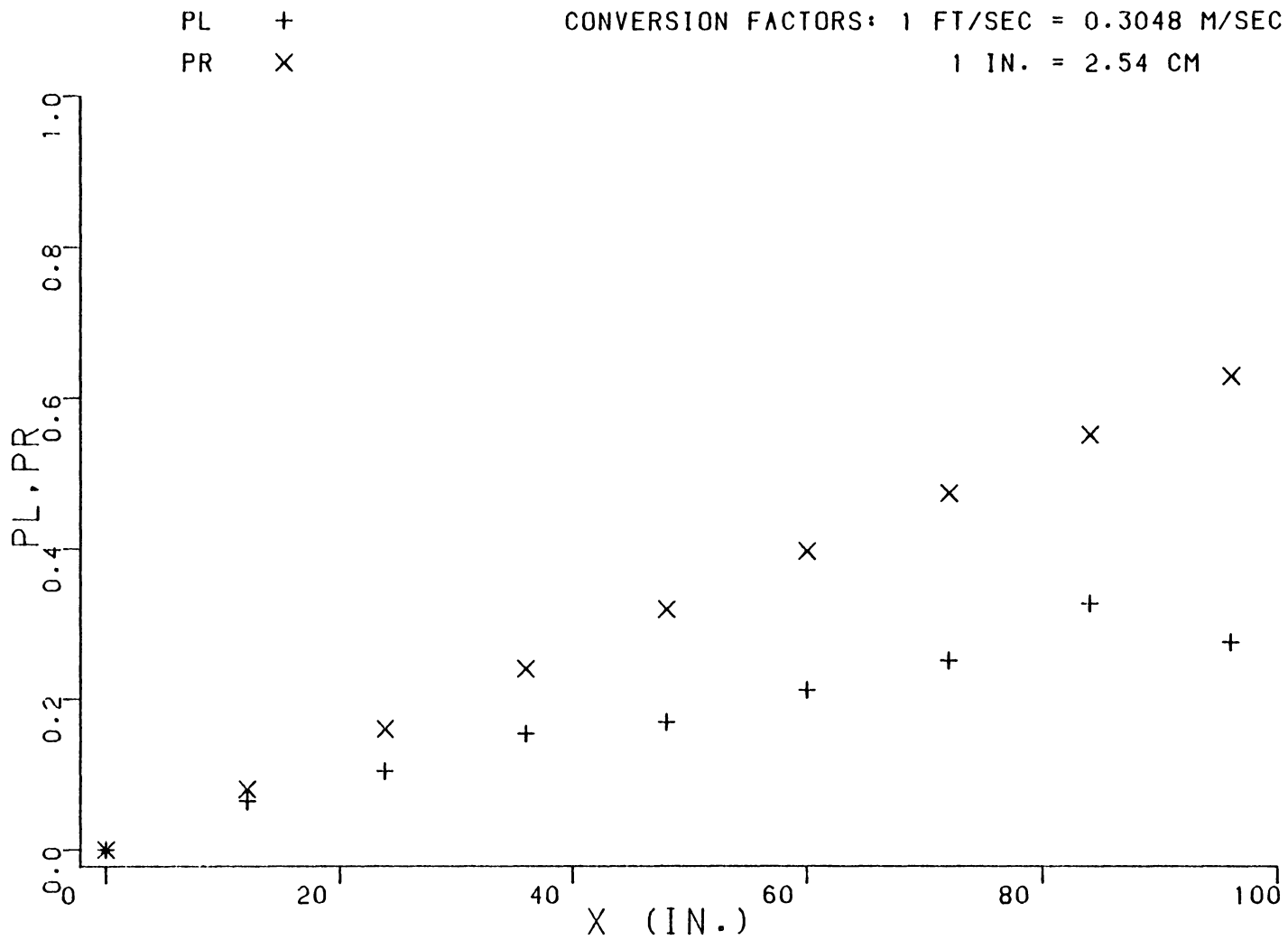


FIG. 20. MENNA SKEWED PLANE OF SYMMETRY FLOW, CASE 5

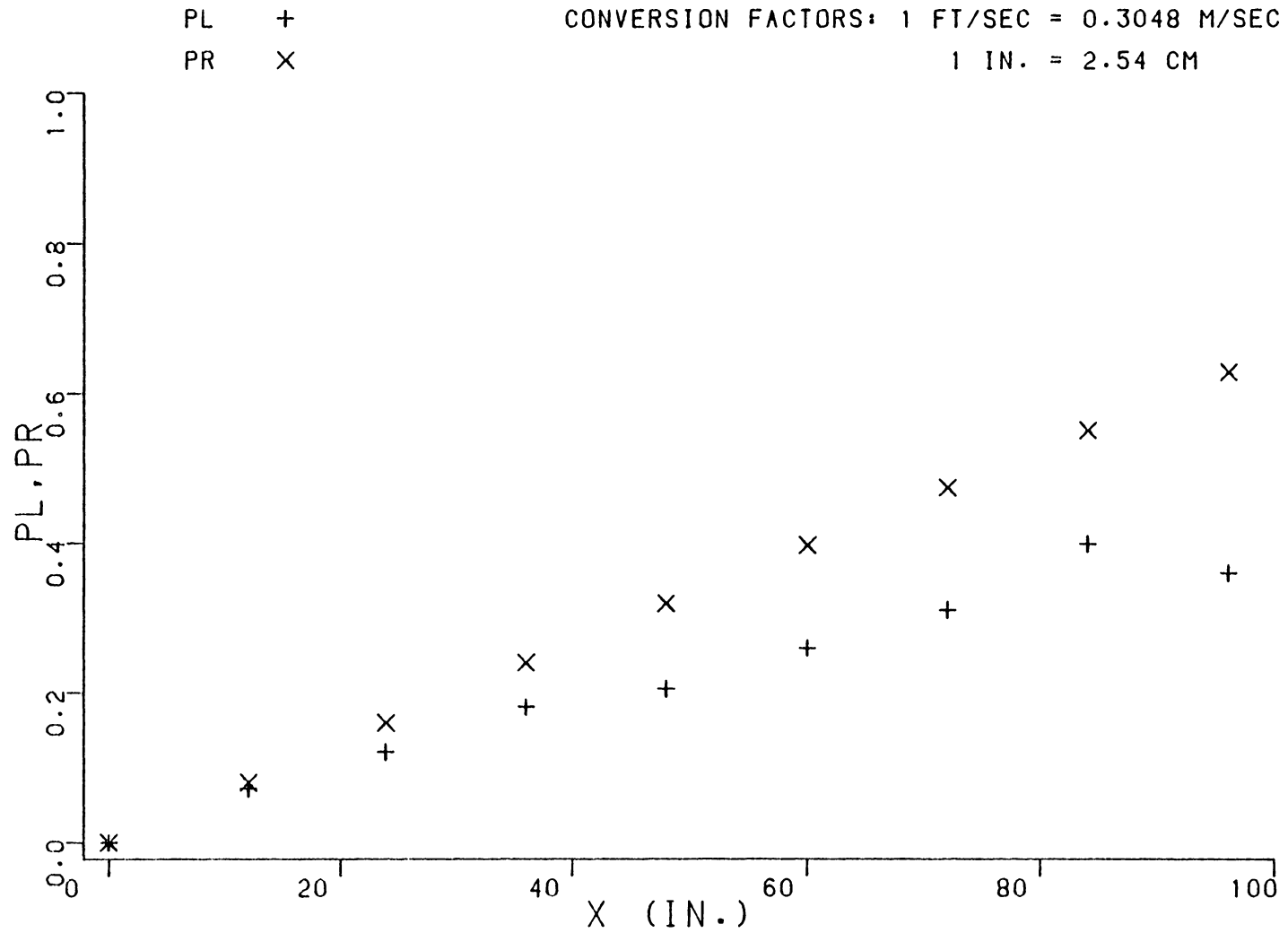


FIG. 21. MENNA SKEWED PLANE OF SYMMETRY FLOW, CASE 6

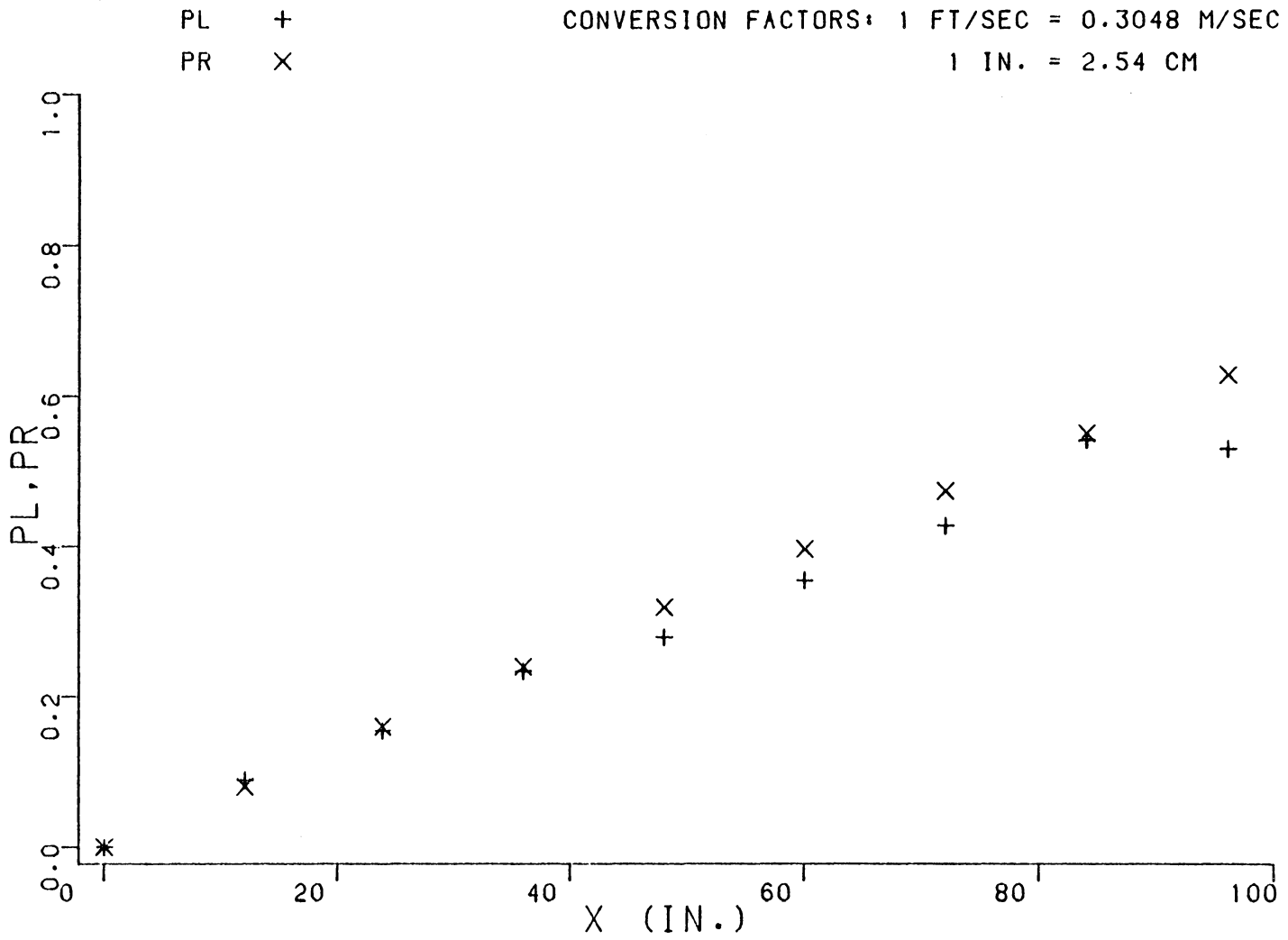


FIG. 22. MENNA SKEWED PLANE OF SYMMETRY, CASE NO. 7

Table 14. PL and PR for Menna's Assumed Skewed Plane of Symmetry Flow, Cases 1 - 7

x, in.	PL ₁	PL ₂	PL ₃	PL ₄	PL ₅	PL ₆	PL ₇	PR
0	0.0	0.0	0.0	0.0	0.0	0.0	0.0	0.0
12	0.133	0.106	0.092	0.100	0.064	0.072	0.089	0.080
24	0.248	0.190	0.162	0.178	0.104	0.121	0.155	0.160
36	0.380	0.290	0.245	0.271	0.154	0.181	0.234	0.240
48	0.482	0.356	0.294	0.331	0.169	0.205	0.279	0.319
60	0.617	0.455	0.374	0.421	0.212	0.259	0.355	0.397
72	0.755	0.553	0.453	0.512	0.251	0.310	0.428	0.474
84	0.939	0.694	0.572	0.644	0.327	0.399	0.542	0.551
96	1.00	0.710	0.565	0.650	0.275	0.360	0.530	0.629

Note: Subscripts of PL Denote Case Number.

Conversion factor

1 in. = 2.54 cm

Table 15. Freestream Spreading and Velocity Profile Skewing Contributions to PL for Cases 3 and 4

x, in.	PL _{2D}	PL ₁	PL ₂	PL ₃	PR
0	0.0	0.0	0.0	0.0	0.0
12	0.111	0.084	0.092	0.100	0.080
24	0.202	0.145	0.162	0.178	0.160
36	0.308	0.218	0.245	0.271	0.240
48	0.382	0.257	0.294	0.331	0.319
60	0.489	0.326	0.374	0.421	0.397
72	0.595	0.393	0.453	0.512	0.474
84	0.745	0.500	0.572	0.644	0.551
96	0.770	0.481	0.563	0.650	0.629

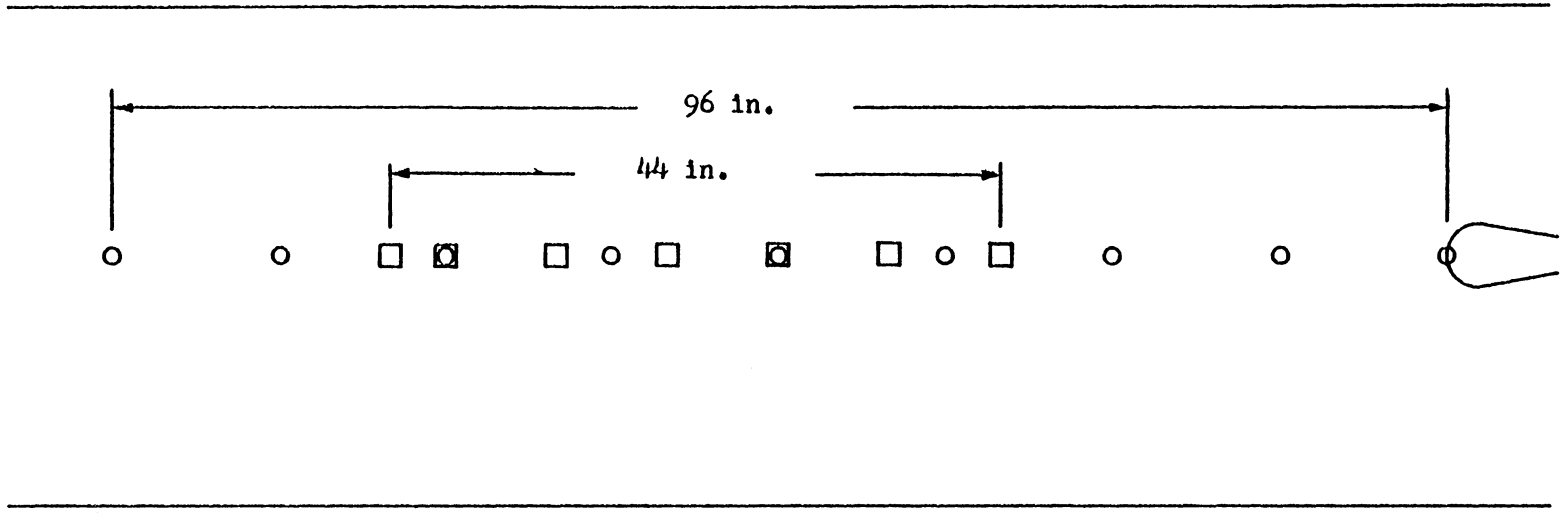
1 - Plane of symmetry, $\frac{\partial \beta}{\partial z} = -1/8 \text{ deg./in.}$

2 - Plane of symmetry, $\frac{\partial \beta}{\partial z} = -1/8 \text{ deg./in.}, \frac{\partial \alpha_0}{\partial z} = 1/15 \text{ deg./in.}$

3 - Plane of symmetry, $\frac{\partial \beta}{\partial z} = -1/8 \text{ deg./in.}, \frac{\partial \alpha_0}{\partial z} = 1/8 \text{ deg./in.}$

Conversion factor:

1 in. = 2.54 cm.



- Measurement locations for Menna (without teardrop body)
- Measurement locations for Horne (with teardrop body)

Conversion factor: 1 in. = 2.54 cm

Fig. 23 Measurement Locations for Menna and Horne

could account for the departure from two-dimensional flow were then determined.

The results of the two-dimensional examination of the data set are found in Fig. 24 and Table 16. The data set apparently described a nominally two-dimensional flow field, similar to Menna's two-dimensional data set. However, this data set was obtained in the flow field upstream of an obstruction. Menna's flow field contained no such obstruction. Equation 5.2 was utilized to determine the amounts of collateral convergence of the flow, which could account for the differences in PL and PR for the two-dimensional assumption. These collateral convergence/divergence rates are found in Table 17. One would assume that the flow field nearer the body would tend to spread from the center-plane of the tunnel. Instead, the flow appeared to fluctuate between small convergence and small divergence of the free-stream streamlines, as in the case of Menna's two-dimensional data set. This would seem to indicate that the presence of the body in the tunnel did not affect the flow field significantly upstream, where this data set was obtained.

5.3.2 Elsenaar and Boelsma, van den Berg and Elsenaar - Infinite Swept-Wing Flow

Elsenaar and Boelsma (23) made measurements of the 3DTBL on a flat surface under infinite swept-wing conditions. The investigation was performed using the same model used by van den Berg and Elsenaar (22). The hot-wire and cobra probes used in this investigation (23) were

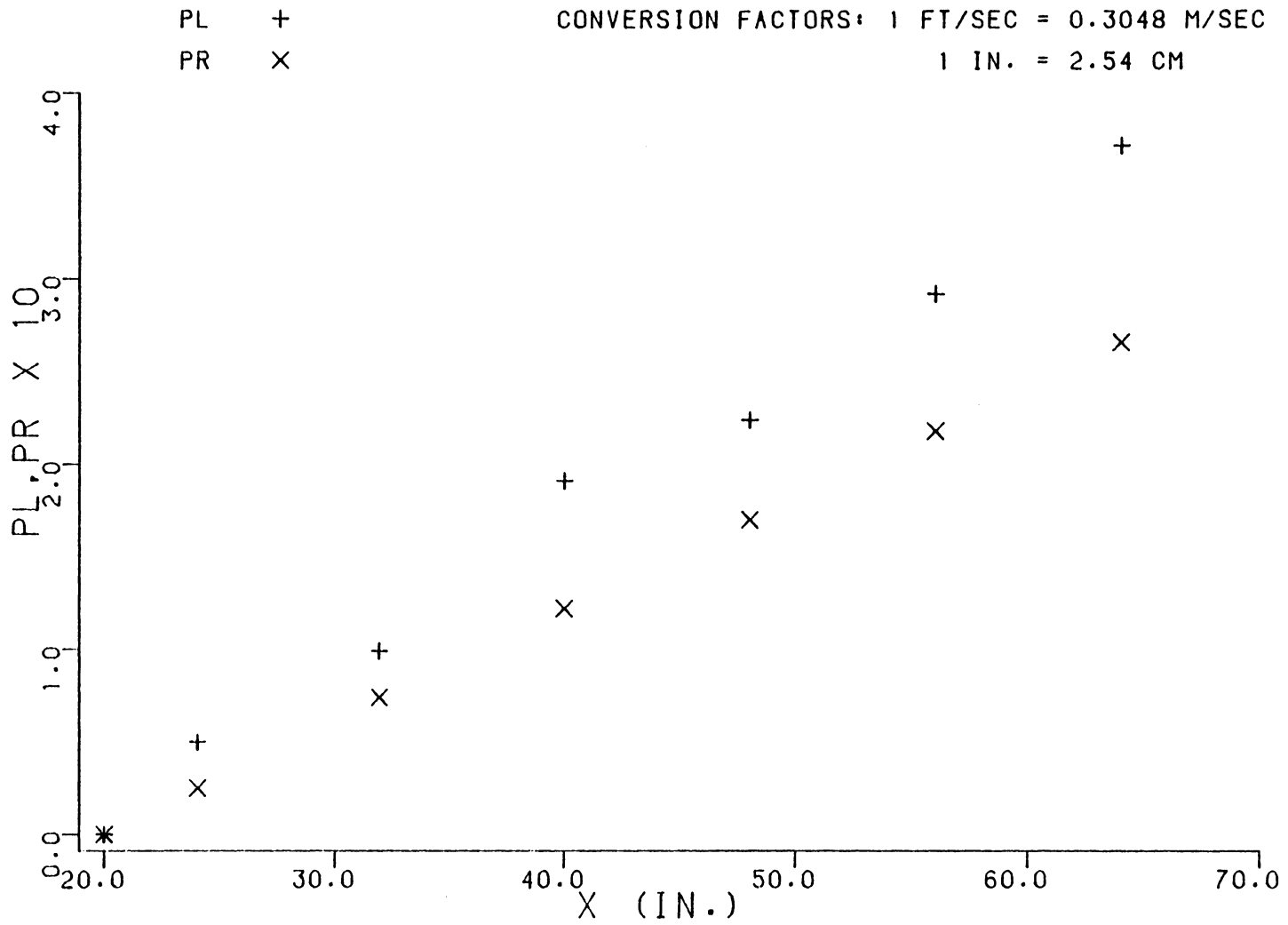


FIG. 24. HORNE. ASSUMED TWO-DIMENSIONAL FLOW

Table 16. PL and PR for Horne's Upstream Condition Flow. Assumes Two-Dimensional Flow.

x, in.	PL	PR
20	0.0	0.0
24	0.050	0.025
32	0.099	0.074
40	0.191	0.122
48	0.224	0.170
56	0.292	0.218
64	0.372	0.266

Conversion factor

1 in. = 2.54 cm

Table 17. Average Collateral Convergence/Divergence of Horne's Assumed Plane of Symmetry Flow

$x_i - x_{i+1}$, in.	$\frac{\partial \beta}{\partial z}$, $\frac{\text{deg.}}{\text{in.}}$
20 - 24	- 1/2.8
24 - 32	- 1/450
32 - 40	- 1/3.6
40 - 48	1/11
48 - 56	- 1/8.6
56 - 64	- 1/5.8

Conversion factor

1 in. = 2.54 cm

designed such that the probe tip was located 25 mm upstream of its axis of rotation. Consequently, the probe-tip described a helix with a radius of 25 mm when traversing the boundary layer. The maximum displacement of the probe tip normal to the leading edge was of the order of 5 mm at the measurement station nearest the trailing edge (see Fig. 25). Mean velocity measurements for this flow were obtained using the cobra probe. Because of the probe geometry, measurements could not be made closer than 2.5 mm to the wall in the boundary layer which ranged from 20 to 70 mm thick. The mean velocities in this region were determined by interpolation of the data of reference 22. In some cases, a slight discontinuity at the matching point was found, due to the inaccuracy of the interpolation. Also, skin friction measurements were not made. Rather, values were determined by interpolation of the skin friction data of reference 22.

The data set from Elsenaar and Boelsma (23) was examined by integrating both the chordwise and spanwise momentum integral equations in the chordwise-direction. Results of both integrations are found in Figs. 26 and 27 and Table 18. These results indicate a flow field which deviates from the infinite swept-wing assumption. In both integrations of the spanwise and chordwise momentum integral equations, values of PR appeared to follow smooth curves, while PL values tended to follow no particular trend.

In the earlier investigation of van den Berg and Elsenaar (22), the data set was examined by the authors using a different form of the momentum integral equation which indicated the data set satisfied the

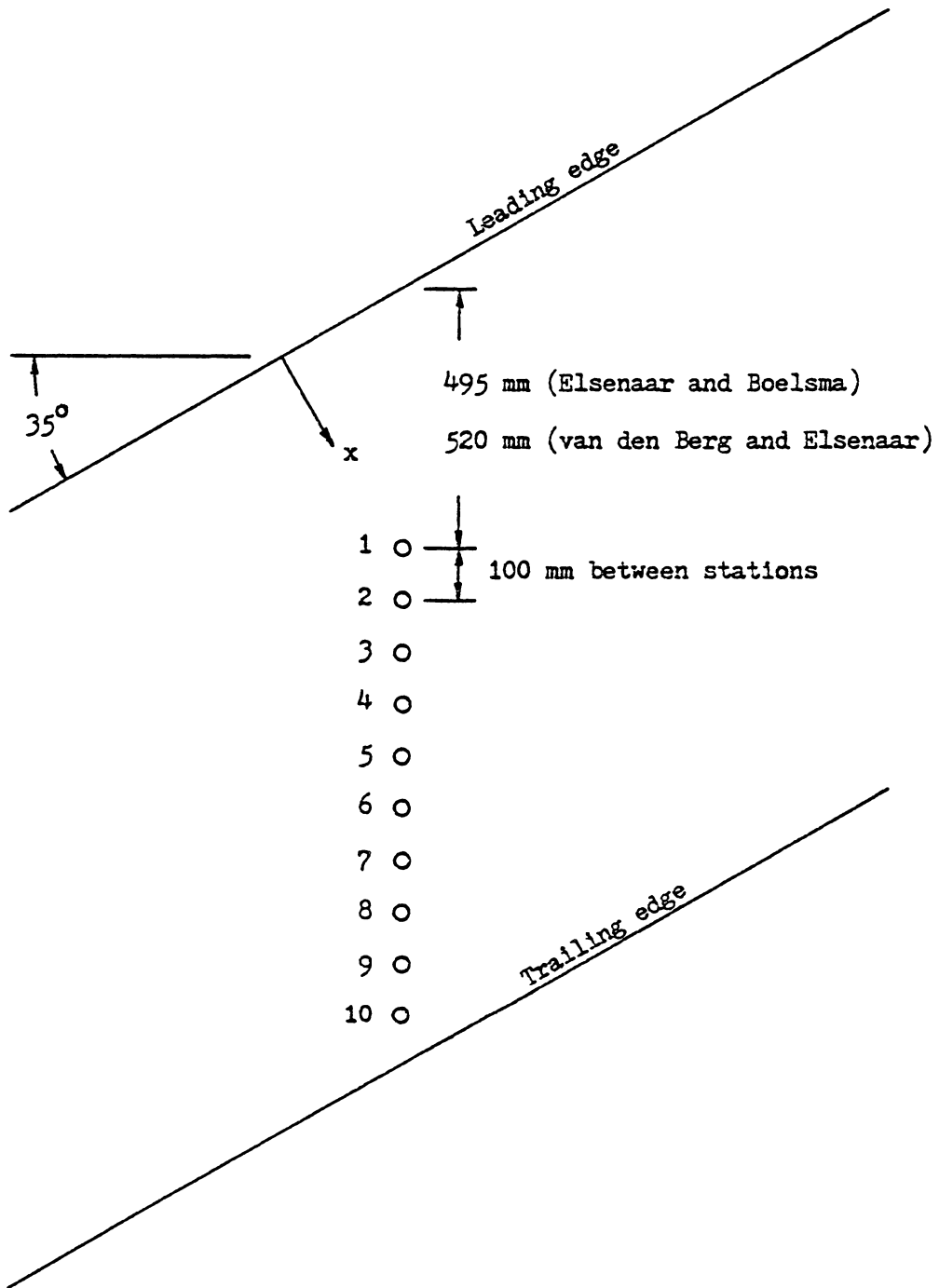


Fig. 25 Measurement Locations for Elsenaar and Boelsma, and van den Berg and Elsenaar

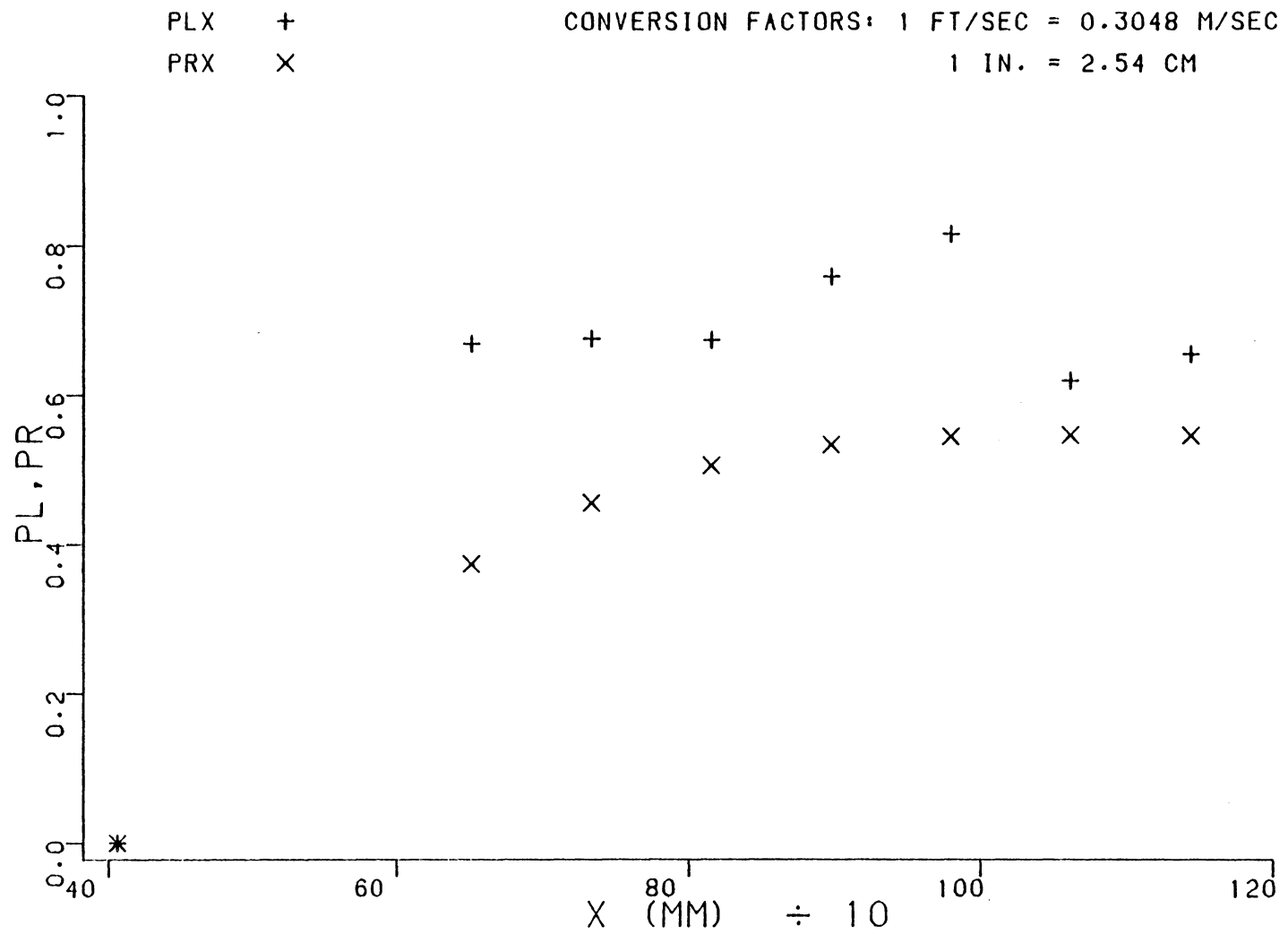


FIG. 26 ELSENAAR AND BOELSMA INFINITE SWEEP-WING, X-EQUATION

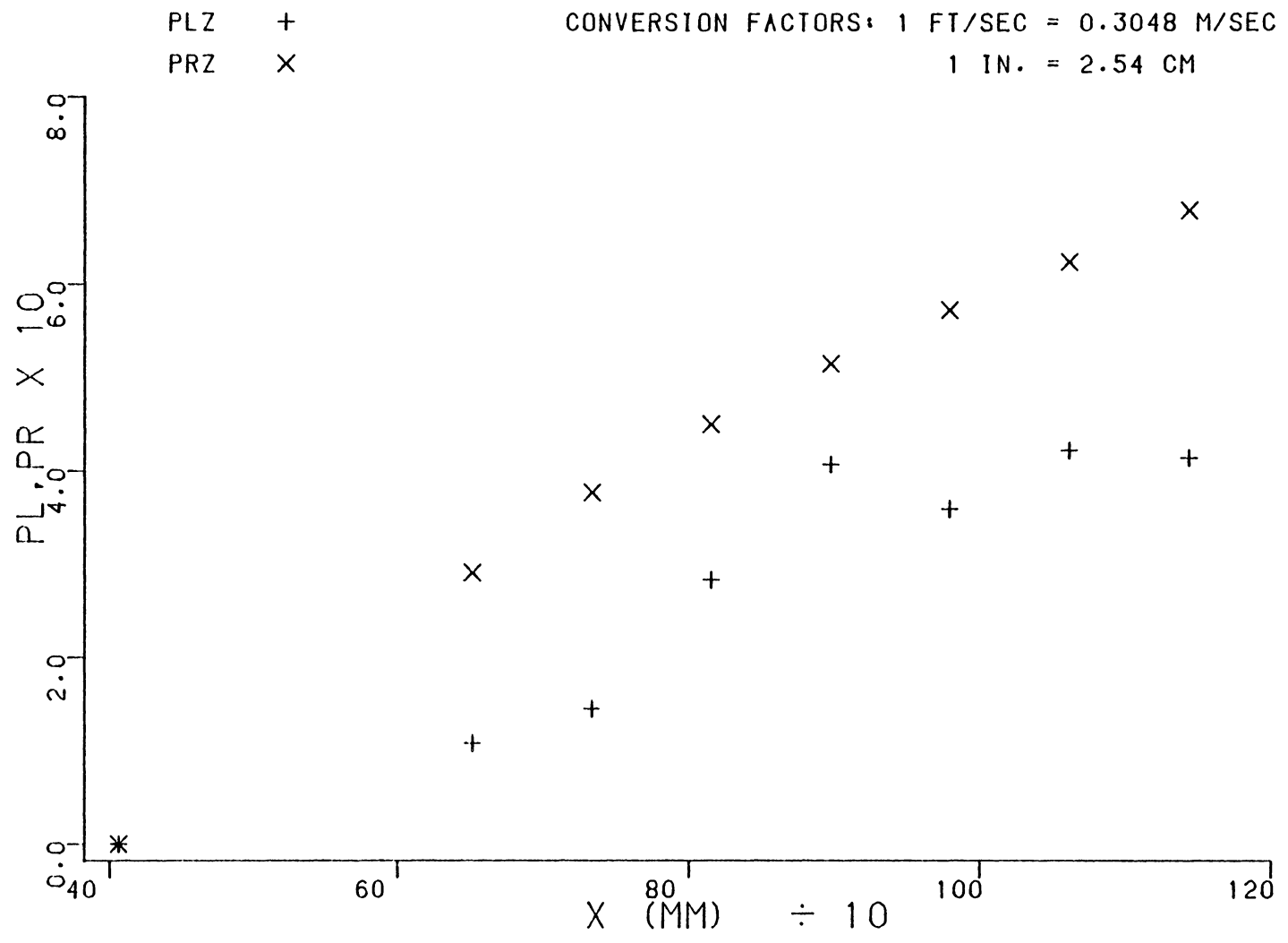


FIG. 27 ELSENAAR AND BOELSMA INFINITE SWEEP-WING, Z-EQUATION

Table 18. PL and PR for Elsenaar and Boelsma's
Infinite Swept-Wing Flow

x, mm	PL_x	PR_x	PL_z	PR_z
406	0.0	0.0	0.0	0.0
651	0.669	0.374	0.108	0.291
733	0.676	0.456	0.145	0.377
815	0.674	0.506	0.283	0.450
897	0.759	0.534	0.407	0.515
979	0.816	0.545	0.359	0.572
1061	0.620	0.547	0.422	0.624
1143	0.655	0.546	0.414	0.679

Note: Subscripts denote integration of x- or z- momentum integral equations.

infinite swept-wing assumption. No momentum integral validation of the data in reference 23 was reported by the authors. Because of the difference in momentum integral methods and for comparison purposes, van den Berg and Elsenaar's data set was also examined here. The results of the examination are found in Figs. 28 and 29 and in Table 19. This data set more nearly satisfied the infinite swept-wing assumption, although large discrepancies between PL and PR were found in the integration of the chordwise momentum integral equation at locations near the wing trailing edge. This may again be a result of the exclusion of the Reynolds normal stress terms, since three-dimensional separation occurred towards the trailing edge of the plate. These discrepancies also may have been a result of a departure from the infinite swept-wing condition.

It is not clear as to why values of PL and PR obtained from the examination of the data of reference 22 agree better than those obtained from the examination of the data of reference 23. Both experiments were performed using the same test apparatus, although data measurement techniques differed.

5.3.3 Pierce and McAllister - Flow About a Strut-Flat Plate Junction

Pierce and McAllister (15) measured the mean velocity and wall shear fields around a blunt teardrop body protruding from a flat surface. The data measurement grid utilized in the investigation is shown in Fig. 30. Since derivatives of flow parameters were required in this examination, the x- and z-momentum integral equations were

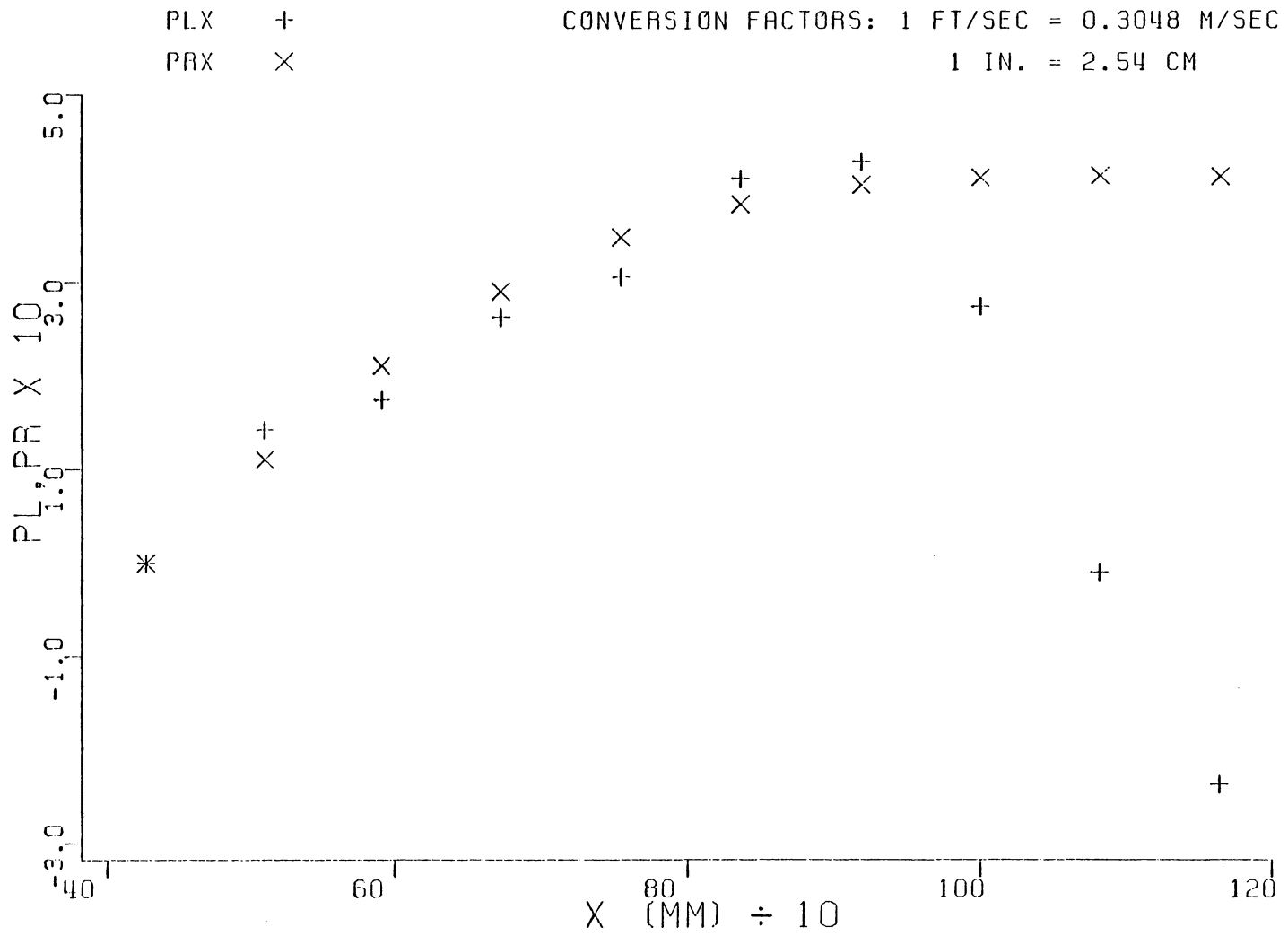


FIG. 28 VAN DEN BERG AND ELSENAAR INFINITE SWEEP-WING, X-EQUATION

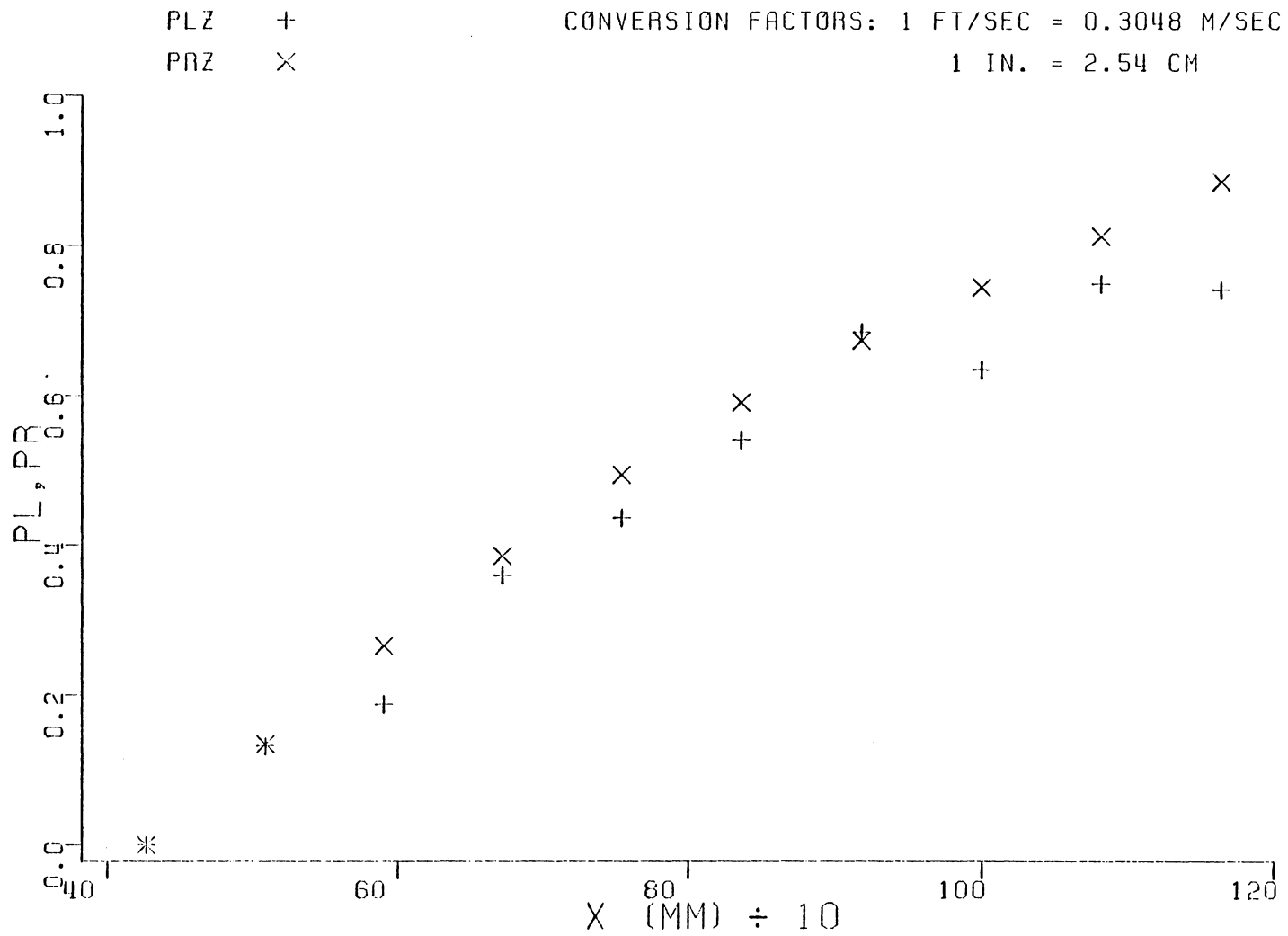


FIG. 29 VAN DEN BERG AND ELSENAAR INFINITE SWEEP-WING, Z-EQUATION

Table 19. PL and PR for van den Berg and Elsenaar's
Infinite Swept-Wing Flow

x, mm	PL _x	PR _x	PL _z	PR _z
426	0.0	0.0	0.0	0.0
508	0.143	0.111	0.132	0.135
590	0.175	0.211	0.188	0.266
672	0.263	0.290	0.360	0.386
754	0.305	0.348	0.437	0.495
836	0.411	0.384	0.541	0.591
918	0.429	0.404	4.685	0.673
999	0.274	0.412	0.634	0.745
1081	-0.010	0.414	0.749	0.812
1163	-0.237	0.413	0.741	0.886

Note: Subscripts denote integration of x- or z-
momentum integral equations.

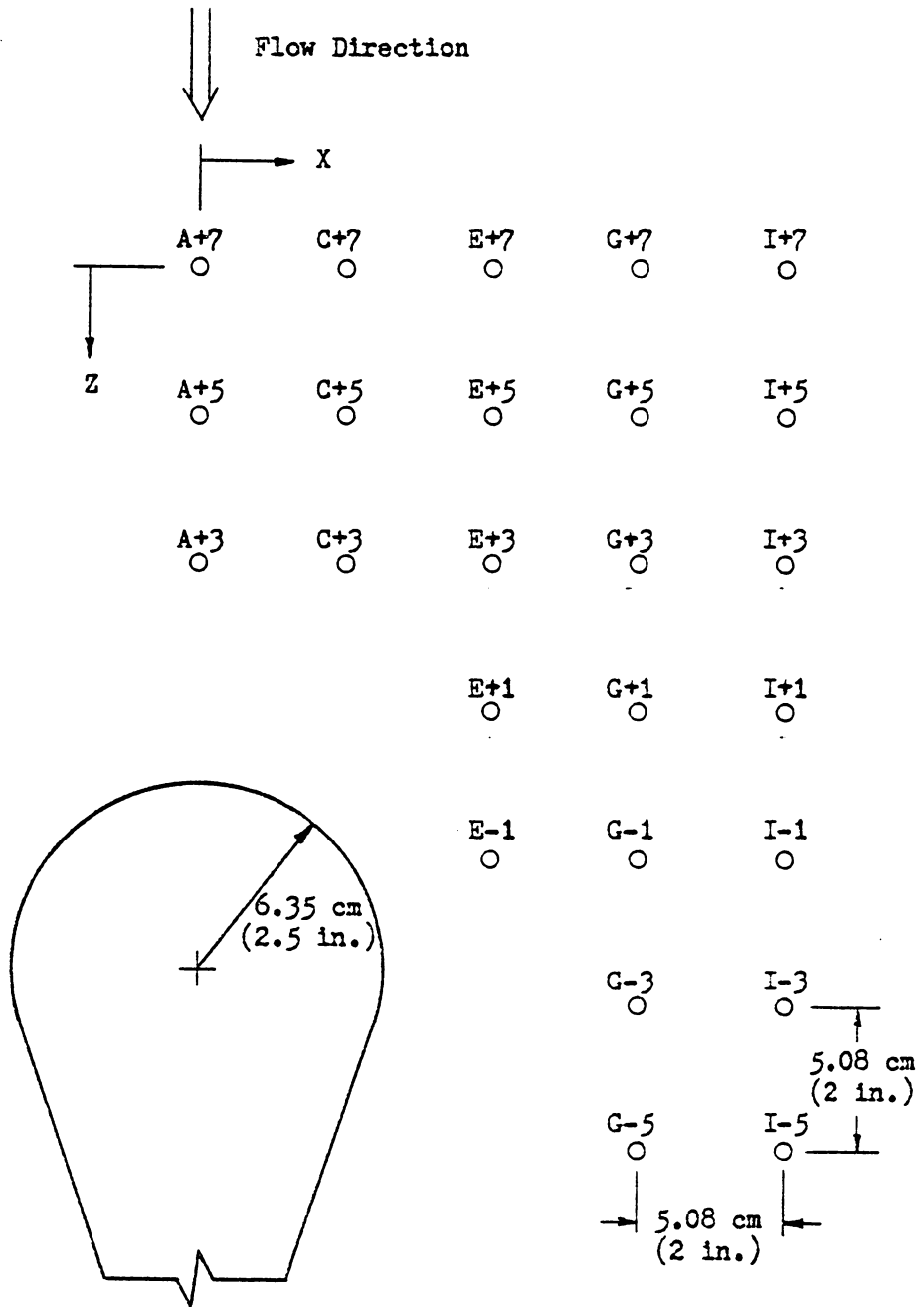


Fig. 30 Data Stations for Pierce and McAllister's Teardrop Flow

integrated in the x-direction from G+7 to G-5, and in the z-direction from A+5 to I+5 only. It should be noted that differentiation of experimental data is not a good practice, since errors due to experimental scatter are introduced. In this examination, some transverse derivatives were obtained from as few as two data points. This was unfortunate, but could not be helped since more data were unavailable.

The results of the examination are found in Figs. 31 through 34 and Tables 20 and 21. It appeared that neither data set satisfied the equations of motion for this flow field, although the G-column data set best satisfied the momentum integral equations. There are several possible explanations for the differences in PL and PR including the method of obtaining the data, neglect of Reynolds normal stress terms as separation was approached, and poor approximations of derivative terms. There is also the question of the adequacy of the boundary layer assumptions in close proximity to the separation region around the body.

All mean velocity and wall shear data were obtained by fixing the probes in the tunnel and moving the model relative to the probes. It was believed that boundary layer growth in the streamwise direction in the vicinity of the test section would be insignificant and that sidewall interference in the 0.61 m high by 0.91 m wide tunnel would be minimal as the model was moved across the test section. In a continuance of this investigation, Menna (18) has found that longitudinal movement of the model caused small differences in the velocity magnitudes and directions at points fixed relative to the model. These

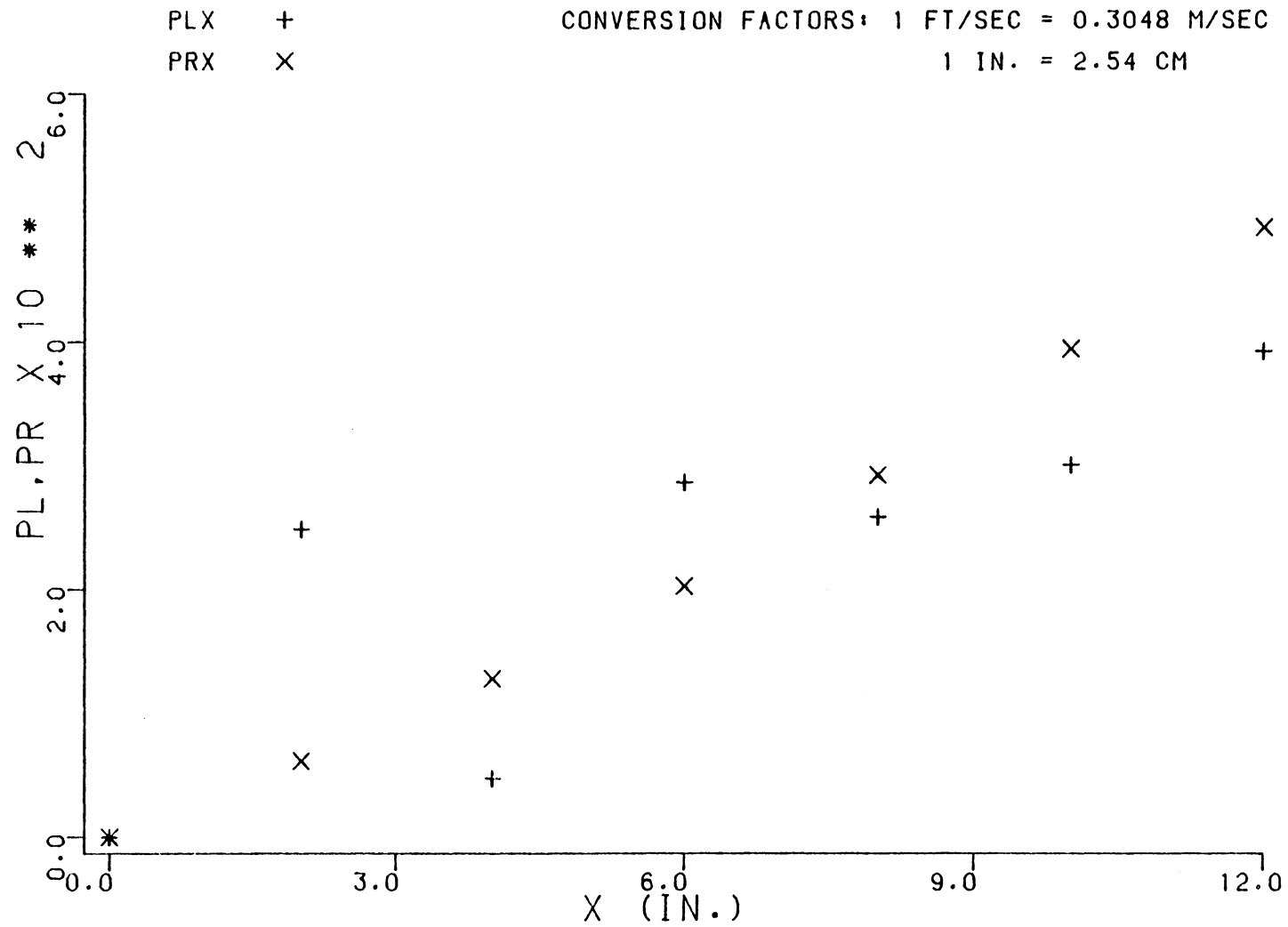


FIG.31. PIERCE AND MCALLISTER COLUMN G. X-EQUATION

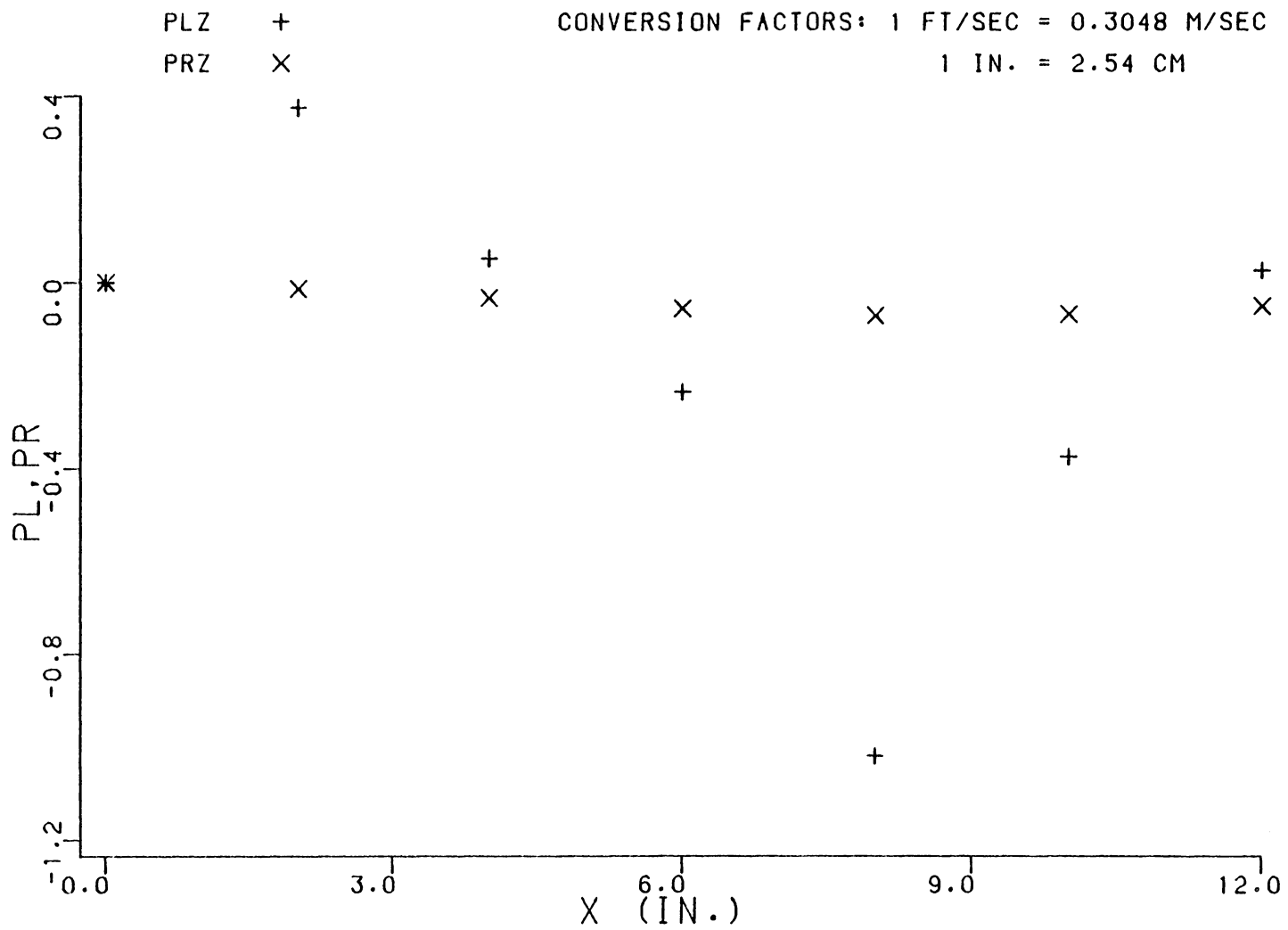


FIG. 32. PIERCE AND MCALLISTER COLUMN G. Z-EQUATION

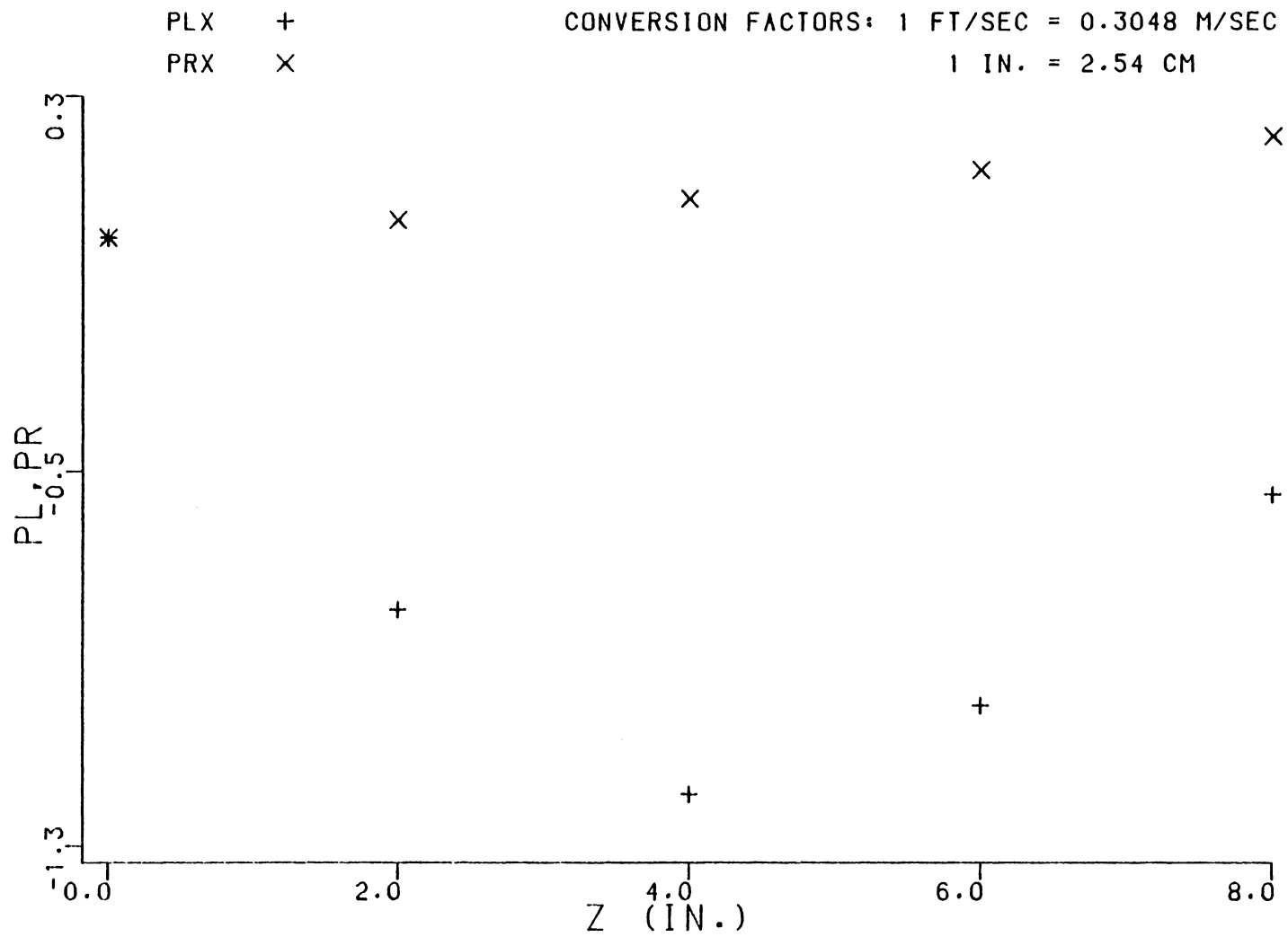


FIG. 33. PIERCE AND MCALLISTER ROW +5. X-EQUATION

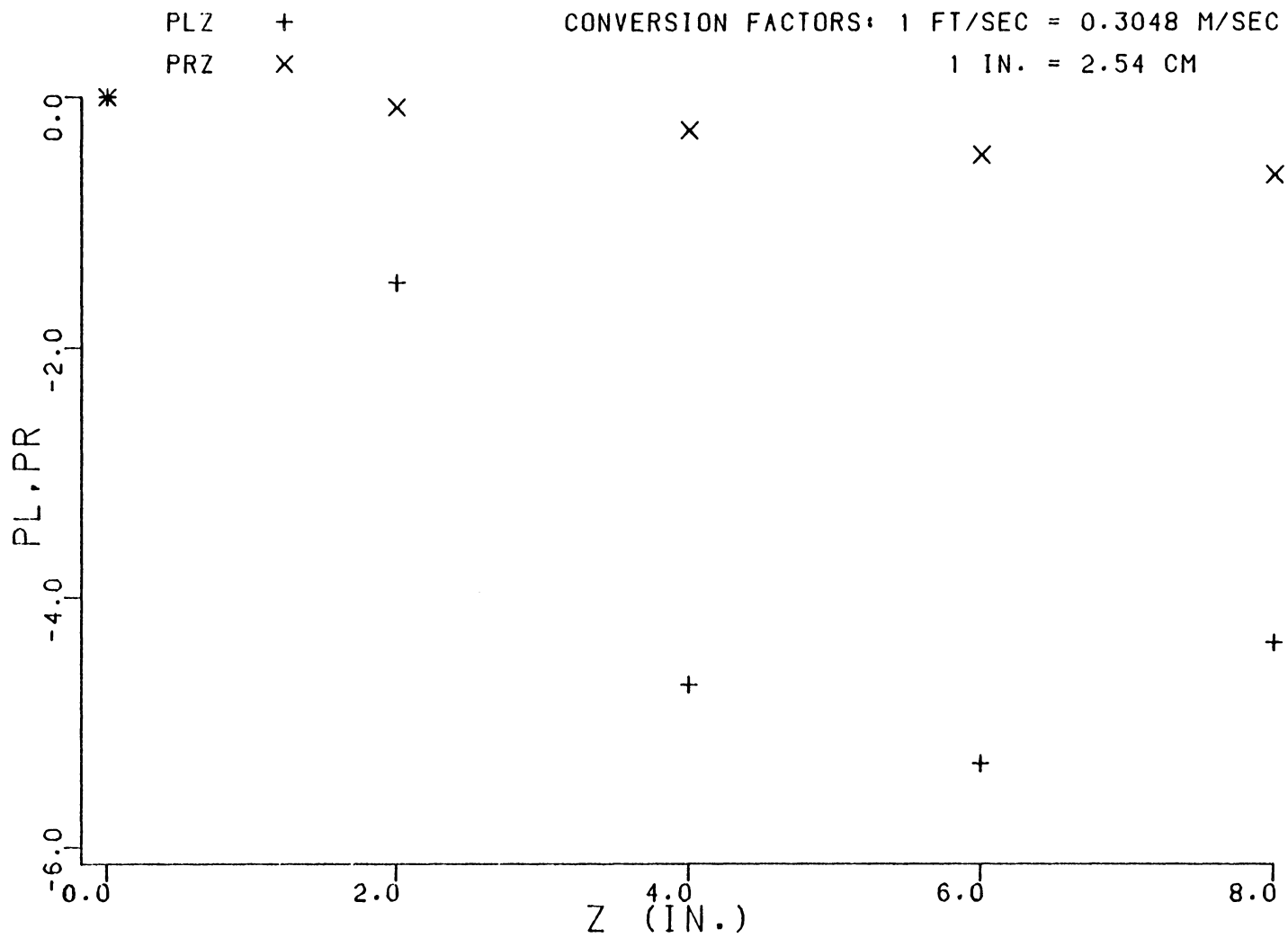


FIG. 34. PIERCE AND MCALLISTER ROW +5. Z-EQUATION

Table 20. PL and PR for Pierce and McAllister's
Strut-Flat Plate Flow on Column G

x, in.	PL _x	PR _x	PL _z	PR _z
0	0.0	0.0	0.0	0.0
2	0.0249	0.0062	0.375	-0.0137
4	0.0047	0.0128	0.052	-0.0334
6	0.0287	0.0203	-0.235	-0.0562
8	0.0259	0.0293	-1.02	-0.0715
10	0.0301	0.0395	-0.375	-0.0684
12	0.0393	0.0493	0.026	-0.0513

Note: Subscripts denote integration of x- or z-
momentum integral equations.

Conversion factor

1 in = 2.54 cm

Table 21. PL and PR for Pierce and McAllister's
Strut-Flat Plate Flow on Row +5.

z, in.	PL _x	PR _x	PL _z	PR _z
0	0.0	0.0	0.0	0.0
2	-0.795	0.0379	-1.48	-0.079
4	-1.19	0.0834	-4.70	-0.265
6	-1.00	0.144	-5.33	-0.461
8	-0.548	0.215	-4.36	-0.617

Note: Subscripts denote integration of x- or z-
momentum integral equations.

Conversion factor

1 in. = 2.54 cm

differences were consistent and essentially within the experimental uncertainty of the data and were judged to be negligible. Transverse movement of the body produced small differences in velocity magnitudes and directions which were of the order of magnitude or greater than the differences created by longitudinal body movement. These differences were consistent, but as large or larger than the experimental uncertainty and may not have been negligible. These findings were supported by the better agreement of PL and PR when the momentum integral was integrated in the x-direction than when integrated in the z-direction. The neglect of Reynolds normal stress terms, at least near the plane of symmetry close to the separated region, may also have been a contributing factor in the disagreement in PL and PR for the +5 row. There is also the question of the adequacy of the boundary layer assumptions in close proximity to the separation region. The same was not necessarily so in the G-column examination because that portion of the flow field did not approach separation.

The potential for error due to inaccurate transverse derivatives was great since, in most instances, these were obtained from curves fitted through three or less data points. Further compounding the differentiation errors, the significant gradients which existed in the flow field, especially near the body, may not have been accurately described by the 5.08 cm by 5.08 cm measurement grid. The differences in velocity direction and magnitude caused by movement of the body, as noted by Menna, would further introduce errors when differentiating the experimental data.

6. Conclusions

In this study, experimentally obtained two- and three-dimensional turbulent boundary layer data sets have been examined using momentum integral techniques. A brief review of turbulent boundary layer experiments was performed to determine which data sets could be examined using the momentum integral equations. The effect of small amounts of three-dimensionality in a nominally two-dimensional flow in the form of collateral or skewed diverging/converging flow about a plane of symmetry was also investigated.

The momentum integral equation was found to provide a convenient means of examining two-dimensional data sets. Differentiation of experimentally determined parameters in the momentum integral equation was avoided through integration of the equation. It was also found that the creation of a truly two-dimensional flow in a wind tunnel is a difficult process most probably due to inlet conditions and side-wall boundary layer growth.

Very small amounts of three-dimensionality in a nominally two-dimensional flow can have large effects on and adversely affect the outcome of a momentum integral validation of the data set. Three-dimensionality of the order of magnitude of experimental uncertainty, in the form of collateral or skewed divergence/convergence of the flow at a plane of symmetry, was shown to have large adverse effects on the momentum integral validation. For the nominally two-dimensional data sets examined in this study, a plane of symmetry flow which fluctuated between slight convergence and divergence of the

freestream streamlines at the plane of symmetry (tending more towards convergence) was shown to possibly exist. This explanation was consistent with the findings of de Brederode and Bradshaw (1).

In many three-dimensional boundary layer investigations, sufficient data were not obtained to allow for a momentum integral examination of the data sets. Except in special three-dimensional flows (rotationally symmetric and infinite swept-wing flows), derivatives of experimentally obtained parameters were required for the momentum integral equations. Unlike the two-dimensional case, where differentiation of experimental parameters was avoided by integration of the momentum integral equation, experimental parameters needed to be differentiated with respect to the direction normal to the direction of integration. For example, when integrating the momentum integral equations in the x-direction, z-derivatives were required for a solution. In order to accurately approximate these derivatives, large amounts of data must be obtained, especially in regions where gradients in the flow field are large. For the general three-dimensional data sets examined in this study, a lack of data prevented an accurate validation of the data sets using the momentum integral equations. Whether investigators will take the necessary large amounts of data required for a sound three-dimensional momentum integral validation of the data set is open to question.

References

1. de Brederode, V. and P. Bradshaw, "Influence of the Side Walls on the Turbulent Centre-Plane Boundary Layer in a Square Duct," Department of Aeronautics, Imperial College of Science and Technology, I.C. Aero Report 74-06, London, May 1974.
2. Bradshaw, P., "The Effect of Wind-Tunnel Screens on Nominally Two-Dimensional Boundary Layers," Journal of Fluid Mechanics, Vol. 22, Part 4, 1965, pp. 679-687.
3. de Bray, P. G., "Some Investigations into the Spanwise Non-Uniformity of Nominally Two-Dimensional Incompressible Boundary Layers Downstream of Gauge Screens," Aeronautical Research Council R & M No. 3578, 1969.
4. Currie, I. G., Fundamental Mechanics of Fluids, McGraw-Hill, New York, 1974.
5. White, F. M., Viscous Fluid Flow, McGraw-Hill, New York, 1974.
6. Coles, D. "The Law of the Wake in the Turbulent Boundary Layer," Journal of Fluid Mechanics, Vol. 1, 1956, pp. 191-227.
7. Coles, D. and E. Hirst, "Computation of Turbulent Boundary Layers," Proceedings Computation of Turbulent Boundary Layers - 1968, AFORSR-IFP-Stanford Conference Vol. II, 1968.
8. Patel, V. C., "Calibration of the Preston Tube and Limitations on Its Use in Pressure Gradients," Journal of Fluid Mechanics, Vol. 23, Part 1, 1965, pp. 185-208.
9. NPL Staff, "On the Measurement of Local Surface Friction on a Flat Plate by Means of Preston Tubes," Aeronautical Research Council R & M 3185, 1955.
10. Spalding, D. B., "A Single Formula for the Law of the Wall," Journal of Applied Mechanics, Trans. ASME, Vol. 83, 1961, pp. 455-458.
11. Pierce, F. J., "The Turbulent Flow at the Plane of Symmetry of a Collateral Three-Dimensional Boundary Layer," Journal of Basic Engineering, Trans. ASME, Paper No. 63-AHGT-3, 1963.
12. Johnston, J. P., "The Turbulent Boundary Layer at a Plane of Symmetry in a Three-Dimensional Flow," Journal of Basic Engineering, Trans. ASME, Series D, Vol. 82, 1960, pp. 622-628.

13. Schlichting, H., "Die Laminare Stromung um Einen Axial Angestrometen Rotierenden Drehkorper," Ingenieur - Archiv, Bd. 21, 1953, pp. 227-244.
14. Pierce, F. J. and B. B. Zimmerman, "Wall Shear Stress Inference From Two and Three-Dimensional Turbulent Boundary Layer Profiles," Journal of Fluids Engineering, Trans. ASME, Vol. 95, 1973, pp. 61-67.
15. Pierce, F. J. and J. E. McAllister, "Near-Wall Similarity in a Three-Dimensional Turbulent Boundary Layer," Report VPI-E-80.32, Department of Mechanical Engineering, Virginia Polytechnic Institute and State University, Blacksburg, Virginia, September 1980.
16. Kong, F., "Turbulent Boundary Layer over Solid and Porous Surfaces with Small Roughness," Ph.D. Dissertation, Virginia Polytechnic Institute and State University, Blacksburg, Virginia, July 1981.
17. Strickland, J. H. and R. L. Simpson, "The Separating Turbulent Boundary Layer: An Experimental Study of an Airfoil Type Flow," Thermal and Fluid Sciences Center, Southern Methodist University, T.R. WT-2, August 1973.
18. Menna, J. D. Untitled (Dissertation in Progress), Virginia Polytechnic Institute and State University, Blacksburg, Virginia, 1982.
19. Vermeulen, A., "Measurements of Three-Dimensional Turbulent Boundary Layers," Ph.D. Thesis, Cambridge University, 1971.
20. Wheeler, A. J. and J. P. Johnson, "Three-Dimensional Turbulent Boundary Layers - Data Sets for Two-Space Coordinate Flows," Report MD-32, Department of Mechanical Engineering, Stanford University, Stanford, California, August 1972.
21. Etheridge, D. W., "Three-Dimensional Turbulent Boundary Layers on 45° Swept Plate and Drag Calculation for a Series of Bodies of Revolution," Ph.D. Dissertation, University of London, 1972.
22. van den Berg, B. and A. Elsenaar, "Measurements in a Three-Dimensional Incompressible Turbulent Boundary Layer in an Adverse Pressure Gradient Under Infinite Swept Wing Conditions," National Aerospace Laboratory NLR, NLR TR 72092 U (Draft Version), 1972.

23. Elsenaar, A. and S. H. Boelsma, "Measurements of the Reynolds Stress Tensor in a Three-Dimensional Boundary Layer Under Infinite Swept Wing Conditions," National Aerospace Laboratory NLR, NLR TR 74095 U, 1974.
24. Zimmerman, D. R. and D. E. Abbott, "An Experimental Investigation of a Three-Dimensional Turbulent Boundary Layer," ASME Paper 77-WA/FE-22, 1977.
25. Bertelrud, A., "Measurements on a Three-Dimensional Swept Wing at Low Speeds, Part I, The Flow Around the Leading Edge," Aeronautical Research Institute of Sweden, Report 130, 1977.
26. Bertelrud, A., "Measurements on a Three-Dimensional Swept Wing at Low Speeds, Part II, The Flow in the Boundary Layer on the Main Wing," Aeronautical Research Institute of Sweden, Report 131, 1977.
27. East, L. F. and R. P. Hoxey, "Low-Speed Three-Dimensional Turbulent Boundary Layer Data," Parts 1 and 2, Aeronautical Research Council R & M 1653, March 1969.
28. Luzhanskii, B. E. and V. P. Solntsev, "Experimental Flow Analysis of Three-Dimensional Separation Zones in Front of Weirs," Journal of Applied Mechanics and Technical Physics, Vol. 13, No. 1, 1972, pp. 41-44.
29. Ezekwe, C. I., "Turbulent Stress Tensors in a Three-Dimensional Boundary Layer," Ph.D. Dissertation, Virginia Polytechnic Institute and State University, Blacksburg, Virginia, December 1974.
30. Dechow, R. and K. O. Felsch, "Measurements of the Mean Velocity and of the Reynolds Stress Tensor in a Three-Dimensional Turbulent Boundary Layer Induced by a Cylinder Standing on a Flat Wall," Symposium on Turbulent Shear Flows, April 18-20, 1977, University Park, Pennsylvania, Vol. 1.
31. Tennant, M. H. "Near-Wall Similarity in Three-Dimensional Turbulent Boundary Layers," Ph.D. Dissertation, Virginia Polytechnic Institute and State University, Blacksburg, Virginia, November 1977.
32. Gruschwitz, E., "Turbulente Reibungsschichten mit Sekundarströmung," Ingenieur Archiv, Bd. VI, 1935, pp. 355-365.
33. Francis, G. P. and F. J. Pierce, "An Experimental Study of Skewed Turbulent Boundary Layers in Low Speed Flows," Journal of Basic Engineering, Trans. ASME, vol. 89, 1967, pp. 597-608.

34. Klinksiek, W. F., "An Incompressible Three-Dimensional Turbulent Boundary Layer on the Floor of a Recurving Rectangular Channel," M.S. Thesis, Virginia Polytechnic Institute and State University, Blacksburg, Virginia, September 1967.
35. Duerson, S. H., Jr., "Measurements of the Reynolds Stress Tensor in a Three-Dimensional Turbulent Boundary Layer," M.S. Thesis, Virginia Polytechnic Institute and State University, 1972.
36. Gregory, N., Stuart, J. T., and W. S. Walker, "On the Stability of Three-Dimensional Boundary Layers with Application to the Flow Due to a Rotating Disk," Philosophical Transactions of the Royal Society of London Series A. Mathematical and Physical Sciences, Vol. 248, No. 943, July 14, 1955, pp. 155-199.
37. Cham, T-S. and M. R. Head, "Turbulent Boundary-Layer Flow on a Rotating Disk," Journal of Fluid Mechanics, Vol. 37, Part 1, 1969, pp. 129-147.
38. Parr, O., "Untersuchungen der Dreidimensionalen Grenzschicht an Rotierenden Drehkörpern bei Axialer Anströmung," Ingenieur - Archiv, Bd. 32, 1963, pp. 393-413.
39. Bissonette, L. R. and G. L. Mellor, "Experiments on the Behavior of an Axisymmetric Turbulent Boundary Layer with a Sudden Circumferential Strain," Princeton University, AMS Report No. 1016, October 1971.
40. Lohmann, R. P., "The Response of a Developed Turbulent Boundary Layer to Local Transverse Surface Motion," Ph.D. Dissertation, The University of Connecticut, 1973.
41. Furuya, Y. and I. Nakamura, "Velocity Profiles in the Skewed Boundary Layers on Some Rotating Bodies in Axial Flow," Journal of Applied Mechanics, Trans. ASME, Series E, March 1970, pp. 17-24.
42. Nelson, D. J., "Pressure and Velocity Fields in a Relaxing Three-Dimensional Turbulent Boundary Layer," M.S. Thesis, Virginia Polytechnic Institute and State University, Blacksburg, Virginia, August 1979.
43. Higuchi, H. and M. W. Rubesin, "An Experimental and Computational Investigation of the Transport of Reynolds Stress in an Axisymmetric Swirling Boundary Layer," AIAA 19th Aerospace Sciences Meeting, January 12-15, 1981, St. Louis, Missouri, AIAA-81-0416.

44. Hebbar, K. S. and W. L. Melnik, "Measurements in the Near-Wall Region of a Relaxing Three-Dimensional Low Speed Turbulent Air Boundary Layer," Department of Aerospace Engineering, University of Maryland, TR No. AE-76-1, July 1976.
45. Winklemann, A. E. and W. L. Melnik, "An Experimental Investigation of a Two and a Three-Dimensional Low Speed Turbulent Boundary Layer," Department of Aerospace Engineering, University of Maryland, TR No. AE-76-2, December 1976.
46. East, L. F. and W. G. Sawyer, "Measurements of the Turbulence Ahead of a 45° Swept Step Using a Double Split-Film Probe," RAE TR 79136, November 1979.
47. Catalano, G. D., Morton, J. B., and J. B. Humphris, "Pressure and Velocity Measurements in a Three-Dimensional Wall Jet," AIAA Journal, Vol. 17, No. 4, 1979, pp. 332-333.
48. Horne, M. P., "Measurement of the Upstream and Edge Boundary Conditions for a Three-Dimensional Incompressible Turbulent Boundary Layer Flow," M.S. Thesis, Virginia Polytechnic Institute and State University, Blacksburg, Virginia, October, 1979.
49. Pierce, F. J., "The Law of the Wake and Plane of Symmetry Flows in Three-Dimensional Turbulent Boundary Layers," Journal of Basic Engineering, Trans. ASME, 1965, pp. 1-8.
50. Apostol, T. M., Mathematical Analysis - A Modern Approach to Advanced Calculus, Addison-Wesley, Massachusetts, 1957.
51. Mager, A., "Generalization of Boundary-Layer Momentum Integral Equations to Three-Dimensional Flows Including Those of Rotating System," NACA Report 1067, 1952.

**The vita has been removed from
the scanned document**

A Study of Two- and Three-Dimensional
Turbulent Boundary Layer Data Sets Using
Momentum Integral Techniques

by

David O. Fitts

(ABSTRACT)

An examination of selected two- and three-dimensional turbulent boundary layer data sets was made to determine the consistency of these data sets with their appropriate momentum integral equations. Several turbulent boundary layer experiments were reviewed to determine which of these provided adequate data so that they could be examined using this method. The selected data sets were used to numerically integrate and compare the two sides of the appropriate momentum integral equations in an extension of the Coles' momentum integral (PL-PR) method originally derived for two-dimensional flow.

The effects of small three-dimensionality in a nominally two-dimensional flow were also studied. Three-dimensionality due to converging or diverging collateral flow and converging or diverging skewed flow about a plane of symmetry was investigated.

The momentum integral examination of two-dimensional and quasi-two-dimensional data sets was verified to be a useful and convenient means of data set validation. Very small amounts of three dimensionality in a nominally two-dimensional flow could have large effects on and adversely affect the outcome of a momentum integral validation of the data set. Three-dimensionality of the order of magnitude of

experimental uncertainty, in the form of collateral or skewed convergence/divergence of the flow at a plane of symmetry, was shown to have large adverse effects on the momentum integral validation. Investigations of arbitrary three-dimensional flows were generally found to lack sufficient data to perform an accurate validation using this PL-PR technique extended to such flows.